Deceleration and trapping of polyatomic molecules

by

Manish Vashishta

B. Tech., Indian Institute of Technology, Guwahati,2012

A THESIS SUBMITTED IN PARTIAL FULFULLMENT

OF THE REQUIREMENTS FOR THE DEGREE OF

Doctor of Philosophy

In

THE FACULTY OF GRADUATE AND POSTDOCTORAL STUDIES

(Chemistry)

The University of British Columbia

(Vancouver)

April 2020

Abstract

In this dissertation, substantial headway towards the Zeeman deceleration and magnetic trapping of methyl radicals, and the standing-wave Stark deceleration and AC Stark trapping of ammonia are presented. Notably, the first ever trapping of gaseous methyl radicals within a permanent magnetic trap is discussed in detail. Additionally, the use of a counter rotating nozzle to produce slow polyatomic molecule beams is discussed.

The methyl radical is the smallest stable paramagnetic intermediate hydrocarbon species, and as such, is the physicochemical properties of this species are of substantial interest to astrochemists and organic chemists alike. Methyl radical, being a paramagnetic molecule, is decelerated using an 85 coil Zeeman decelerator from 320 m/s to 60 m/s. Notably, the first ever trapping of methyl radicals in the gas phase inside a permanent magnetic trap is described here. The trapped radicals had a temperature of 200 mK, and a lifetime greater than one second. Lastly, the elastic collisional cross sections for the methyl radical with helium and argon are also reported.

In addition to the magnetic trapping of the methyl radical, progress towards the trapping of polar molecules with microwave radiation is discussed in detail. A quality (abbr. Q) factor of 5×10^5 was achieved by cooling a Fabry Perot cavity with superconducting mirror surfaces to 3 K. Resulting from the large Q factor, the maximum electric field inside the cavity is 1 MV/m when a power input of 10 W is used. The cavity is cooled to 3 K in order to achieve a quality factor of 5×10^5. Due to the high Q factor and a power input of 10 Watts, the maximum electric field inside the cavity is 1 MV/m. At this electric field, NH_3 molecules travelling slower than 10 m/s can be successfully trapped. Additionally, the AC stark shift of NH_3 molecules within the trap is reported as the first step towards their trapping.

In addition to the two Stark and Zeeman decelerators, a counter rotating nozzle was constructed based on the design presented by Gupta et al. at Harvard University. The technical modifications presented in this thesis yielded an increase in the density of the molecular beam by three orders of magnitude, compared to the original design. This nozzle was used to decelerate acetone from 430 m/s to 110 m/s, and unlike the Stark and Zeeman decelerators, it can be used to decelerate any gaseous molecules.

Lay Summary

The accuracy of a measurement involving light and matter increases with their interaction time. The interaction time can be increased by slowing the particles and storing them inside a trap. In this dissertation, a counter rotating nozzle and a Zeeman decelerator are the two methods used to slow down polyatomic molecules. Using the Zeeman decelerator, it was possible to store the methyl radicals in a permanent magnetic trap. In addition to employing the current existing methods, a new type of trap which uses MWs has been developed. These works are aimed towards developing schemes for slowing and trapping of particles, particularly polyatomic molecules. Atoms and some diatomic molecules can be slowed and trapped using laser cooling technique, which is not applicable in general, for polyatomic molecules.

Another phenomenon which manifests itself when the atoms or molecules moves slowly, is their increase in thermal De Broglie wavelength. This gives rise to quantum effects during collision between atoms or molecules. The particles can influence each other at a distance which can be larger than its size due to its increased thermal De Broglie wavelength at slow speeds. This effect is investigated with the trapped radicals and their collisions with helium and argon atoms.

Preface

This dissertation is based on the experiments conducted on a Zeeman decelerator and a Counter rotating nozzle which were already constructed in the lab of Dr. Takamasa Momose at UBC before I joined as a graduate student in 2014. A new Fabry Perot cavity was constructed in 2017, in collaboration with Dr. Frank Steinkemeir at The University of Freiburg, Germany, to trap polar molecules using MW radiation.

Chapter 3 and 4 covers the production, deceleration and trapping of methyl radical using the Zeeman decelerator. The density of trapped radicals is also estimated as the future experiments such as sympathetic cooling or collision experiments, depend on the density of trapped radicals. In addition to this, the collision dynamics of trapped radicals with noble gas atoms is also discussed. The Zeeman decelerator was constructed in 2013, by the machine shop, electronics shop at UBC, and members of Momose lab namely Pavle Djuricanin, Yang Liu, Sida Zhou and Wei Zhong. Following 2014, the mechanical maintenance for the Zeeman decelerator involving the coils, feedthroughs, nozzle and other experimental components was done by me. The electronic shop at UBC chemistry department provided the support for electronic components. The experimental work done to trap methyl radicals was done my and Dr. Yang Liu, who was working as a post-doctorate fellow in Momose lab. All the data analysis presented in chapter 4 were also done by me. The LabVIEW program for data acquisition was developed by Tony Mittertreiner, from the electronics shop at UBC, chemistry department. The theoretical calculations for elastic cross section as well as the deceleration timing sequence were performed by Dr Yang Liu. The work done towards optimization of methyl radical generation in chapter 3 has resulted in the following publication: “Jonas Grzesiak, Manish Vashishta, Pavle Djuricanin, Frank Stienkemeier, Marcel Mudrich, Katrin Dulitz, and Takamasa Momose, Review of Scientific

Instruments 89, 113103". The work done in chapter 4 has resulted in the following paper: "Yang Liu, Manish Vashishta, Pavle Djuricanin, Sida Zhou, Wei Zhong, Tony Mittertreiner, David Carty, and Takamasa Momose, Phys. Rev. Lett. 118, 093201"

Chapter 5 covers the progress towards trapping of ammonia molecules using MW radiation. A Fabry Perot cavity was constructed for this goal whose inner mirror surfaces are coated with a superconducting material. The Fabry Perot cavity was designed in by Dr. Katsunari Enomoto, Pavle Djuricanin, Dr. Takamasa Momose and me while it was machined at the University of Freiburg, Germany. The coating of superconducting material on the cavity mirrors were done my Pavle Djuricanin and myself at UBC. The LabVIEW program for data acquisition was developed by Tony Mittertreiner, from the electronics shop at UBC, chemistry department. All the data acquisition and analysis in chapter 5 were performed by me.

In chapter 6, the slowing of acetone molecules using a counter rotating nozzle is discussed. Like the estimation of density of trapped radicals in chapter 4, chapter 6 also presents the estimated density of Argon beam using an RGA detector. The experiment was designed by Pavle Djuricanin while the LabVIEW program for data acquisition was developed by Ilja Gerhardt. All the data acquisition and analysis in this chapter has been performed by myself.

Table of Contents,

List of tables

List of figures

Glossary

REMPI Resonance enhanced multi photon ionization

MPI Multi photon ionization

MCP Micro channel plate

HFS High field seeking

LFS Low field seeking

MW Microwave

RGA Residual gas analyzer

AMU Atomic mass unit

Acknowledgments

I’m immensely grateful for the leadership, support, and guidance I’ve received from professors, coworkers, family and friends that led to the success of this project. To my supervisor, Dr. Takamasa Momose, thank you for taking me on as a student and patiently providing support and guidance.

Thank you also to Dr. Yang Li and Dr. Katsunari Enomoto for making a collaborative team, for lending support, ideas and instruction. Thanks to Pavle Djuricanin for your technical support with each thing that just wouldn’t work. Thanks to the many past and present lab mates who shared experience and banter, including Dr. Eric Miller, Brendan Moore, Jiahong Hu, Colton Carlson, Thomas Prescott, Cindy Toh, Angel Wong, Wei Zhong, Omid Nourbakhsh, Sida Zhou, Harman Brar, Satveer Singh, and Tim Schemberly. Thanks to my family and friends, for love and support. Thanks to my parents for a lifetime of support

Chapter 1.

The field of cold atoms and molecules has made it possible to achieve temperature on the order nano-Kelvin which is almost close to zero Kelvin. This achievement has made it possible to enhance our knowledge about matter which has far reaching consequences. For example, the upper limit set on the magnitude of the electric dipole moment (EDM) of an electron is less than 1.1 $x10^{-29}$ e cm [1], which was measured inside a thorium monoxide (ThO) molecule. This measurement serves as a test for the Standard Model of particle physics which predicts it to be $<10^{-38}$ e cm [2,3,4]. Other models beyond the Standard Model predicts this value between $10^{-27} – 10^{-30}$ e cm which can be now compared with experiments. So far, a standard molecular beam of ThO has been used to measure the electron's EDM but efforts are being made to cool the ThO molecule in order to increase the precision of the measurement. Another example is the measurement of variation of fundamental constants with time such as the fine structure constant or electron-to-proton mass ratio which are believed to be constant with time in the Standard Model of particle physics. These precision measurements are allowing us not only to test but go beyond the Standard Model of particle physics which is unable to explain matter-antimatter asymmetry, strong CP problem or dark matter and energy problems. These applications emphasize the importance of cold molecules in the field of physics. However, another side of cold molecules essence emerges from a chemist's point of view. As the temperature of a gas decreases, it's thermal De Broglie wavelength, λ_{th} increases which is given by [5]

$$\lambda_{th} = \frac{h}{(2\pi mkT)^{\frac{1}{2}}} \tag{1.1}$$

When λ_{th} becomes comparable to the interparticle distance or to the size of particles, the particles start to abide by the rules of quantum statistics rather than classical statistics. Collisions between

two particles at such condition can no longer be treated as hard sphere collisions and quantum effects such as interference, scattering resonance, or tunneling phenomenon may be observed during collisions [6].

Table 1-1 shows λ_{th} of a methane (CH_4) molecule at different temperature. The classical size for CH_4 is approximately 4 Å [7]. At around 1 K, methane molecules are expected to show quantum effects as their classical size becomes comparable to their thermal De Broglie wavelength.

Table 1-1:Velocity and the thermal De Broglie wavelength of a methane molecule at different temperature

T	CH4(v)	CH4(λ_{th})
300 K	400 m/s	0.2 Å
1 K	23 m/s	4.3 Å
10 mK	23 cm/s	4.3 nm
10 nK	2.3 mm/s	4370 nm

1.1 Temperature

Any gas molecule can store energy in the forms of both kinetic energy due to the motion of its constituent atoms and potential energy due to the interatomic forces. The motion of molecule in space reflects the translational degrees of freedom whereas the internal degrees of freedom consist of rotation and vibration of a molecule around its center of mass. The total energy, E due to all degrees of freedom of a molecule, with mass m, at a temperature T, can be given as

$$E = E_T + E_v + E_R$$

where E_T is the translational energy, E_v is the vibrational energy and E_R is the rotational energy of the molecule. According to the equipartition theorem, the energy of a system in thermal equilibrium is distributed equally among its various degrees of freedom. A diatomic molecule has 6 degrees of freedom which includes 3 translational, 2 rotational and 2 vibrational modes of motion (one due to kinetic energy and the other due to potential energy during vibration). Therefore, the molar heat capacity at a constant volume for a diatomic molecule at very high temperature is given by $C_v = \frac{7}{2}R$.

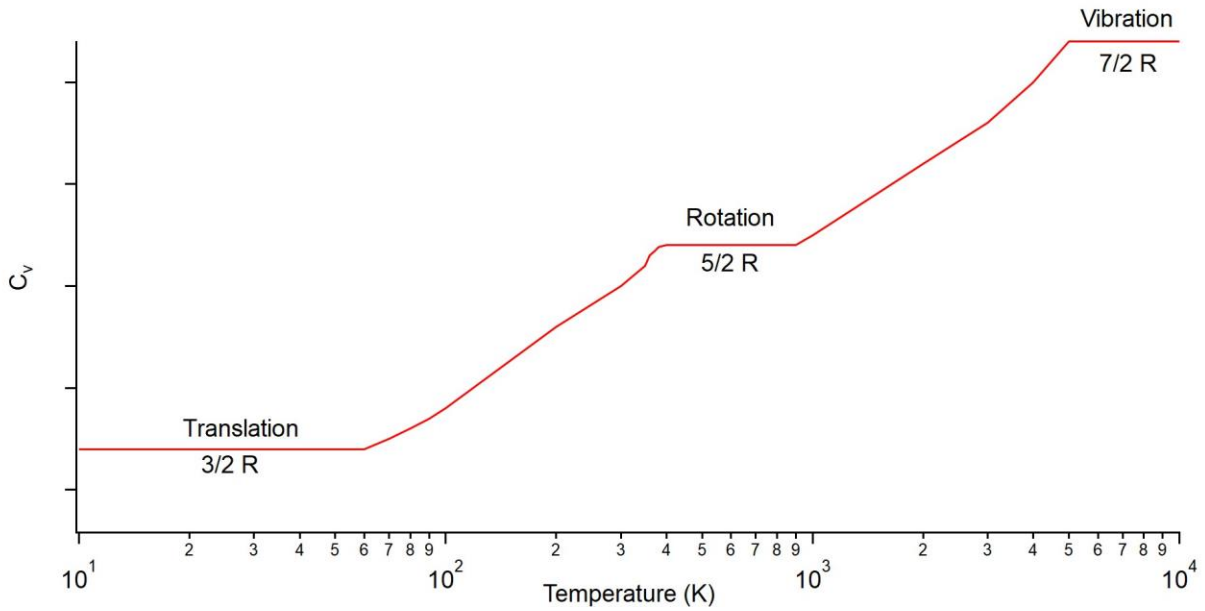

Figure 10-1: Heat capacity of a diatomic molecules as a function of temperature. Only translational degrees of freedom are activated at temperature below few Kelvin

In case of a diatomic molecule at room temperature, most of the thermal energy is distributed between translational and rotational degrees of freedom as vibrational degrees of freedom are not activated at room temperature as can be seen in Figure 1-1. Therefore, if we can cease the translational and rotational motion of diatomic molecule, we can reduce its temperature. Using

classical statistics, the distribution of translational energy as a function of temperature is given by Maxwellian velocity distribution f(v) [8].

$$f(v) = \frac{4}{\sqrt{\pi}}\left(\frac{m}{3kT}\right)^{\frac{3}{2}} v^2 \exp\left(-\frac{mv^2}{2kT}\right) \tag{1.2}$$

The most probable speed v_w is defined as the speed where the distribution has its maximum [7].

$$v_w = \sqrt{\frac{2kT}{m}}$$

The temperature of a gas according to Maxwell-Boltzmann distribution, is directly proportional to its width of its velocity distribution. This temperature is referred as translation temperature or simply temperature of a gas in the field of cold molecules research. Therefore, cold molecules are slow molecules with narrow velocity distribution. Figure 1-2 shows the Maxwell-Boltzmann velocity distribution for a particle of m = 15 amu at 298 and 1 K. As the temperature decreases, v_w shifts towards lower velocity and the FWHM also decreases. Particles move slowly with narrower velocity distribution at low temperature. The rotational temperature as differentiated from translational temperature, is related to the population of internal states and is referred to as internal temperature in the field of cold molecules research. At lower internal temperature, most of the population lies in the lowest rotational states according to the expression below [9].

$$N_i \propto N e^{\frac{-\varepsilon_i}{k_B T}}$$

Here N is the total number of particles, N_i is the number of particles in rotational state i, and ε_i is the energy for quantum state i. Figure 1-3 shows the population of rotational states as a function of internal temperature. As the internal temperature reduces, the population of lower rotational states increases.

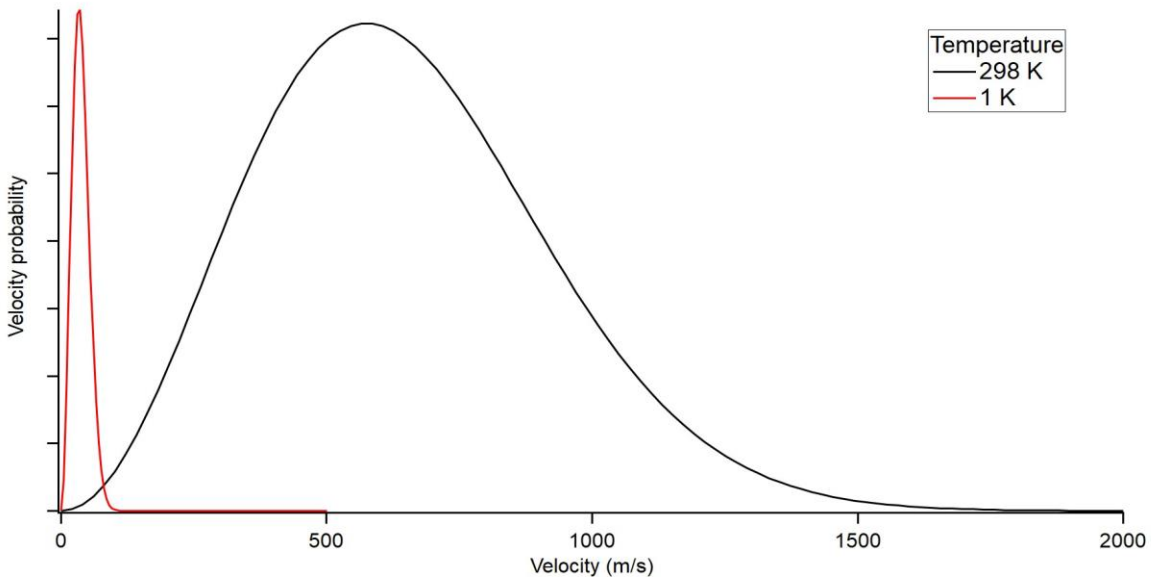

Figure 1-0-2:Maxwell-Boltzmann distribution of a particle with a mass of 15 amu at different temperature. The peaks for the two traces are normalized to each other

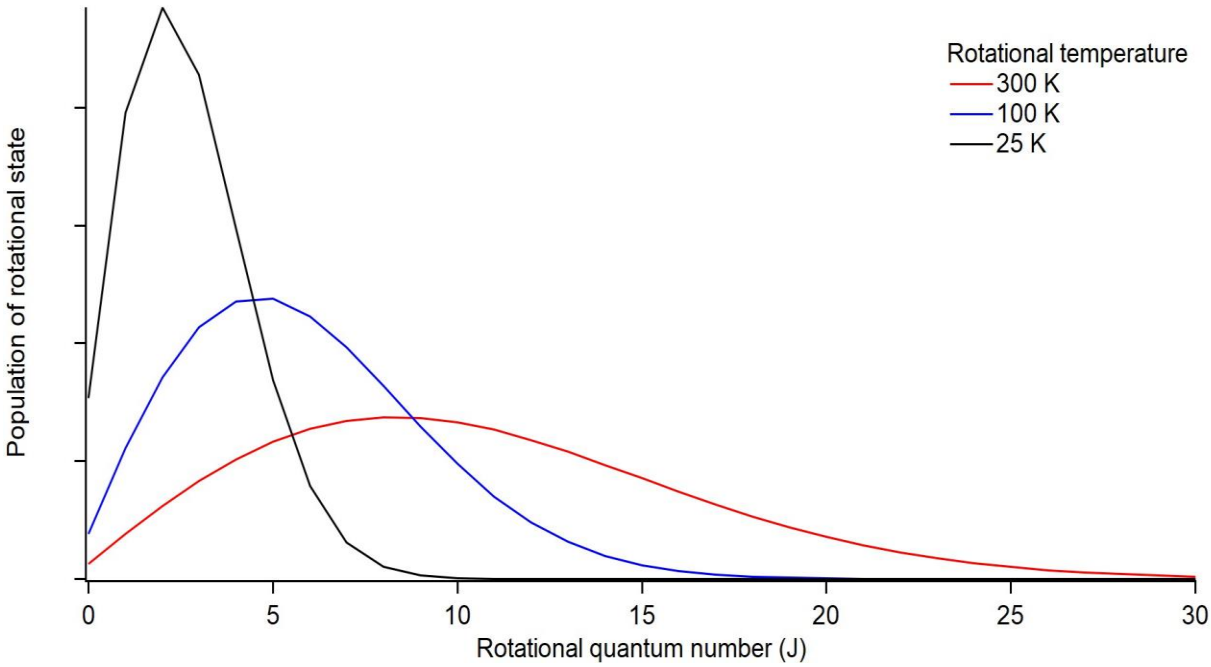

Figure 1-0-3:Population of rotational levels at different rotational temperature for a CO molecule with a rotational constant, B=1.92 cm-1.

1.2 Why do we need cold molecules?

The first ever quantum degenerate state of matter in the gas phase was created in 1995 by cooling Rb atoms to a temperature of 170 nK where most of the atoms occupied the lowest energy level as governed by Bose-Einstein statistics [10]. Other atomic species which have ben cooled to form their BECs are H, ^{4}He, ^{7}Li, ^{23}Na, ^{41}K and ^{85}Rb [11,12,13,14,15,16]. These ultra cold atoms have been used to study the inter particle collisions at very low collision energy which is impossible to study at room temperature. Other important phenomena which have been studied in ultra cold atoms include measurement of parity non conservation in cesium atom [17,18], improving accuracy in optical clocks [19,20,21,22,23], creation of ultra cold molecules [24] and interference between BECs [25]. From a chemist's point of view, the creation of ultra cold molecules had to be the next step in order to expand the knowledge of chemical reactions at low temperature. The only type of chemical reaction which can be studied with atomic system is the combination reaction

$$A + B + M \rightarrow AB + M$$

Where A and B are atomic species and M is a collision partner which is required for conservation of momentum during the reaction. On the other hand, molecular systems can be used to study any type of reaction namely combination, decomposition or displacement reactions.

Decomposition $AB \rightarrow A + B$

Combination $2AB \rightarrow A_2 + B_2$

Displacement $AB + CD \rightarrow AC + B$

The importance of ultra cold molecules is not only restricted to study different chemical reactions

but also includes measurement of physical quantities such as electron's EDM [1], or energy differences between chiral molecules [26] which have very small values such that it cannot be investigated in atomic systems. However, as the number of atoms increase in a molecule, the applicability of laser cooling decreases and it becomes difficult to achieve cold temperature for molecules. The laser cooling technique requires a closed transition cycle as the particles must absorb photons from the laser light to lose their kinetic energy and subsequently emit them in random directions due to spontaneous emission. However, the change in momentum due to one such event is negligible, and the particles need to undergo this event multiple times. In the case of atoms, during spontaneous emission, the atoms decay to their initial state, however, molecules due to their rich internal energy level structure, can decay to different quantum states. This makes it difficult for the molecule to absorb subsequent photons as it becomes off resonance from the laser light. So far, of all diatomic molecules, only alkali dimers have been created in the ultra cold regime by laser cooling of the constituent atoms and then photo associating them to create dimers. This restricts the number of chemical reactions which can be studied at low temperature. In order to bring more chemical species into the ultra cold regime, physicists have been trying to develop new techniques which are applicable to a wider range of molecules such as Stark or Zeeman deceleration [27-35], buffer gas cooling [36-38], counter rotating nozzle [39,40] and velocity filtering methods. These techniques rely on molecular beam manipulation using different force fields. The use of a supersonic expansion for molecular beam is ideal for this purpose as particles move in straight lines with very small diversion and low internal temperature. After the supersonic expansion, the velocity distribution narrows but the molecules move very fast in the lab frame. The application of each technique depends on the molecule of interest. For example, Stark deceleration requires molecules to have a permanent electric dipole moment whereas Zeeman

deceleration is limited to molecules having permanent magnetic dipole moment. Buffer gas cooling can be applied to most molecules which have large thermalization rates with helium. Counter rotating nozzle can also be applied to any molecule except those which exists as solid at room temperature due to technical difficulties arising as a result of the design of counter rotating nozzle.

Table 1-2 [41] lists the molecules which have been successfully cooled using various methods.

Table 1-2: Molecules which have been cooled using different techniques

Method	Molecule	T	N
Photo association	Rb_2, Cs_2, H_2, Li_2 , Na_2, K_2, KRb, RbCs, LiCs, LiRb	50 nK	$>10^5$
Buffer-gas cooling	CaH, CaF, VO, PbO, NH, ND, CrH, MnH	400 mK	$>10^8$
Stark deceleration and trapping	NH_3, ND_3, CO, OH, OD, NH, SO_2, YbF, H_2CO	5 mK	10^6
Zeeman deceleration and trapping	O_2, CH_3, He, H_2	100 mK	$>10^7$
Counter rotating nozzle	O_2, CH_3COCH_3, Ar, Xe, CH_3F	60 m/s	
Laser cooling	SrOH,CH_3F,YbF,YO	100 μK	

The final goal after slowing molecules is to store them inside a trap so that they are nearly stationary and can be subjected to experiments requiring long interaction times with laser radiation. In order to store neutral slow molecules various static traps have been used such as quadrupole traps or anti-Helmholtz magnetic trap which again depend on the molecular properties. Storing

slow molecules in such traps not only permits studies at low temperature but, is a crucial step in order to further reduce the temperature and increase the density for experiments at even lower temperature. Application of techniques such as sympathetic and evaporative cooling can bring down the temperature from mK range to μK range inside such traps.

Table 1-3:Applications of cold molecules and the density required for such experiments [26]

Number density	Temperature	Scientific goal
10^6-10^9	<1 K	Test of fundamental forces of nature
$>10^9$	<1 K	Electric dipole transition
$>10^{10}$	<1 K	Cold controlled chemistry
$>10^9$	<1 μK	Ultra cold chemistry
$>10^{13}$	100 nK	Quantum degeneracy with molecules
$>10^{13}$	100 nK	Optical lattices of molecules

1.2.1 Cold chemistry

A chemical reaction occurs between two reactants to form a new product. Classically, the kinetics can be described by the collision theory of chemical reactions. In summary, the colliding or reacting molecules undergo collisions during a chemical reaction and, only the collisions which can overcome the activation energy barrier are able to form new products. The role of temperature is described by the Arrhenius equation which predicts that the rate constant k, of a chemical reaction is given by [42]:

$$k = Ae^{\frac{-E_a}{RT}}$$

where A is a pre-exponential factor, E_a is the activation energy and T is the temperature. As can be seen from Arrhenius equation, the rate of a chemical reaction increases as the temperature increases. However, at low temperature, the wave nature of reactants starts to dominate the reaction due to the increase in λ_{th} , giving rise to phenomenon such as quantum tunneling, in which reactants tunnel through the potential barrier instead of climbing over it. One such example of a barrier less reaction where quantum tunnelling dominates the reaction dynamics is the formation of methanol from methyl radical and hydroxyl radical [43]. But there are other reaction branches which competes with the formation of methanol. Understanding the formation of methanol at low temperature can provide us new information such that the competing processes in the formation of methyl radical can be suppressed. Non-Arrhenius type behaviour is also possible at lower temperature as the reaction pathway is different. Narvecius et al. observed this effect at a temperature of 10 mK in a reaction between metastable helium and hydrogen [44]. Another application of cold molecules lies in the field of astrochemistry. Many chemical species have been observed in outer space where the temperature is around 3 K. At this temperature the chemical reaction dynamics could be different than at room temperature. Creation of conditions which exist in outer space and study of these reactions inside laboratories can predict the abundance of these chemical species in outer space.

1.2.2 Precision spectroscopy

When a laser beam probes a molecular transition, the resolution of this measurement depends on the transit time in addition to other line broadening factors such as Doppler effect, laser power

and the gas pressure [9]. If a molecular beam travels at a speed v and a laser beam has a diameter d, then the transit time is defined as

$$\tau = d/v$$

Usually, cold gases move very slowly and have low densities. Therefore, spectroscopy of cold gases results in suppression of the line broadening due to transit-time, Doppler effect and gas pressure. The hyperfine structure of ND_3 was recorded for the first time using a slowed beam of ND_3 molecules by a Stark decelerator [45]. The increase in resolution of a spectroscopic measurement allows us to calculate molecular parameters more precisely which can also be compared to data from astrophysical measurements to see any changes in such molecular parameters over time.

2 Experimental techniques

2.1 Supersonic beam

The rapid expansion of gas from the tip of a high-pressure nozzle into an area of low-pressure results in the production of a supersonic beam. The diameter of the nozzle should be smaller than the mean free path of the gas particles in the high-pressure region. As the gas slows out from the orifice of the nozzle, the particles undergo multiple collisions with each other resulting in cooling of internal degrees of freedom. The flow of gases through a nozzle at a pressure P_O, into a region of low background pressure P_B is highly complex. It consists of several regions downstream of the nozzle where the flow must adjust to boundary conditions imposed by the background pressure. The Mach disk location x_M [46] is given by

$$x_M = 0.67 \times d \times \left(\frac{P_O}{P_B}\right)^{\frac{1}{2}} \tag{2.1}$$

The location of Mach disk when P_O = 3000 Torr (4 bar), $P_B = 1x10^{-7}$ Torr with a nozzle diameter of 250 μm, is around 30 metres. The expanding beam before the Mach disk location does not interact and is devoid of any collisions. In our experimental setup a skimmer is usually placed at 5-10 cms downstream of nozzle in order to extract the non-interacting and collinear part of the molecular beam. The diameter of a skimmer is usually 1-4 mm. The skimmer also allows differential pumping such that the pressure in the downstream region of the nozzle is smaller. This reduced pressure is critical to eliminate beam attenuation by background gas collisions during deceleration experiments.

Our sample molecules are very light (NH_3, CH_4), therefore, to reduce mean velocity of the molecular beam, these samples are mixed with heavy noble gases such as Krypton or Argon.

Another advantage in using heavy carrier gases is the low rotational temperature achieved in comparison to light carrier gases such as Helium or Neon. The rotational cooling of a molecular beam increases as the mass of the carrier gas increases [47]. The mean velocity of a gas mixture at a nozzle temperature of T_O, after the supersonic expansion can be calculated based on the equation below [46],

$$V = \sqrt{\frac{2C_P}{W}\left(\frac{\gamma}{\gamma - 1}\right)T_O} \qquad (2.2a)$$

Where C_P is the molar average heat capacity given by

$$C_P = \sum X_i \left(\frac{\gamma}{\gamma - 1}\right) R \qquad (2.2b)$$

And W is the molar average molecular weight given by

$$W = \sum X_i W_i \qquad (2.2c)$$

Here, X_i and W_i are the mole fraction and the molecular weight of the i^{th} component in the gas mixture. Based on the above equation, the mean velocity also depends on the temperature of the nozzle. Therefore, the nozzle temperature is reduced from room temperature using liquid nitrogen to just above the boiling point of the gas to decrease the initial velocity of the molecular beam.

An important aspect of the supersonic expansion is the velocity distribution of molecules. The velocity distribution is characterized by temperature in the longitudinal ($T_{||}$) and transverse direction (T_{perp}) of the molecular beam is related to the FWHM of the velocity distribution in respective directions,

$$T_{||} = \frac{m\Delta v^2}{2k_B} \qquad (2.3)$$

The longitudinal temperature can be easily determined by measuring the time-of-flight distribution of a molecular beam, however, the transverse temperature is more difficult to measure.

Another important parameter to consider in the supersonic expansion is the speed ratio, S. This is defined as the ratio of mean velocity and the deviation in the velocity [48].

$$S = \frac{v}{\Delta v} \tag{2.4a}$$

In 1979, Brusdeylins and Meyer showed that the speed ratio can be calculated as a function of nozzle pressure with [3].

$$S = 5.4(P_O d)^{0.32} \tag{2.4b}$$

Thereby confirming that, nozzle pressure and the velocity spread in a molecular beam are directly proportional to each other. In other words, higher pressure inside the nozzle gives dense and cold molecular beams.

2.2 Zeeman shift of methyl radical

Methyl radical is a planar molecule in ground state with one unpaired electron belonging to D_{3h} point group symmetry [49]. Due to the planar nature of methyl radical, it has zero permanent electric dipole moment. However, due to presence of one unpaired electron, just like any other free radical, it possesses a permanent magnetic moment. Hence, magnetic fields can be utilized to decelerate methyl radicals. Due to the three hydrogen atoms around the carbon atom, methyl radical has two nuclear spin isomers with I=1/2 (para) and I=3/2 (ortho). The rotational angular quantum number and its projection along the molecule-fixed axis are denoted by N and K respectively. Due to nuclear spin statistics, only certain quantum states with N and K are allowed. The rotational ground state is the ortho nuclear spin isomer with N=0, K=0 and the first excited

rotational state is the para nuclear spin isomer with N=1, K=1. Due to the spin of electron (M_s = ±1/2), the degenerate ortho or para states are split in presence of magnetic field. The Zeeman shift for methyl radical, ΔE_Z at high magnetic fields is approximated as [35]

$$\Delta E_Z = g_e \mu_B B_O M_S \tag{2.5a}$$

Or,

$$\frac{\Delta E_Z}{cm^{-1}} = \pm 0.47 \times B_O(T) \; for \; M_S = \pm \frac{1}{2} \, , \tag{2.5b}$$

where g_e is the electron g-factor, μ_B is the Bohr magneton, B_O is the magnetic field. After supersonic expansion, most of the radicals are in their lowest rotational states. The Zeeman shift of methyl radical in the two lowest rotational states is provided in Figure 2-1. of methyl radical in

The states which show a positive Zeeman shift are called low-field seekers (LFS) whereas the states which show a negative Zeeman shift are called high-field seekers (HFS). The upper component of Zeeman shifts of ortho and para states (dotted traces) are LFS while the lower components are HFS. The potential energy of a methyl radical depends on its position in an inhomogeneous magnetic field. Hence, the direction of force also depends on its position. The force on a methyl radical F, is expressed in terms of potential energy V, by taking its gradient as,

$$F = -\nabla V = -\frac{\partial V}{\partial z} = -\frac{\partial V}{\partial B}\frac{\partial B}{\partial z}$$

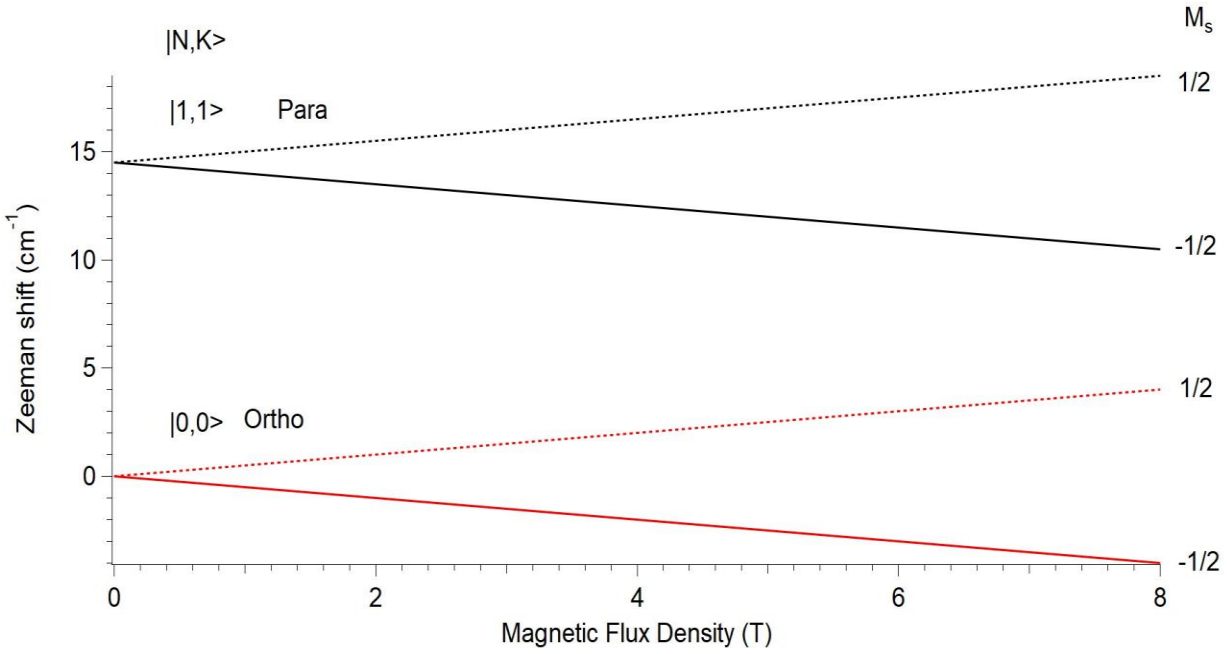

Figure 2-1:Zeeman shift of methyl radical in para (black) and ortho (red) nuclear spin isomers state. The dotted traces show LFS states whereas the solid trace show HFS states. The Zeeman decelerator decelerates the LFS states

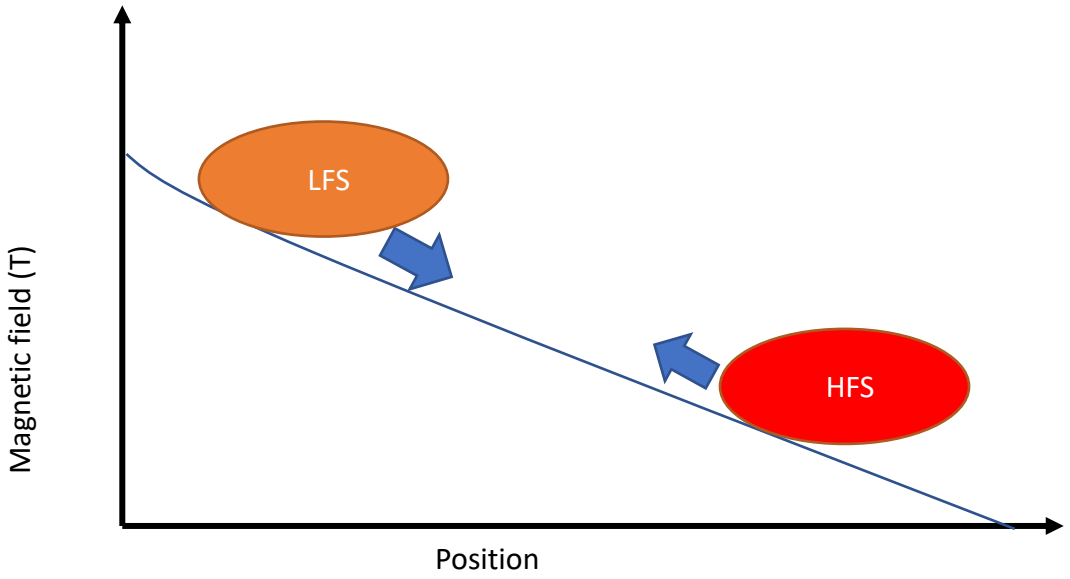

Figure 2-2: Direction of force on the LFS and HFS states in a non-homogeneous magnetic field. The direction of arrow indicates attractive force.

For a LFS, $\partial V/\partial B$ is positive, therefore F is negative in regions where $\partial B/\partial z$ is positive. In other words, LFS are repelled away from high field regions. So, for a LFS molecule, as it enters a magnetic field region where the magnetic field is increasing, it will experience a deceleration force and vice-versa.

2.3 AC Stark shift of ammonia

Ammonia molecule exists in a pyramidal shape in its ground state. We denote the rotational state of NH_3 using J, K and M quantum numbers, where J is the total angular momentum quantum number, K is the projection of J on the symmetry axis of molecule and M is the projection of J on a fixed axis in laboratory frame. Nitrogen atom in the ground vibration state of NH_3 cannot lie in the plane of hydrogen atoms due to a hump in the potential energy at this position as shown in Figure 2-3 [84]. However, due to finite barrier height, nitrogen atom can move across the plane. The movement of the nitrogen atoms from one side of the plane of hydrogen atoms to the other is called as tunnel effect as classically it is forbidden. As NH_3 can exist on both sides of the plane, the motion of nitrogen atoms from one side of the hydrogen atoms plane is similar to vibrational motion but due to the hindered motion as a result of potential energy barrier, this vibrational motion is much slower than normal vibrational motions. The tunneling frequency lies in the MW region (0.36 cm^{-1}) whereas the normal vibration motion lies in the infrared region (950 cm^{-1}). The tunneling frequency is the result of the energy difference between the two eigen states which are solutions of the system describing the tunneling of nitrogen atoms across a barrier which is symmetric. The upper state which has more energy is anti-symmetric whereas the lower energy state is symmetric.

The interaction of polar molecules with an AC field is described by AC Stark effect. In comparison to DC Stark effect, the magnitude of AC Stark effect is much higher at same electric field intensity.

When an AC field is tuned close to the resonance frequency of a two-level system in any polar molecule, the two energy levels shift due to AC Stark effect. In case of NH_3, the two-level system is the inversion doublet in the vibronic ground state of para-NH_3 with a transition frequency of 23.695 GHz. In the semi-classical treatment, the AC stark shift for NH_3 is given as [82]

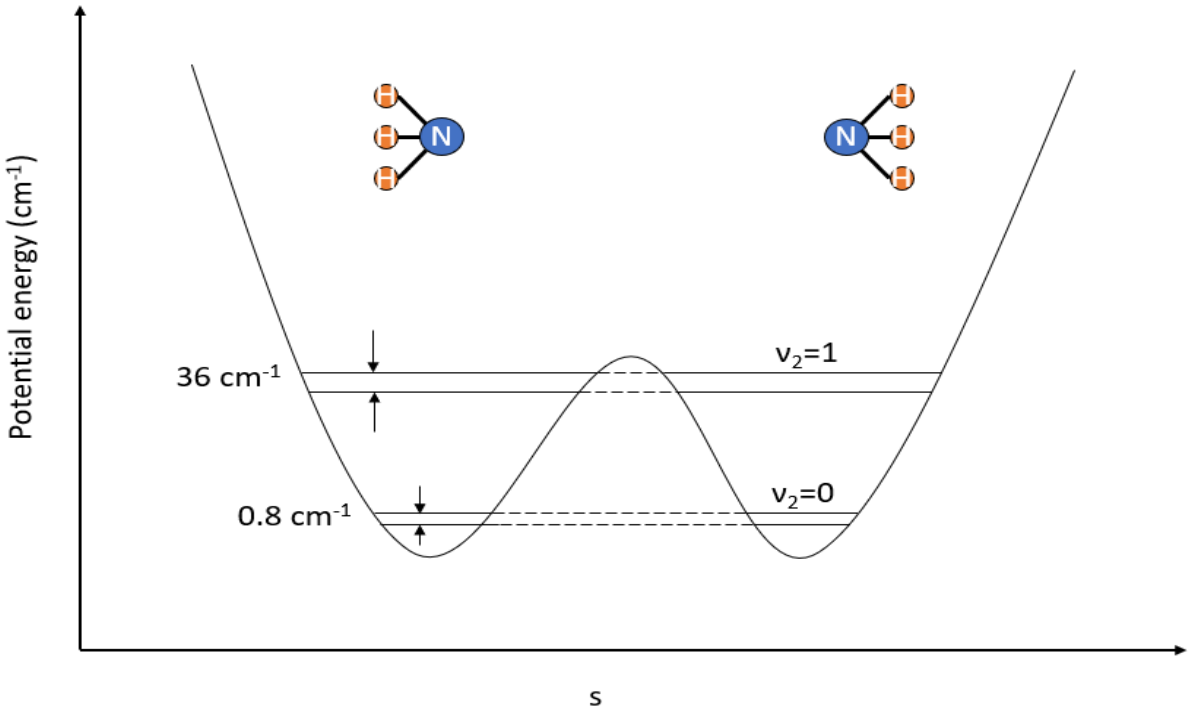

Figure 2-3: Potential energy curve of ammonia showing a double well potential. The y axis is the potential energy and the x axis denoted the distance of nitrogen atom from the plane of hydrogen atoms. The hump in the center denotes s=0 when nitrogen atom is in the plane of hydrogen atoms.

$$U = \pm\sqrt{\left(\frac{h\delta}{2}\right)^2 + \left(\frac{\mu EKM}{2J(J+1)}\right)^2} \pm \frac{h\delta}{2} \tag{2.6}$$

where, E is the electric field of MW, J,K,M are the quantum numbers describing the state, μ is the permanent dipole moment of NH_3 and $\delta = (\nu_{MW} - \nu_0)$ is the detuning of the applied MW frequency

(ν_{MW}) from the inversion transition frequency (ν_0). Thus, the AC stark shift depends on the magnitude of detuning frequency, electric field and the sign of detuning. The sign of detuning can determine whether a molecule will behave like a low field seeking (LFS) or high field seeking (HFS). This is illustrated in Figure 2-4 which shows that by changing the sign of detuning, AC stark shift also reverses in sign. Thus, any molecule can be trapped inside a cavity using MW radiations by selecting the appropriate detuning frequency. In addition to changing the sign of AC stark shift, smaller detuning frequency gives larger AC stark shift. Zero detuning should be voided as it causes undesired transitions between the two levels.

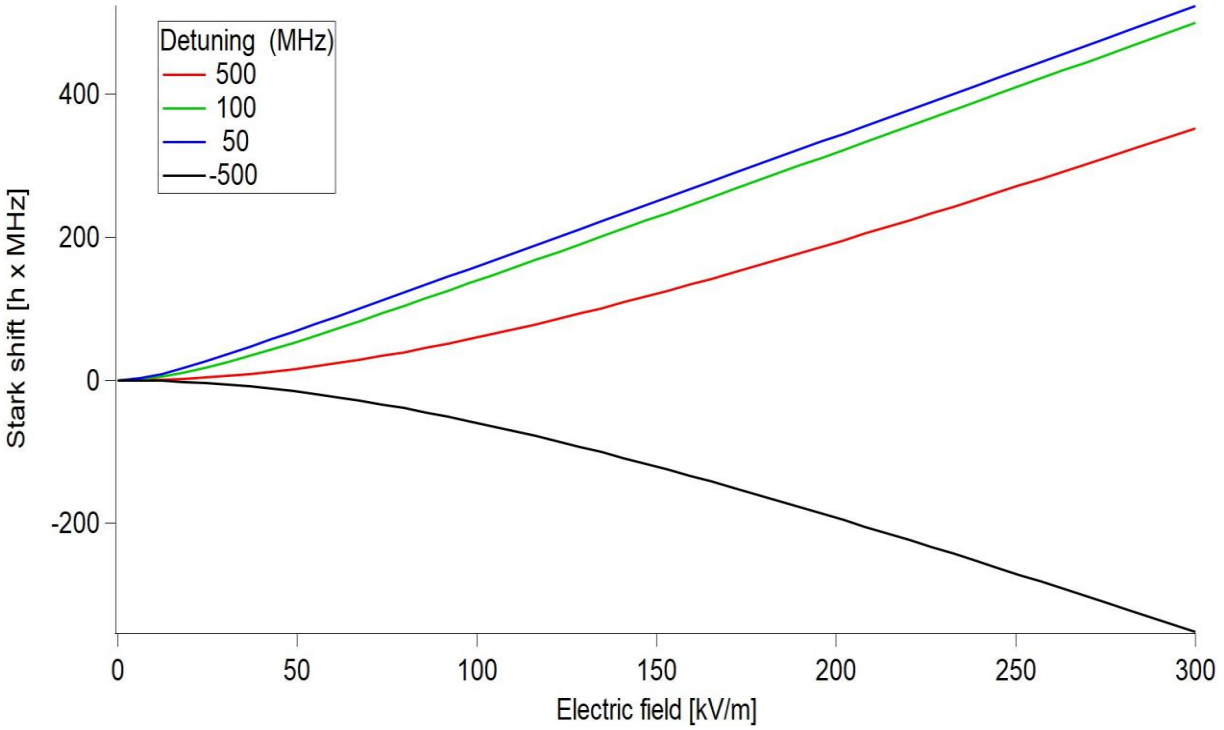

Figure 2-4: AC stark shift for NH_3 in the lower level of the inversion doublet at different detuning frequency as a function of electric field.

A multiphoton transition is an important issue for the MW trap. In the case of NH_3, the lowest excitation except the inversion transition is J=1→2 rotational transition. This transition energy is 4B = 1.2 THz. This transition corresponds to $4B/\nu_0 \approx 50$ photon process and is negligible.

2.4 Detection method

In this thesis, three molecules have been used as the samples in respective experiments. In general, the molecules are ionized using a laser radiation which can be resonant or non-resonant to the energy levels of the molecule. For NH_3 and methyl radical, 2+1 REMPI scheme whereas for acetone molecules, non resonant multi-photon ionization was used.

The detection scheme used in all the experiments in this thesis is based on the principle of time of flight mass spectrometry [50]. A laser is used to ionize the sample molecule inside a vacuum chamber. The laser ionizes the sample molecule in between two metallic plates which have holes in the center for the transmission of ions towards a detector. We use a Micro channel plate detector which can be used to detect positive or negative charged particles, X-rays, UV rays and gamma rays. In our case, the positive ions are directed towards the MCP using the metallic plates where the arriving charged particles generates secondary electrons. These secondary electrons are generated inside small glass capillaries which have a diameter of 4-25 um forming the front surface of the MCP. The signal arising due to these secondary electrons is what we observe on an oscilloscope.

A basic TOF mass spectrometer consists of a repeller plate, extractor plate and the detector. As shown in Figure 2-5, the repeller plate is supplied a DC voltage which is higher than that of extractor plate. In the Figure 2-5, the repeller plate is supplied a voltage of +1200 V and the extractor plate is supplied a voltage of 600 V. Additional plates can be stacked with these two

plates in order to increase the efficiency of ion detection. When a laser ionizes a neutral molecule from a molecular beam traveling across the plates, the positively charged particle with a charge +q experiences an electric field E due to the potential difference between the two plates. The force, F on the charged particle in this region is given by,

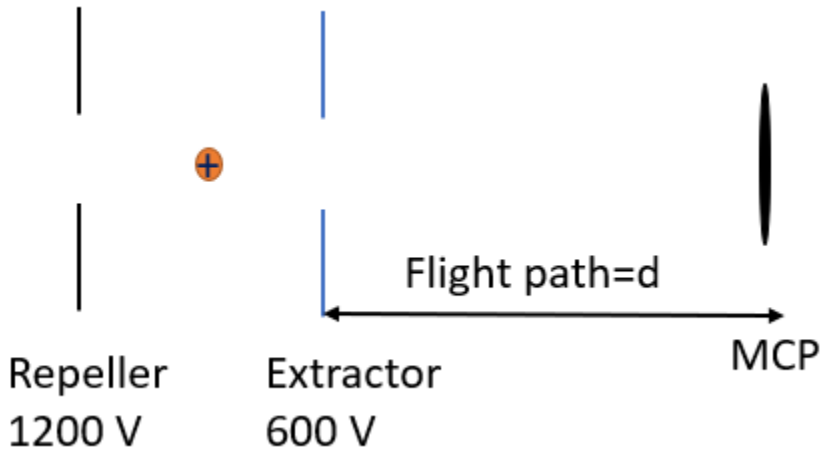

Figure 2-5: Basic principle of time of flight mass spectrometry

$$F = qE$$

The acceleration, a of this particle of mass m is given by

$$a = \frac{qE}{m}$$

Once the particle exits the extractor plate, it travels towards detector in a field free region. Since the acceleration is inversely proportional to the mass of a particle, heavier particles arrive later at the MCP detector. In this way, the ionized particles are resolved based on their mass. If we know the time of arrival, t_1 of a particle whose mass is m_1, then the arrival time t_2 of a known mass m_2 can be easily calculated as both particles have same kinetic energy after the extractor plate.

$$\frac{1}{2}m1 \times {v_1}^2 = \frac{1}{2}m2 \times {v_2}^2$$

$$v1 = \frac{d}{t_1}$$

$$v_2 = \frac{d}{t_2}$$

$$t_2 = \sqrt{\frac{m_2}{m_1}}t_1 \tag{2.7}$$

2.4.1 Methyl radical

The electronic configuration of a methyl radical in its electronic ground state is [51]

$(1a_1')^2(2a_1')^2(2e')^4(2a_2'')^1$, X_2A_2"

Figure 2-6 shows the various Rydberg states in a methyl radical [6]. In our experiment, the methyl radical is detected via a 2+1 REMPI scheme. Two photons are absorbed by a methyl radical and the $2pa_2$" electron is promoted to 4p A_2" state, after which one more photon is used to ionize it.

The two photon selection rules for this transition allows for ΔK=0, ΔN=0, ±1, ±2 rotational branches. Additional transition rules due to rovibronic symmetry requirement [10] forbids ΔK=0, ΔN=±1 transition for K=0 levels.

The wavelength used to excite methyl radical upon absorption of two photons is 286.3 nm. This wavelength light is generated by using a dye laser which is pumped by a 10 Hz Nd: YAG laser at 532 nm. The dye used for this purpose inside the dye laser is Rhodamine 6G which is mixed with methanol. Typically, 5-6 mJ/pulse is used in the experiments although the maximum output from the dye laser is around 15 mJ/pulse.

2.4.2 Ammonia

Ammonia is also detected by 2+1 REMPI process. An ammonia molecule is excited to C (0) excited electronic state by absorption of two photons at 63866 cm-1 [52]. This light is also generated using a dye laser which is pumped by a 10 Hz Nd: YAG laser at 532 nm. The dye used in this case is DCM which is mixed with Methanol. The ammonia molecule is excited from the lower level of the inversion doublet to the excited electronic state C with a vibration quantum number = 0. The selection rules for this transition are:

$$\Delta J=\Delta K=0 \text{ or } \Delta J=2,\ \Delta K=0$$

We also used other Rydberg states such as B (5) at 64000 cm-1 and C (1) at 64710 cm-1 which probes the upper level of the inversion doublet. But the C (0) state was used for detection in measurement of AC stark shift measurements. This was due to stronger signal achieved while using the C (0) transition. The B (5) transition was at least 10 times weaker than the C (0) transition. In addition to detection of NH_3 using 2+1 REMPI, a LIF detection scheme was also attempted. In the same chamber, a PMT tube for LIF detection and a MCP detector for 2+1 REMPI detection were installed. We could not see any LIF signal from the ammonia molecular beam whereas at the time, we saw ionized ammonia molecules hitting the MCP detector. No literature reports were found reporting the LIF detection of ammonia on a molecular beam however, LIF detection was reported for a glass cell filled with NH3 at an excitation wavelength of 304 nm and an emission wavelength of 565 nm [53]. LIF was needed for detection of NH_3 molecules inside the Fabry Perot cavity but after installing ion-optics for Fabry Perot cavity, the LIF detection scheme was no longer needed.

2.4.3 Acetone

Work done by T. Gierczak et al [54] where they measured the absorption cross section of acetone in a wavelength range of 215-349 nm shows that absorption cross section of acetone peaks around 274 nm with a value of 4.94 x 10^{-20} cm^2. In our counter rotating nozzle experiment, the acetone molecules are ionized using multi-photon ionization at 266 nm at which the absorption cross section is 4.49 x 10^{-20} cm^2. The light is generated from the fourth harmonic generation of a Nd: YAG laser. The acetone molecule is fragmented into CH_3CO and CH_3 fragments following absorption at 266 nm at a laser energy of 5 mJ/pulse.

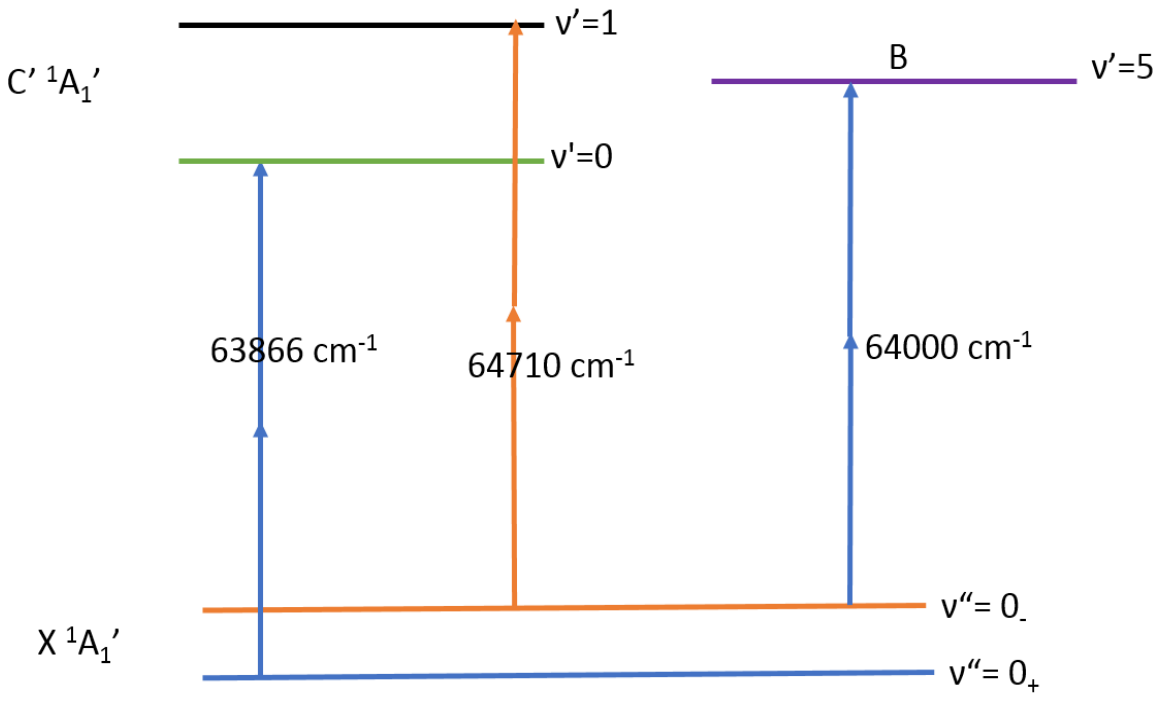

Figure 2-6:Rydberg energy levels for NH3 using two photon absorption

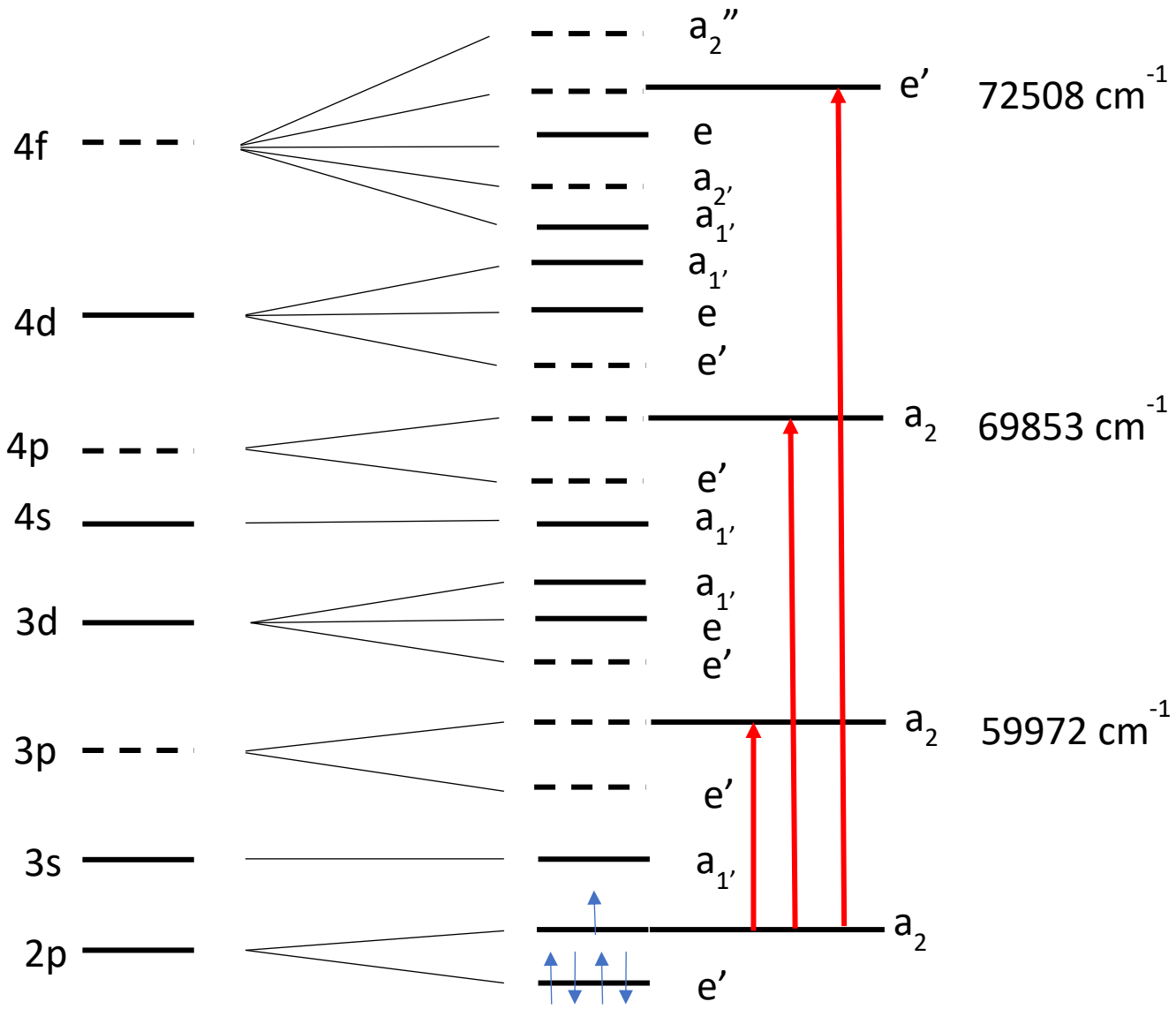

Figure 2-7: Molecular orbital levels of methyl radical. The solid lines indicate one photon allowed transitions from the 2p2 A2`` ground state. Dashed lines indicate energy states accessible by multiphoton transitions. Red lines indicate two photon transition. We use the 4p Rydberg state.

3 Optimization of methyl radical generation

3.1 Introduction

Many techniques have been developed to produce CH_3 molecular beams, including pyrolysis [55, 56, 57], photo dissociation [58, 59] and discharge sources [60, 61]. However, only the pulsed discharge sources have been shown to yield cold molecular beams with rotational temperatures of around 25 K [60, 61]. Ishiguro et al. used a supersonic jet expansion combined with a discharge modulation technique [61], and Davis and co-workers have developed a shaped plate discharge source (slit discharge) to produce cold radical beams [60, 62].

In this chapter, we present the comparison of a plate discharge and a dielectric barrier discharge (DBD) source in combination with a home-built pulsed valve for the generation of rotationally cold CH_3 radical beams. Both discharge techniques are widely used in industrial applications [63] and they have already been used to produce molecular radicals and electronically excited atoms and molecules in supersonic jets [64-68]. The two methods differ in terms of the underlying discharge mechanism and in terms of their technical complexity.

The realization of a DBD is technically more demanding compared to the set-up of a plate discharge. A simple and robust two-plate electrode scheme can be used to ignite a DC discharge at relatively low voltages and at intermediate current strengths in the glow regime [69]. In this regime, the nozzle does not suffer from sputtering, and high electron excitation energies, which would lead to a heating of the gas pulse, are avoided. For the operation of a DBD, several AC high voltage pulses are applied to the electrodes, which are shielded from their surroundings using a dielectric material. This mode of operation ensures that the discharge current is kept at very low values [63, 66]. A DBD source has been shown to generate very cold and intense supersonic beams

[66, 67]. Since the discharge is initiated in filaments, which are uniformly spread over a large surface, the formation of highly energetic species through arcing is prevented. It was therefore of interest to investigate whether a DBD can also be used as an efficient CH_3 radical source.

The optimization of methyl radical generation was done with a different experimental setup such that there was no decelerator involved. Doing so with the Zeeman decelerator was difficult as the flight distance of the molecular beam was around 1 metre. At such a large distance, the molecular beam density at the detection point resulted in poor signal to noise ratio, which made it difficult for comparison at different condition.

3.2 Experimental setup

The experimental setup consisted of a CRUCS nozzle, a skimmer with a diameter of 2 mm, ion-optics and a microchannel plate for detection of positively charged ions. The source chamber housed the nozzle and skimmer whereas the detection chamber housed ion-optics and MCP detector.

Molecular beams of CH_3 radicals are formed by a supersonic expansion of the CH_4 gas mixture followed by bond cleavage initiated by one of the two discharge sources described below. Both sources are directly attached to the front plate of the valve (see Fig. 3-1).

The plate discharge source, which is schematically shown in Fig. 3-1, is based on the design described by Lewandowski et al. [64]. It consists of one insulated, stainless steel electrode plate of the same outer diameter as the valve with a hole of 3 mm diameter and a thickness of 0.7 mm mounted to the valve head. The electrode is set to high negative voltage, and the valve head serves as the ground electrode. The electrode is insulated against the valve using a polytetrauoroethylene (PTFE) spacer (outer diameter as the valve, 7 mm hole diameter and 2.5 mm thickness).

In our case, the supersonic expansion creates conditions of a steady charge flow that prevents the discharge from arcing [60, 70], and thus also avoids an unwanted heating of the supersonic beam. Such heating would be caused by the high current flow along very distinct and spatially small paths. We did not observe an increase of the beam temperature when the duration of the discharge pulse was increased. For this reason, we have applied DC voltages to the electrode during the experiments described here. Due to the voltage applied to the electrode, the direction of the gas flow is directed against the drag of the electrons.

In contrast to schemes in which the electrode voltages are pulsed on and off for very short time periods [64], we found that the discharge process can be driven in the glow regime, i.e., without arcing, at relatively low DC voltages of around -1 kV. To ensure that the discharge is operated in the glow regime, we monitor the applied voltage using a voltage probe. In the case of arcing, a strong and rapid decrease of the voltage is observed (Fig. 3-2). In contrast to that, a glow discharge is characterized by a much smaller and less abrupt voltage drop. In our setup, the use of an additional glow filament for the generation of seed electrons for the discharge, as reported in Refs. [64] and [71], was not required for the stable operation of the discharge unit. To optimize the plate discharge source, the amplitude of the electrode voltage was varied between -0.6 kV and -1.6 kV. For comparison with the plate discharge source, we used a dielectric barrier discharge head (DBD) [72] in combination with a CRUCS valve of the same dimensions as detailed for the plate discharge setup above. Apart from the pulsed valve assembly, the experimental setup is identical to the plate discharge setup. The alumina (Al_2O_3) nozzle for the DBD source (250 μm orifice diameter) has a 40-degree opening angle and a parabolic shape. The ring electrode inside the DBD head is driven by a ferrite-core step-up transformer built in-house which is optimized for the generation of peak-to-peak AC voltages up to 5 kV at a frequency of 1 MHz. The transformer is externally triggered

by two externally programmed pulse trains from a commercial digital delay generator. In the experiments, a fixed number of 0.5 μs long TTL pulses with a gap of 0.5 μs is used which results in a time period of 1 μs for each channel. The TTL pulse trains of each channel are offset by 0.5 μs with respect to each other. The external generation of the DBD pulse sequence allows for the optimization of the time delay between the AC voltage pulse for the DBD source and the pulsed valve, and it is used to adjust the duration of the AC voltage pulse. The operation of the discharge source is monitored by using a fast photodiode (Thorlabs, APD38-A) mounted to a window in the source chamber. For the experimental characterization of the DBD source, both the peak-to-peak voltage, U_{DBD}, and the number of AC voltage periods contained in a pulse train, N_P, were adjusted. The discussion below is limited to U_{DBD} = 3.0 kV and 4.4 kV and to N_P = 8 and 120 for the following reasons: CH_3 radical signal is only observed at $U_{DBD} \geq 3.0$ kV and $N_P \geq 8$, and arcing starts to occur at $U_{DBD} > 4.4$ kV which in turn leads to large fluctuations of the signal intensity. For $N_P > 120$, no further increase of the CH_3 signal intensity was observed. In addition to that, for N_P, the delay of the pulse train with respect to the falling edge of the valve trigger was optimized to the maximum of the gas pulse. For $N_P \geq 120$, the DBD pulse train covered the full duration of the gas pulse.

To detect CH_3 radicals, [2+1]-resonance-enhanced multiphoton ionization (REMPI) of the molecule via the 4p Rydberg state is used in combination with mass-selected ion detection in a Wiley-McLaren-type ion-time-of-flight spectrometer. For this, laser light at 573 nm at a 10 Hz repetition rate is generated by a Nd: YAG-laser-pumped, pulsed dye laser (Sirah, Precision Scan) and subsequently frequency-doubled in a BBO crystal (9 mJ pulse energy, 8 ns pulse duration) to yield the desired laser radiation at 286.3 nm. The laser beam is focused into the interaction volume using a lens (350 mm focal length). The methyl ions produced are accelerated onto an MCP

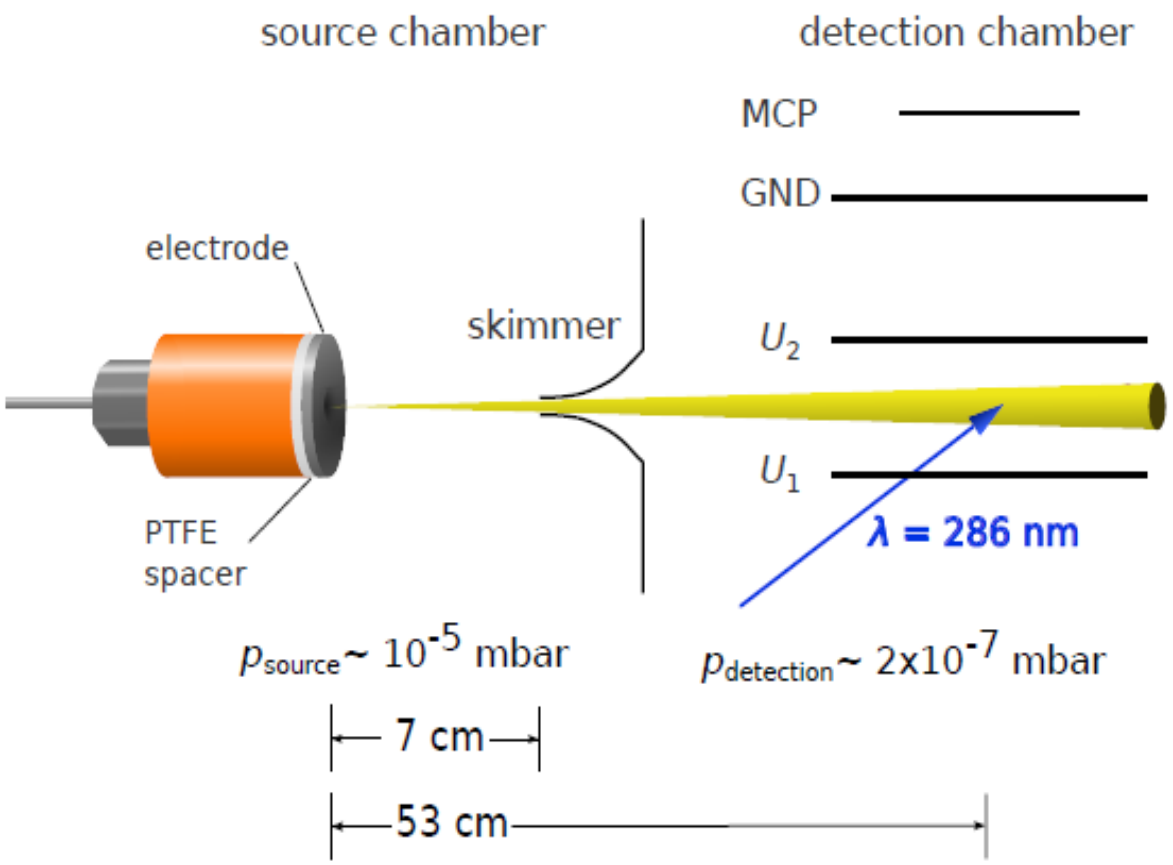

Figure 3-1: Experimental setup of the test chamber used to optimize the generation of methyl radicals. The source chamber consists of a CRUCS nozzle, a discharge plate or DBD head, a skimmer with a diameter of 2 mm. The detection chamber houses the repeller and extractor plates which together with a MCP plate are used to detect laser ionized methyl radicals

detector perpendicular to the molecular beam axis by applying DC voltages of U1 = 1200 V and U2 = 600 V to the extraction plates, respectively. The use of DC extraction voltages prevents the detection of ions produced during the discharge process.

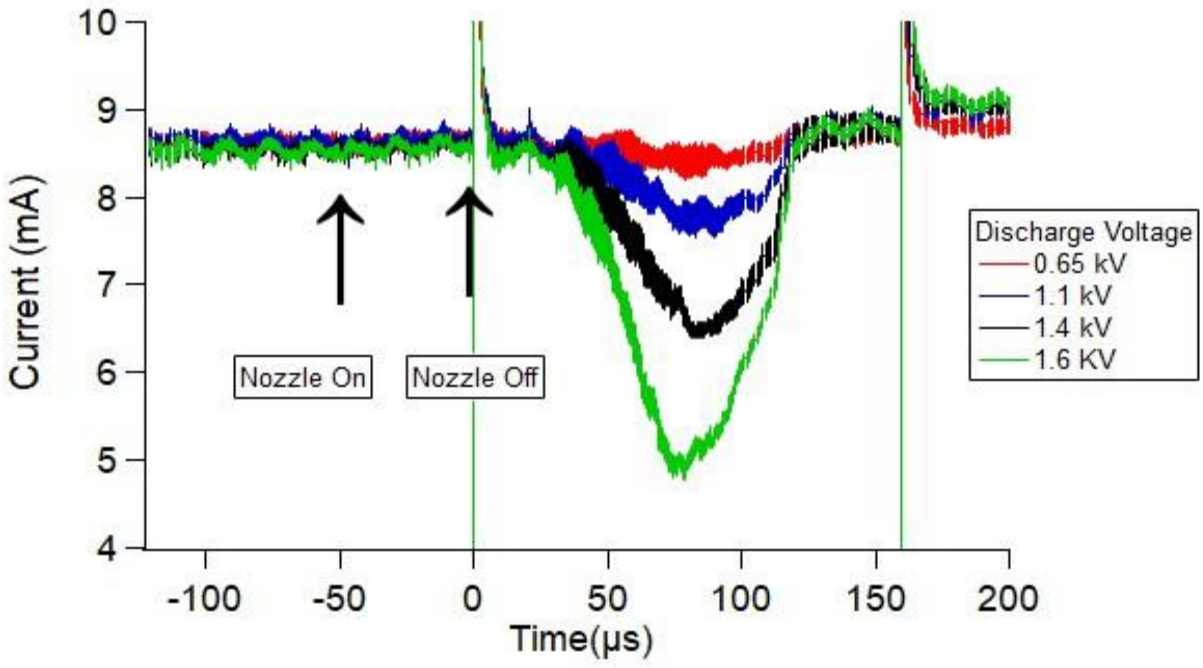

Figure 3-2: Current profiles of the plasma generated in the gas produced after the supersonic expansion from the CRUCS nozzle. The discharge pulse is turned on at the same time as the nozzle with a duration of 160 us. The peaks at the beginning and the end are due to switching noise of the HV switch.

3.3 Results and discussion

CH_3 beam TOF traces for both discharge methods are shown in Fig. 3-3. For clarity, only a selection of traces is given. As can be seen from Fig. 3-3, similar CH_3 radical intensities can be observed for both discharge sources under certain experimental settings. For the plate discharge, we have found that radical production sets in at $U_{PD} > - 0.6$ kV, and a maximum in signal intensity is measured at around -1.1 kV. Above this voltage, a decrease in signal intensity and a significant broadening of the TOF spectrum - which is indicative of a significant heating of the beam by the discharge - is observed. As the voltage is increased, the maximum of the TOF profile is shifted to shorter times, i.e. the beam velocity is increased. The plasma generated during th discharge pulse near the nozzle consists of negatively charged particles which are

3.3.1 Time of flight profiles

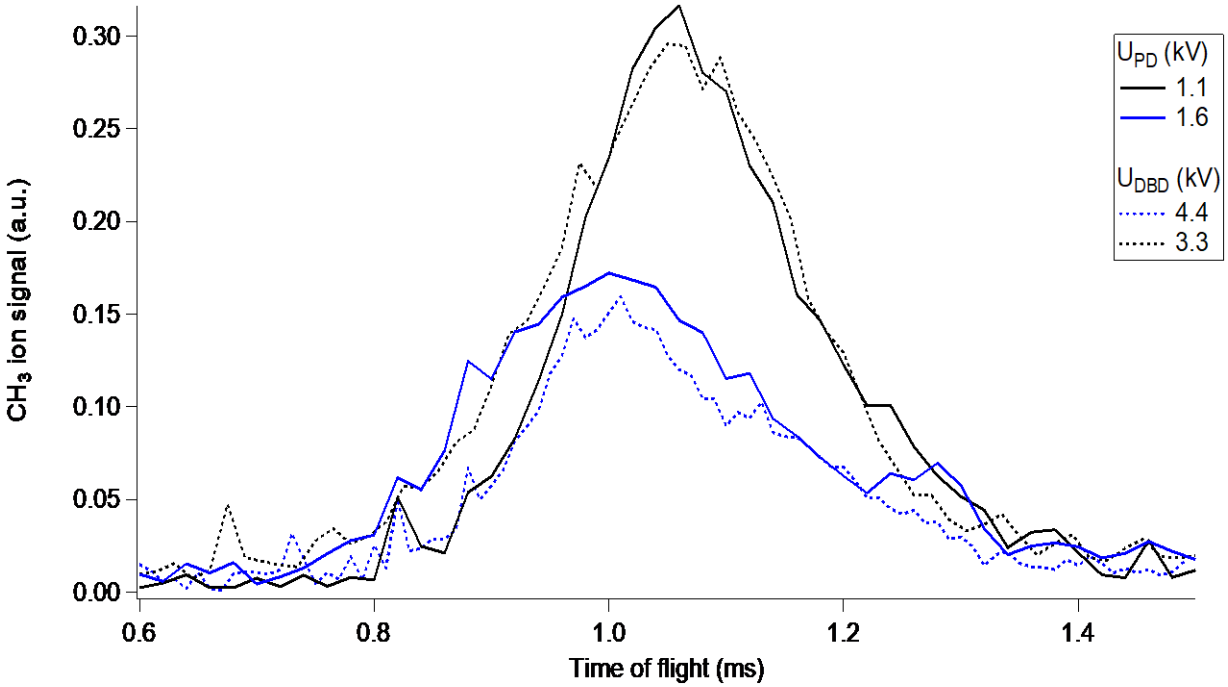

Figure 3-3: CH_3 beam TOF traces at a two-photon wavenumber ν = 69852.8 cm^{-1} for the plate discharge source (solid) and the DBD source (dotted trace) measured using the most optimum discharge conditions using CH_4 as a radical precursor.

attracted towards the skimmer. The voltage applied on the plate is negative, therefore the electric field points towards the skimmer.The voltage applied on the plate is negative, therefore the electric field points towards the skimmer in the region between the skimmer and discharge plate. Therefore a negatively charged plasma is accelerated more towards the skimmer as the dishcharge plate voltage increases.

For the DBD source, the CH_3 signal intensity is increased as the applied voltage U_{DBD} is raised. The highest CH_3 radical yield is thus observed at the highest voltage U_{DBD} that can be applied without causing arcing, and for long pulse trains. At lower values of U_{DBD}, a shift of the mean velocity to slightly higher values is observed. This can be due to an asymmetric density profile of the gas pulse, i.e. due to a higher intensity of the molecular beam at earlier times.

Table 3-1: Summary of beam parameters at different discharge voltage for plate discharge.

Discharge voltage (V)	**-0.65**	**-1.1**	**-1.6**
Mean beam velocity(m/s)	510	540	560
FWHM(%)	17	24	35
Relative beam intensity (a.u.)	0.6	1	0.55

Table 3-2: Summary of beam parameters at different discharge voltage for DBD.

Discharge voltage (V)	**-3.3**	**-4.4**
Mean beam velocity(m/s)	555	550
FWHM(%)	30	28
Relative beam intensity (a.u.)	0.33	0.87

3.3.2 Rotationally resolved spectra

Figure 3-4 shows the rotationally resolved frequency spectra(REMPI) using the plate discharge at different discharge voltage. The REMPI spectra was obtained setting the laser delay time from nozzle when the ion yield is maximum and the laser frequency is varied. The spectroscopic assignements are labelled as Q, R and S which corresponds to $\Delta N=N'-N''=0,1$ and 2 respectively. Here, N' and N'' denotes the rotational angular momentum quantum number for the excited and ground electronic state respectively. As can be seen from the relative intensities for S0 or R2 transitions, there is not a significant change for these transitions which implies that the rotational cooling is not affected as much as the translational coling as a function of discharge voltage. Figure 3-5 shows the REMPI spectra for plate discharge and the DBD source. The rotational temperature from the two discharge sources were comparable as was the case for the intensity of the beam. Judging from the energy-level structure of the molecule, we can deduce a rotational temperature of < 15 K. This means that the heating of the supersonic beam at high discharge voltages only

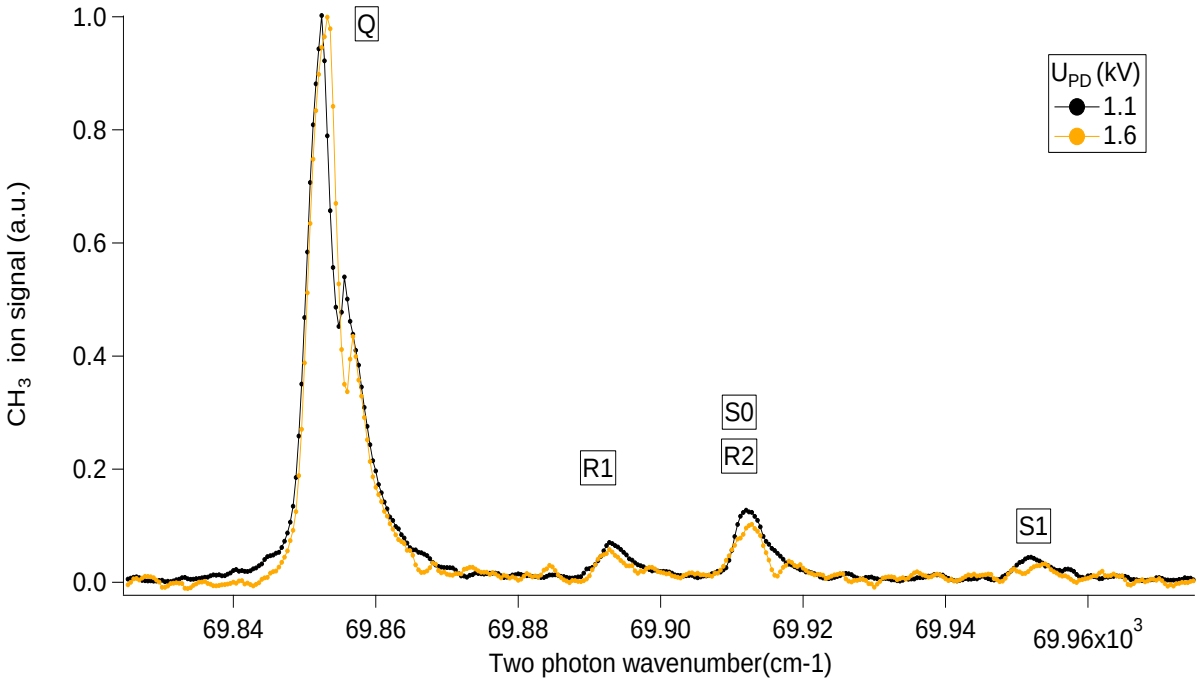

Figure 3-4: Rotationally resolved frequency spectra of methyl radical molecular beam at different discharge voltage

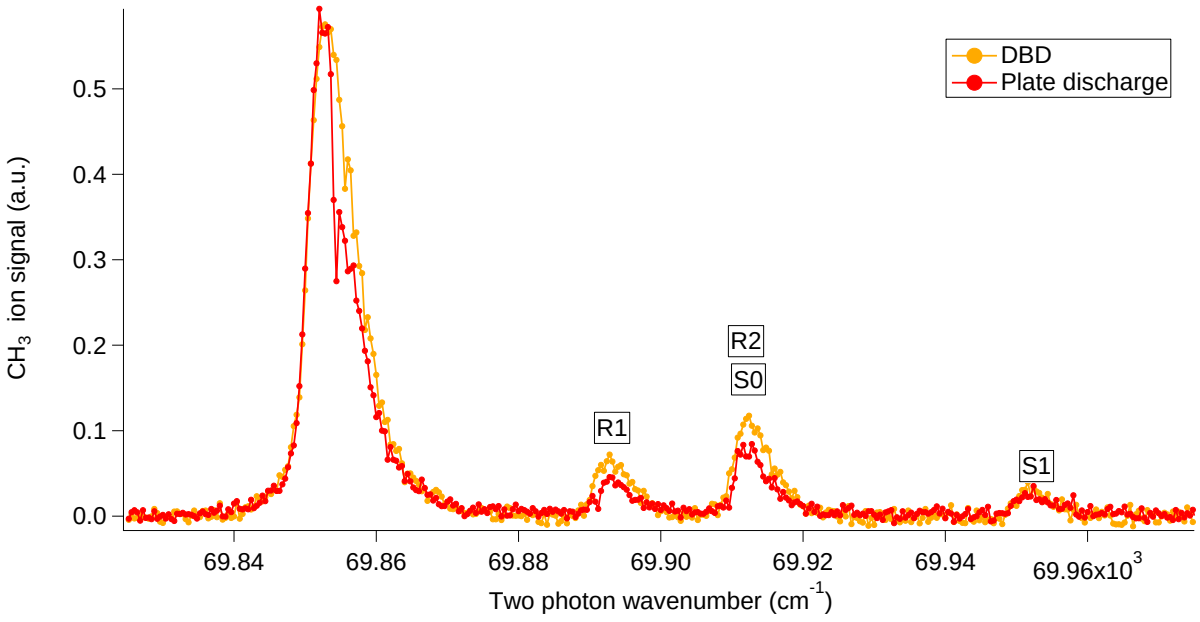

Figure 3-5: Rotationally resolved REMPI spectra of CH_3 obtained using the plate discharge source and the DBD source. For the plate discharge source, U_{PD} =-1.1 kV was used. For the DBD source, a voltage of UDBD = 4:4 kV was applied and a pulse train with N_P = 120 was used. All traces are normalized to the maximum signal intensity at ν= 69852.8 cm^{-1} (Q branch). The dip in the plate discharge spectrum at ~ ν = 69855 cm^{-1} is an experimental artifact caused by instabilities in the laser system.

affects the translational motion and thus the longitudinal beam temperature of the molecules in the supersonic beam. This finding is of interest for applications in spectroscopy and supersonic beam deceleration experiments, where not only the velocity distribution of the beam is important but also the population of internal states plays a crucial role.

3.4 Conclusion

We have found that both a plate discharge and a DBD source can yield cold supersonic beams of methyl radicals of similar intensity. The relative velocity obtained from the TOF profiles indicates that both discharge sources lead to an increase of the longitudinal beam temperature, and this effect is highest at high electrode voltages. In contrast to that, the rotational cooling of the beam into the lowest-lying rotational state of each nuclear-spin isomer, induced by inelastic collisions during the supersonic expansion, is not affected by the discharge process. However, in terms of technical complexity, a plate discharge source is much easier to set-up compared to a DBD source. In particular, a plate discharge source does not require special ceramic and magnetic discs, and additional electronics equipment is not necessary for the generation of a pulse train.

4 Magnetic trapping of Methyl radicals and collisions with helium and argon atoms

4.1 Introduction

Recent developments in molecular deceleration [73] now make it possible to control the translational motion of molecules and create extremely slow molecular beams. Among various molecules, free radicals having unpaired electron(s) are of interest in relation to cold scattering because of their high reactivity towards other molecules and substances. Since molecules with unpaired electron(s) always have a nonzero magnetic moment, it is natural to use magnetic fields for the deceleration, i.e., Zeeman deceleration [74-79], and as well as for trapping of these reactive species. So far, only two diatomic molecules, He_2 [79,80] and O_2 [81,82] have been successfully decelerated by Zeeman deceleration, except for our preliminary work on methyl radicals (CH_3) [83]. The magnetic trappings of CaH [84], CaF [85], NH [86,87] and OH [88] were reported following buffer gas cooling, and optical loading as well as Stark deceleration. The trapped molecules were applied to high-resolution spectroscopy [89], cold collision experiments [90] as well as evaporative cooling [91]. However, all the molecular candidates that have been magnetically decelerated and trapped have been limited to diatomic species. In this chapter, we describe the magnetic trapping of CH_3, the simplest organic polyatomic radical, in the ground rotational state for the first time for longer than a second, after slowing down its velocity by well-controlled pulsed magnetic fields. Creating cold ensembles of the methyl radical is of particular importance. CH_3 is an ideal system for long trapping experiments, because CH_3 does not possess an electric dipole moment [92], and therefore there is no trap loss for CH_3 due to rotational excitation by blackbody radiation [93]. Furthermore, it has been predicted that sympathetic cooling

of CH_3 with ultra cold (< 100 μK) alkaline-earth metals may be possible, thereby enabling the further cooling of CH3 into the ultra cold regime (< 1 mK) [95]. Achieving long trapping times and lower temperatures, by sympathetic cooling, are both imperative for the realization of molecular BEC. Another key feature of CH_3 is that it exists as two spin isomers, para (I ¼ 1=2) and ortho (I ¼ 3=2) species, which is an ideal system to solve the outstanding problem of understanding the rate and mechanism of nuclear spin conversion between spin isomers [94] as well as the separation of different nuclear spin states of molecules [96,97].

4.2 Experimental setup

Our experimental setup can be categorized into three major parts namely the source, deceleration and detection chamber. An additional test chamber was used in order to optimize the generation of methyl radicals. This chamber was separate from the chamber consisting of Zeeman decelerator and is described after description of the main experimental setup which was used for trapping of methyl radicals.

4.2.1 Source chamber

It consists of a CRUCS valve, a discharge plate and a skimmer. The CRUCS valve is a pulsed valve which can run as fast as 10 Hz and with an opening time as short as 30 μs. It is cooled using liquid nitrogen while a 50 W heater is used to maintain the temperature of the nozzle at a specific value which depends on the pressure of the gas. For methyl radical experiments, typically we use a pressure of around 5-6 bar of methane gas mixed in Krypton which corresponds to a boiling point of 145 K for methane gas. The valve has an orifice diameter of 250 μm and is sealed by a plastic

poppet which is mounted on a spring. The nozzle activation is achieved using a solenoid located inside the nozzle assembly.

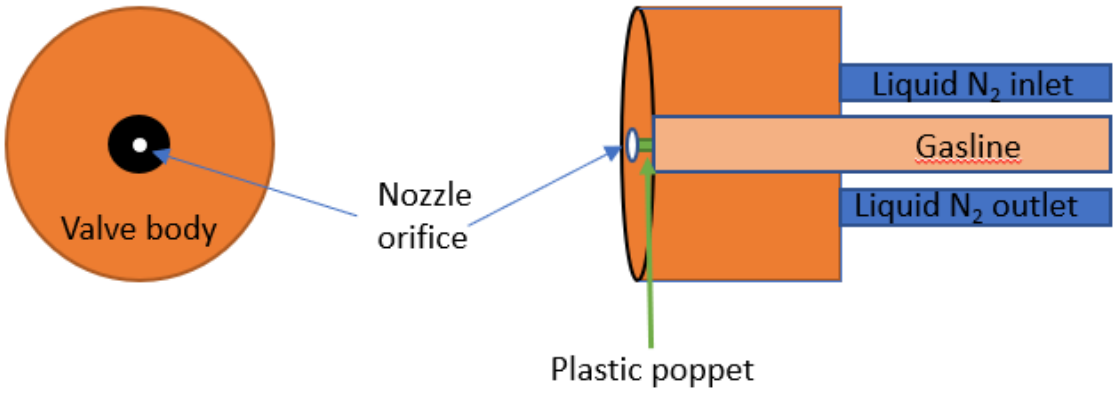

Figure 4-1: The CRUCS nozzle. The nozzle orifice has a diameter of 250 um and is sealed by a plastic poppet. The whole valve body is cooled using liquid nitrogen to reduce the initial beam velocity. The gas line contains the mixture of methane and krypton gas at a pressure of 5 bar.

When current flows through the solenoid and the poppet spring, the magnetic field generated due to solenoid pulls the spring back. As the spring moves back, it allows the gas to come out from the orifice. In our experiments, we use a pressure of around 5 bars in the nozzle. At this pressure, there are no concerns for any leaks in the nozzle. Whenever a leak occurs in the nozzle, it is mostly due to damage to the gasket which is placed between the nozzle orifice and the poppet. This can be easily fixed by replacing the damaged gasket with a new gasket. The skimmer has a diameter of 2 mm. The chamber is pumped by a turbo molecular pump to reduce the pressure below 1×10^{-8} Torr. The discharge plate has a hole in the center with a diameter of 3 mm and a thickness of 0.7 mm. This plate is attached to the nozzle head with a polytetrafluoroethylene (PTFE) spacer for insulation.

4.2.2 Deceleration chamber

The deceleration chamber consists of an array of 85 solenoid coils in order to decelerate methyl radical before they enter the permanent magnet trap located at the end of the 85th coil. The 85 coils are supplied current from driver boards. Each driving board runs 5 coils and, every coil is wired individually to its driving board. To connect each coil which is inside the chamber and its driving board which is outside the chamber, six vacuum feedthroughs are used which can withstand a current of 600 A when the coils are activated. The inner core of each solenoid coil is

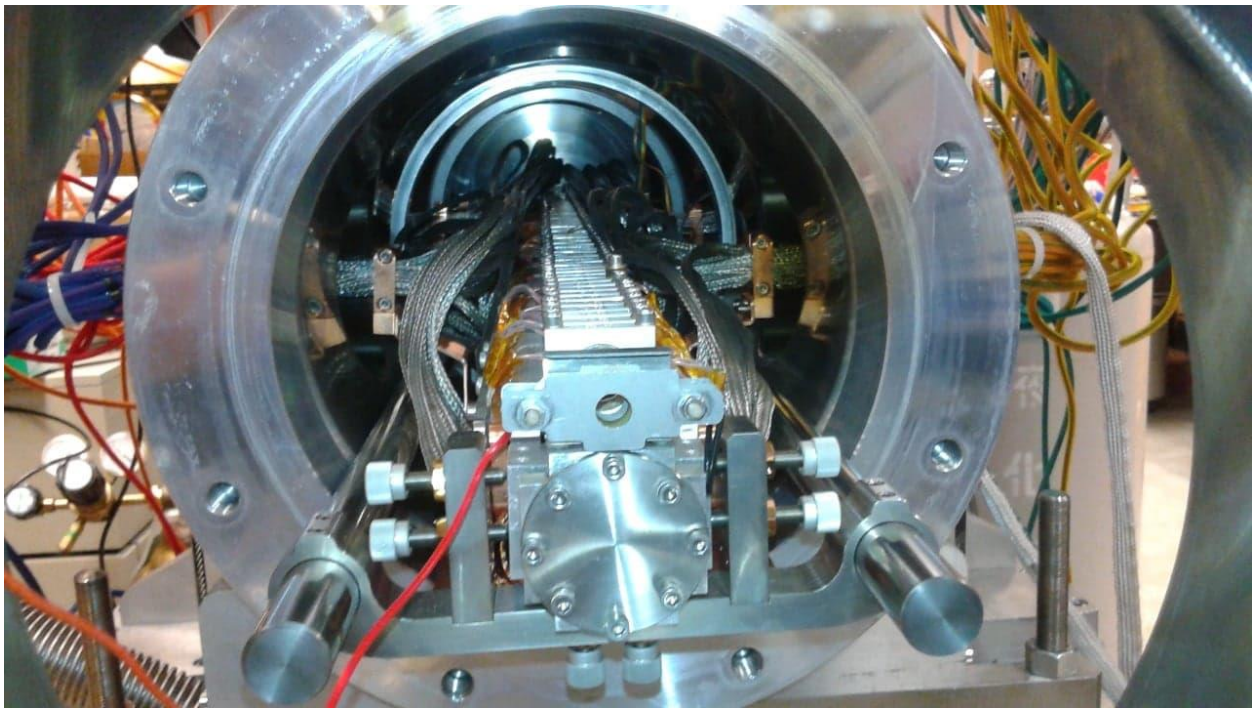

Figure 4-2: Picture of Zeeman decelerator chamber looking from the detection chamber side. The 85 coils are arranged linearly on a cooled copper plate using a closed cycle refrigerator. The current carrying wire for each coil is connected to the driver boards which are outside the chamber through a vacuum feedthrough. A total of six feedthroughs are used for 85 coils.

made up of permendur material which is a cobalt-iron alloy. Permendur has a higher shielding effect in comparison to cast iron which is why the outer core is also made up of permendur. The coil has a hole in the center with a diameter of 4 mm for the transmission of molecules. A kapton

coated copper wire is used as the current carrying conductor around the inner core. The total number of turns around the inner core is 30 laid out on 6 layers of 5 turns each. The diameter of inner and outer core is 10.3 mm and 17.8 mm respectively. At a current of 600 Amperes, a magnetic field of 4.27 Tesla is produced at the center. The rise time for the current inside the coil to reach its maximum value is around 70 us. Therefore, each coil is turned on 80 us before the molecules arrive at the entrance of coil. The fall time for the current in the coil from it maximum value to zero current is around 7.5 us. All the coils including the coils used in the permanent magnet trap are cooled by a close-cycle refrigerator to remove the heat generated when a current of 600 Amperes is running through the coils. The cooling also reduces the resistance of copper wires which increases the current flow through the coils at a given voltage. In order to monitor the temperature inside the decelerator, there are four temperature sensors located on coil numbered 8, 38, 76 and the cold head of the refrigerator. During the normal operation of decelerator which around 0.4 Hz, coil 8, coil 38, coil 76 and the cold head hovers at a temperature of 90 K, 95 K, 110 K and 67 K respectively. The decelerator can be maintained to a specific temperature by using two 50 W heaters installed on the copper base. This avoids the contraction and expansion of decelerator during times when we do not run experiments. The total length of decelerator is around 1 metre. Alignment screws are installed at both ends of decelerator which can be used to align the decelerator to the skimmer. The decelerator is aligned to the skimmer followed by alignment of nozzle to skimmer. The nozzle can be moved from outside the chamber however the decelerator alignment can only be done if the chamber is open. A telescope is used for aligning the decelerator, skimmer and the nozzle. This serves as a good starting position which can be further optimized by moving the nozzle with respect to skimmer by measuring the transmission of a molecular beam of oxygen gas. For this process, no deceleration is needed as a pure oxygen molecular beam is fast

and gives a strong signal which can be obtained easily. Since the alignment of nozzle, skimmer and decelerator is independent of molecule used, we used oxygen gas. Another reason to use oxygen over any other molecule is because oxygen can be ionized at a similar wavelength as methyl radical. This avoids change of dye in the pulsed dye laser.

4.2.3 Detection chamber

In order to trap the decelerated radicals, an anti-Helmholtz–type magnetic trap made of two ring-shaped NdFeB permanent magnets was placed at the end of the decelerator. Each magnet has an outer diameter of 19 mm and an inner diameter of 6.35 mm. Its magnetic field distribution is shown in Fig. 4-3. This trap provides a maximum magnetic field of 0.75 T (longitudinal) and 0.45 T (transverse), which corresponds to a 500 mK (longitudinal) and 300 mK (transverse) trap depth for CH_3. In addition, solenoid coils were placed inside the magnets and used as the last stages of the decelerator. There are 24 turns of Kapton coated copper wires with 2 layers of 12 turns each inside each of the magnet. These magnets are also used as a part of ion optics in order to accelerate the ions towards MCP. The front magnet is supplied a voltage of +1600 V and the rear magnet is kept at +200 V.

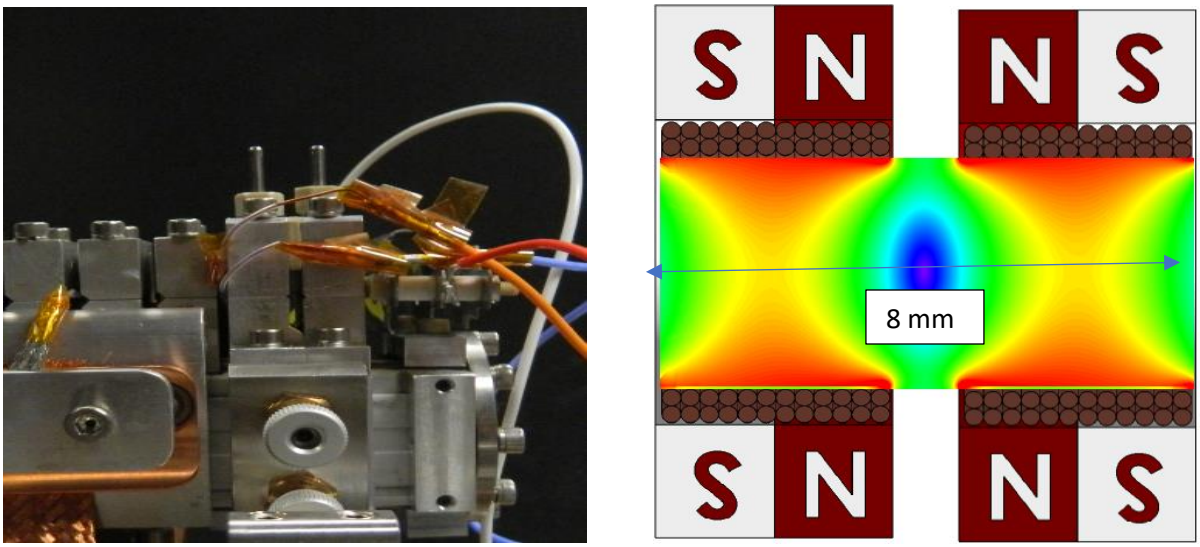

Figure 4-3: Permanent magnet trap. The trap is arranged in an anti-Helmholtz type configuration. The magnetic field is zero in the center. Each magnet has a solenoid coil inside it with a total of 24 turns arranged in 2 layers of 12 turns. The distance between the maxima of magnetic field on either side of trap center is 8 mm.

4.3 Theory

4.3.1 Deceleration

A Zeeman decelerator is made up of solenoid coils. Inside each solenoid coil, the magnetic field distribution in the longitudinal direction which is along the molecular beam axis is shown below in Figure 4-4. Each end on x axis marks the entrance and exit of a coil. The methyl radical enters the coil starting from z=0 position with the center of coil at 6 mm. At the center of the coil, the magnetic field is maximum. So, the differential $\partial B/\partial z$ is zero at the center. Phase angle is commonly used term in deceleration experiments and is denoted by $\emptyset$.

$$\emptyset = \frac{z}{L} \times 180^{\circ}$$

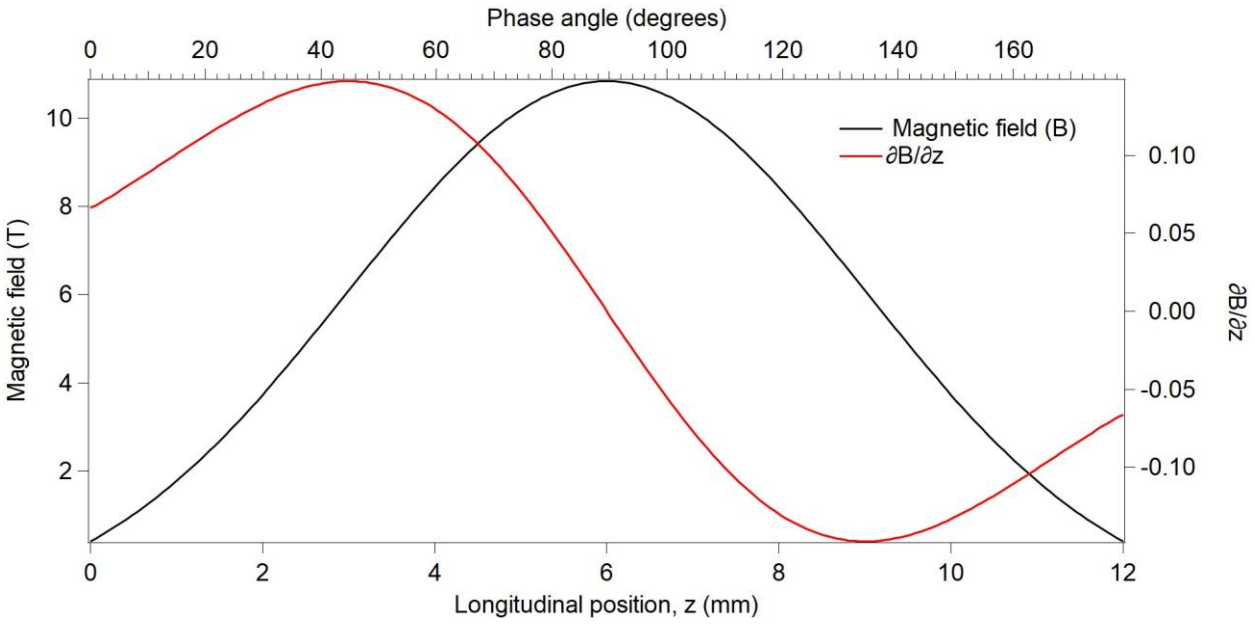

Figure 4-4: : Magnetic field and phase angle inside a coil. 6 mm is the center of the coil at which the phase angle is 90 degrees and the magnetic field is maximum. The red trace shows the derivate of magnetic field with respect to position. The molecule travels from left to right.

So, at z = 0, 6,12 the phase angles are 0, 90, 180 degrees respectively. The potential energy of LFS methyl radicals increases whereas the kinetic energy decreases and becomes maximum at $\emptyset$. Once they cross $\emptyset = 90$, the potential energy starts to decrease again and the kinetic energy increases. In Figure 4-5, the current flowing through a solenoid coil is shown as a function of time. In order to decelerate methyl radicals, the current producing the magnetic field must be switched off before the radicals can cross $\emptyset = 90$, otherwise the radicals will start to accelerate. This is achieved by using insulated gate bipolar transistors (IGBT). The current reaches its peak value is around 70 us and the time taken for the current to drop to zero from its peak value is around 3.5 us. This fast switching is the key to decelerate paramagnetic molecules inside a Zeeman decelerator. The amount of kinetic energy removed from methyl radical will be maximum if the phase angle is 90 degrees. However, due to finite phase space acceptance of a coil, the number of decelerated molecules decreases with increase in phase angle. In general, a synchronous molecule is chosen

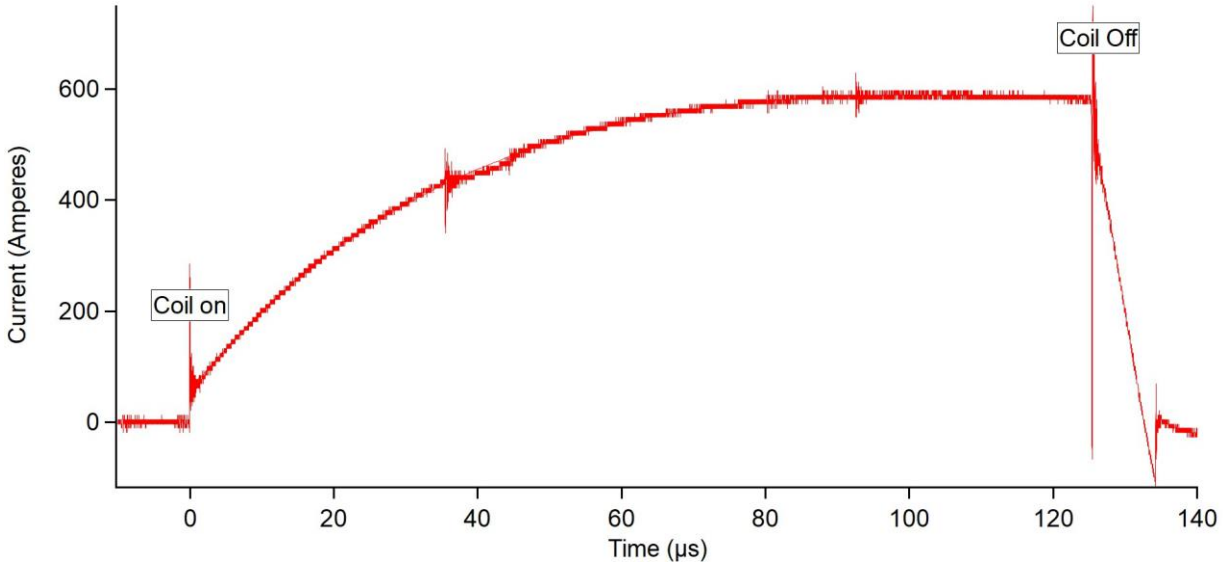

Figure 4-5: Current profile of a solenoid coil used in the Zeeman decelerator. The pulse duration is 125 us when the coil is turned off.

with a specific velocity and the phase angle is determined by the final decelerated velocity of this molecule. In order to choose the velocity of synchronous molecule, a free time of flight is measured by turning the decelerator off. The peak velocity and FWHM of the velocity distribution are used as an input for the simulation. Depending on the final decelerated velocity required, different combination of the phase angle and the velocity of synchronous molecule are used as an input for the simulation which outputs different number of decelerated molecules. The synchronous velocity and the phase angle which outputs the maximum number of decelerated molecules is used in the experiment.

Figure 4-6 shows the schematic of methyl radical deceleration with a Zeeman decelerator. As the radical enters coil 1, the current is activated around 80 us before it reaches the entrance such that the magnetic field produced for deceleration is at its maximum. This also provides a nonzero

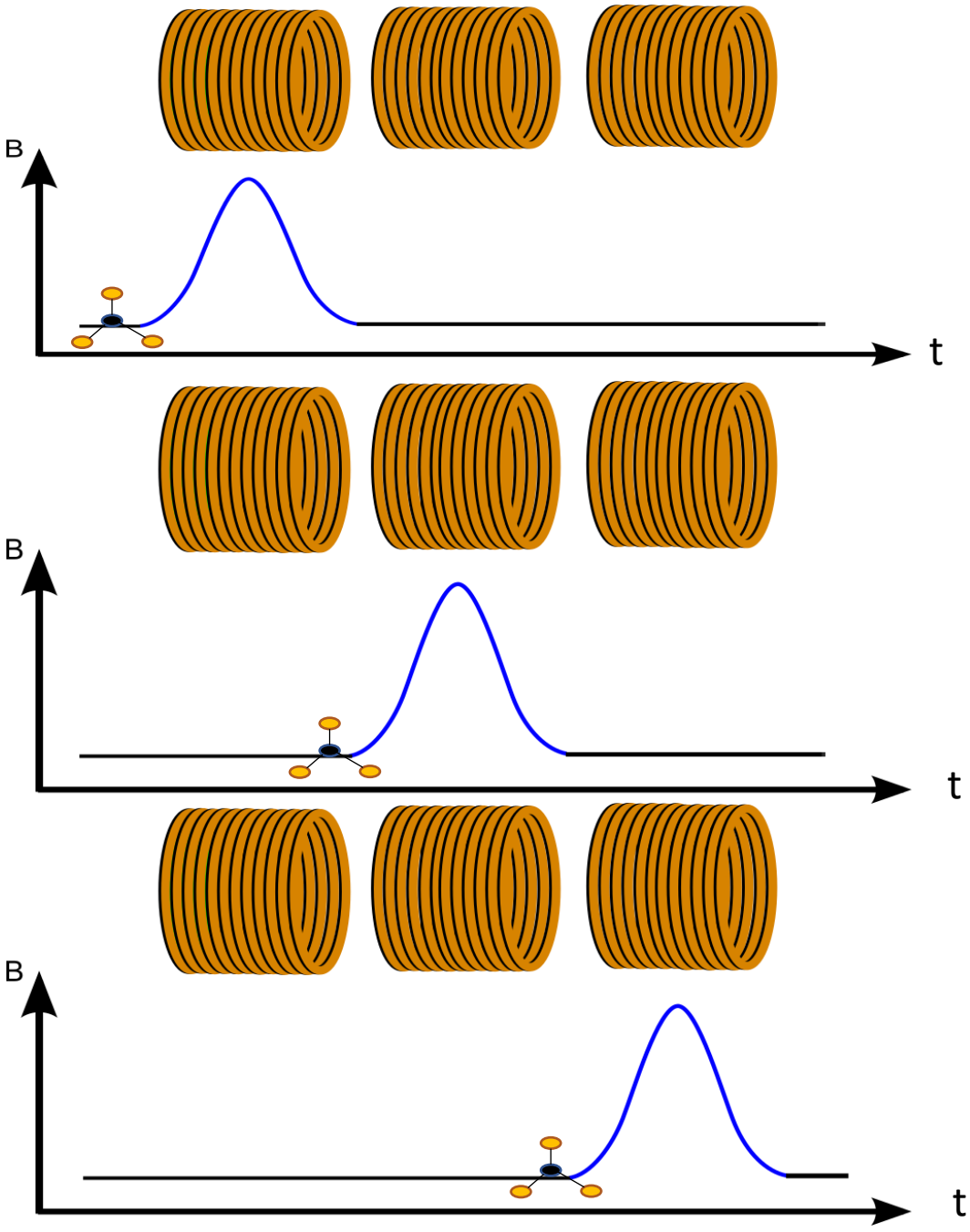

Figure 4-6: Deceleration scheme of methyl radical depicted using three coils. The first coil is turned on while the other two coils are off. After climbing up the potential hill (blue), first coil is turned off such that the methyl radical travels in field free region until it reaches the entrance of second coil where the process is repeated again.

magnetic field such that there is no loss of radicals due to field free region during deceleration. Depending on the phase angle chosen, the switch off time of a coil is determined based on its position inside the coil. After turning coil 1 off, the radical travels towards coil 2 where similar process is repeated. As a result, the radicals get slower at each successive coil. As a result, he duration of current pulses increases at later stages of deceleration as the radicals take more time to traverse the same distance in the coil. For example, in order to reduce the velocity of methyl radical from 320 m/s to 60 m/s, coil 1 and coil 85 runs for a duration of 120 μs and 180 μs respectively.

4.3.2 Trapping

To trap CH_3 radicals, the decelerated packet is slowed further down using the first solenoid coil housed inside the first permanent Ni-coated NdFeB magnet used for the trap. Figure 4-7 shows the phase space plot of the decelerated packet in which the synchronous molecule is travelling with a speed of 60 m/s. This decelerated packet is loaded into the trap using the sequence described below. The current inside the first solenoid coil is switched on when the position of the synchronous molecule is 15 mm away from the trap center. This is done in order to further slow down the radical from 60 m/s to 38 m/s.

Figure 4-9 A shows the magnetic field distribution in the trap region when the current in the front coil is on and the rear coil is off. The x-axis is the direction along the longitudinal direction which is along the beam axis. Zero position on the x axis is the center of the trap and the magnetic field is zero if both the solenoid coils are off. The front trapping coil is switched off when the synchronous molecule is at 6 mm from the trap center (-6 mm on x axis). At this time, the rear coil is turned on and the magnetic field distribution in the trap region can be seen in Figure 4-9 B. The

rear coil completely stops the molecule after which both the solenoid coils are turned off (Figure 4-9 C). After this step, the radicals with velocity greater than 18 m/s escape the trap whereas the rest of radicals are confined inside the trap due to the magnetic field of permanent magnets. The magnetic field strength of the permanent magnets is 0.75 T (longitudinal) and 0.45 T (transverse) which corresponds to 500 mK and 300 mK trap depths for CH_3 radical respectively. This is shown in Figure 4-8. In terms of velocity of the radical, 500 mK and 300 mK corresponds to 23 m/s and 18 m/s.

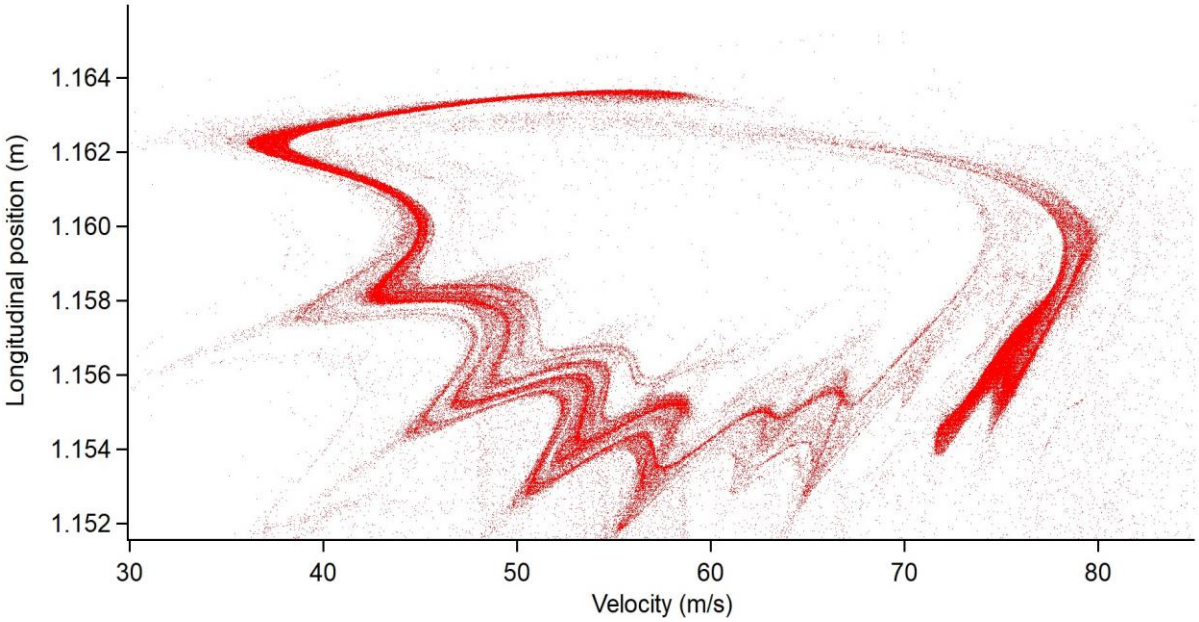

Figure 4-7: Phase space plot of the decelerated packet before entering the trap region. The synchronous molecule speed is slowed down from 320 m/s to 60 m/s. The y axis denotes the position along the molecular beam axis and the trap center is located at 1.177 m.

is turned on and the magnetic field distribution in the trap region can be seen in Figure 4-9 B. The rear coil completely stops the molecule after which both the solenoid coils are turned off (Figure 4-9 C). After this step, the radicals with velocity greater than 18 m/s escape the trap whereas the

rest of radicals are confined inside the trap due to the magnetic field of permanent magnets. The magnetic field strength of the permanent magnets is 0.75 T (longitudinal) and 0.45 T (transverse) which corresponds to 500 mK and 300 mK trap depths for CH_3 radical respectively. This is shown in Figure 4-8. In terms of velocity of the radical, 500 mK and 300 mK corresponds to 23 m/s and 18 m/s.

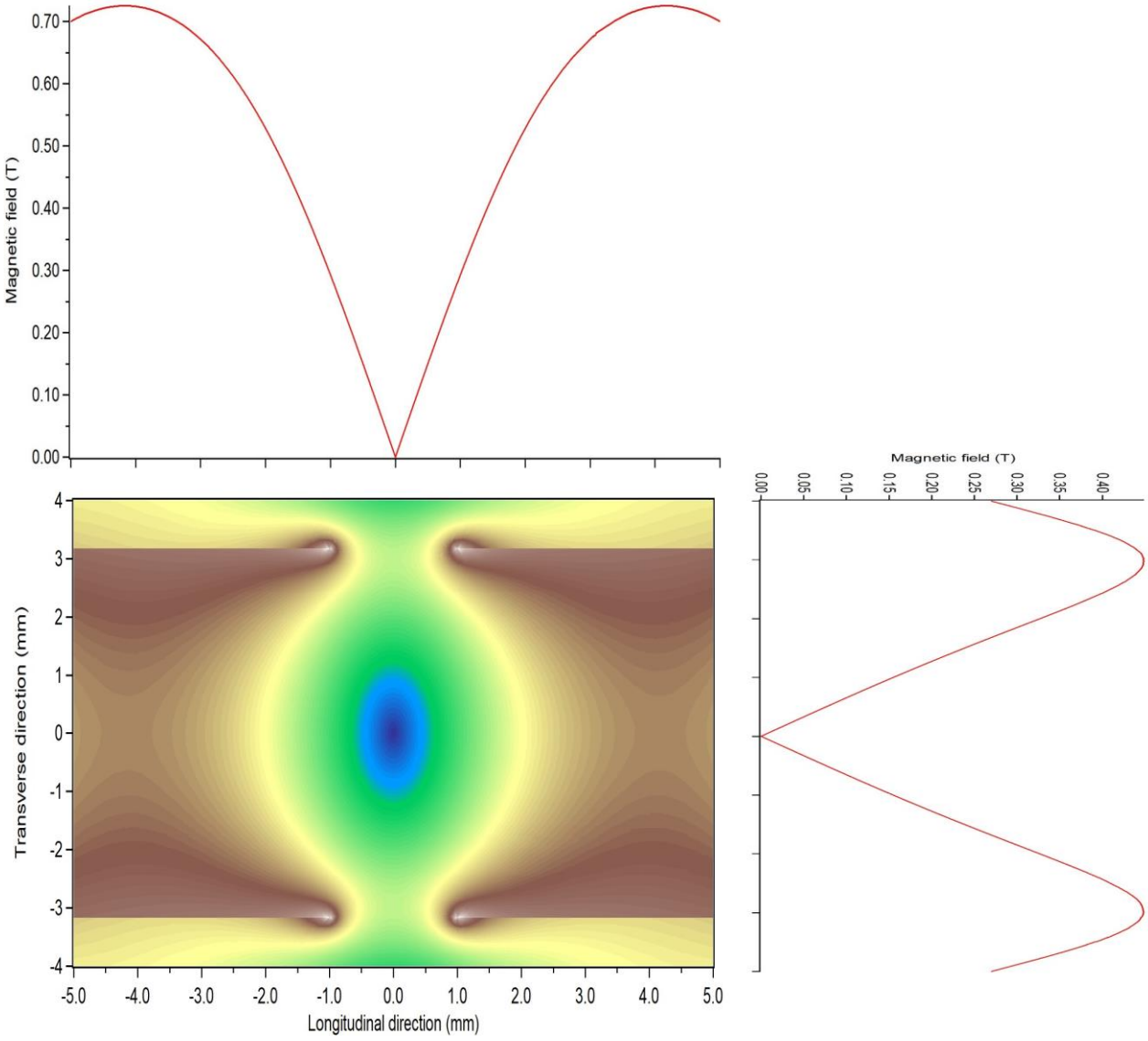

Figure 4-8: Magnetic field distribution of our anti-Helmholtz configuration trap

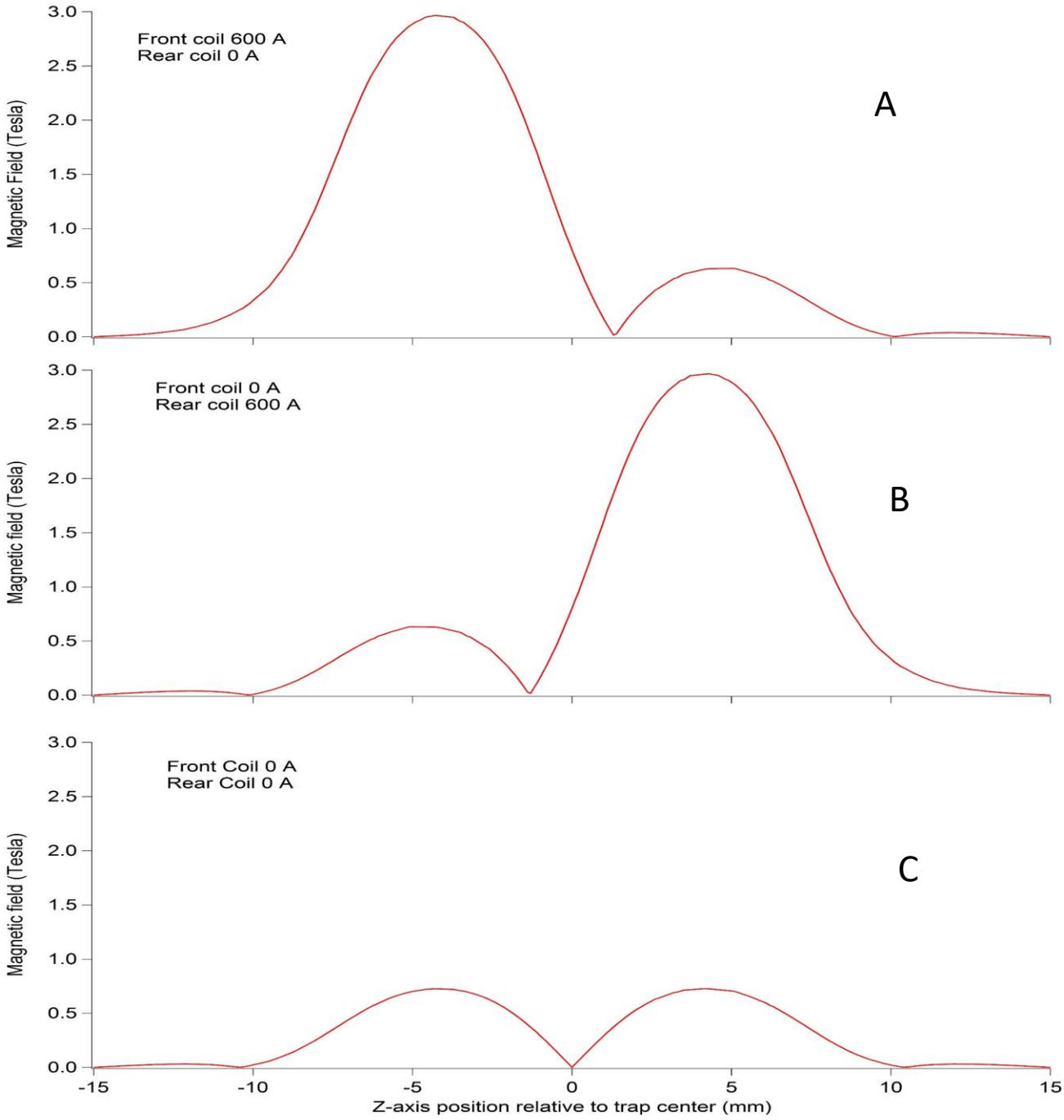

Figure 4-9: Trapping scheme of methyl radicals using the solenoid coils inside the permanent magnets. The position on the x axis denotes the distance from the trap center. Negative values on x axis are towards the nozzle and positive values are towards the detector side. The radical enters the trap region from the left in the figure above and is slowed down in figure A, from 60 m/s to 38 m/s. In Figure B it is reflected towards the center of the trap such that velocity is smaller than the trap depth as shown in Figure C. Radicals with speed less than the trap depth are confined in the trap due to the magnetic field of permanent magnets,

4.3.3 Elastic collision cross section of trapped radicals with helium and argon

In order to calculate the elastic cross section between trapped methyl radical and different background gases, a leak valve was installed in the detection chamber. Using the leak valve, helium and argon gases at a known background pressure were leaked in the detection chamber. The background gas density is known using an ionization gauge which is cross-calibrated with a residual gas analyzer. The background gas has a Maxwell Boltzmann distribution at 298 K. The energy transfer between the background gas and the trapped radicals, is due to elastic and inelastic collisions. In elastic collisions, there is no change in the quantum state of the colliding particles i.e. only momentum transfer takes place during these collisions. Whereas in inelastic collisions, internal state of colliding partners changes. The loss of trapped radicals can occur due to both types of collisions. However, only some of the elastic collisions impart enough energy to radicals such that they can overcome the trapping potential and hence escape the trap. Larger the density of the background gas, more will be the number of such collisions. Therefore, the loss rate of trapped radicals in presence of a background gas is also proportional to its density. The loss rate of methyl radicals from the trap follows a first order differential equation given by:

$$\frac{d[CH_3]}{dt} = -\tau[CH_3] \tag{4.1}$$

Where $\tau = \langle v\sigma \rangle[n]$ is a pseudo-first order rate coefficient that depends on the background gas density [n], and the velocity-weighted cross section for trap-loss collisions. The trap loss is measured over time in order to measure τ, which can then be used to measure the elastic cross-section of trapped radicals with the known background gas.

Theoretical calculations are also made to compare with the experimental measured values for the collision cross section of trapped radicals with helium and argon. In our theoretical calculations, we use an interaction potential comprising of only the C_6 coefficient, therefore only a long-range isotropic interaction is considered. The interaction potential between CH_3 and a background gas n is given by,

$$V = -\frac{3}{2}\frac{I_n I_{CH_3}}{I_n + I_{CH_3}}\frac{\alpha_n \alpha_{CH_3}}{r^6} \tag{4.2}$$

Here, I_{CH3} and I_n are the first ionization energy for CH_3 and background gas n respectively. The polarizability is denoted by α and r is the distance between the two species. The collision energy between two particles with reduced mass μ and relative momentum k is given by E

$$E = \frac{h^2 k^2}{2\mu} \tag{4.3}$$

The scattering amplitude, f can be represented as a sum over the partial waves.

$$f = \sum_{l=0}^{\infty}(2l+1)\, f_l P_l(cos\theta) \tag{4.4}$$

ere f_l is the partial scattering amplitude and P_l are the Legendre polynomials. The differential cross section (DCS) is

$$\frac{d\sigma}{d\Omega} = |f(\theta|^2 = \frac{1}{k^2}\left|\sum_{l=0}^{\infty}(2l+1)\, e^{i\delta_l}\sin(\delta_l) P_l(cos\theta)\right|^2 \tag{4.5}$$

, δ_l is the phase shift of the lth partial wave. This phase shift is the difference between phase of radial wave functions in the presence and absence of the scattering potential.

The energy transferred during an elastic collision between a trapped CH_3 whose kinetic energy can be neglected and particle of mass m with a relative velocity v and a scattering angle of θ can be written as:

$$E = \frac{\mu^2}{m_2}|v_r^2|(1 - cos\theta) \quad (4.6)$$

minimum scattering angle θ_{min} is defined as the scattering angle which ejects a trapped CH_3 particle and can be written as

$$\theta_{min} = \cos^{-1}\{1 - \frac{m_2 U_{trap}}{\mu^2|v_r|^2}\}\#(4.7)$$

The total cross section is then computed by integrating the DCS from a minimum scattering θ_{min} to Π. The elastic cross section for Helium and Argon obtained by integration of DCS is shown in Figure 4-15.

$$\sigma = \frac{4\pi}{k^2}\sum_{l=0}^{\infty}(2l+1)sin^2\delta_l \quad (4.8)$$

4.4 Results and discussion

4.4.1 Deceleration and trapping

Figure 4-10 shows a free TOF spectrum in which the x axis is converted to velocity of the molecular beam. Figure 4-11 shows the decelerated plot for methyl radicals starting from an initial speed of 320 m/s. The pressure behind the nozzle in this experiment was 5 bar with the nozzle set to a temperature of 152 K as the boiling point of this mixture at this pressure was 145K. Using different phase angles, we have decelerated the radicals to any desired speed. In this plot, the radicals were decelerated from 320 m/s to 245 m/s, 200 m/s, 150 m/s, 104 m/s and 62 m/s at phase angles of 10, 27 and 29 degrees respectively. We can see from the plot that as the deceleration increases the intensity of the decelerated peak decreases.

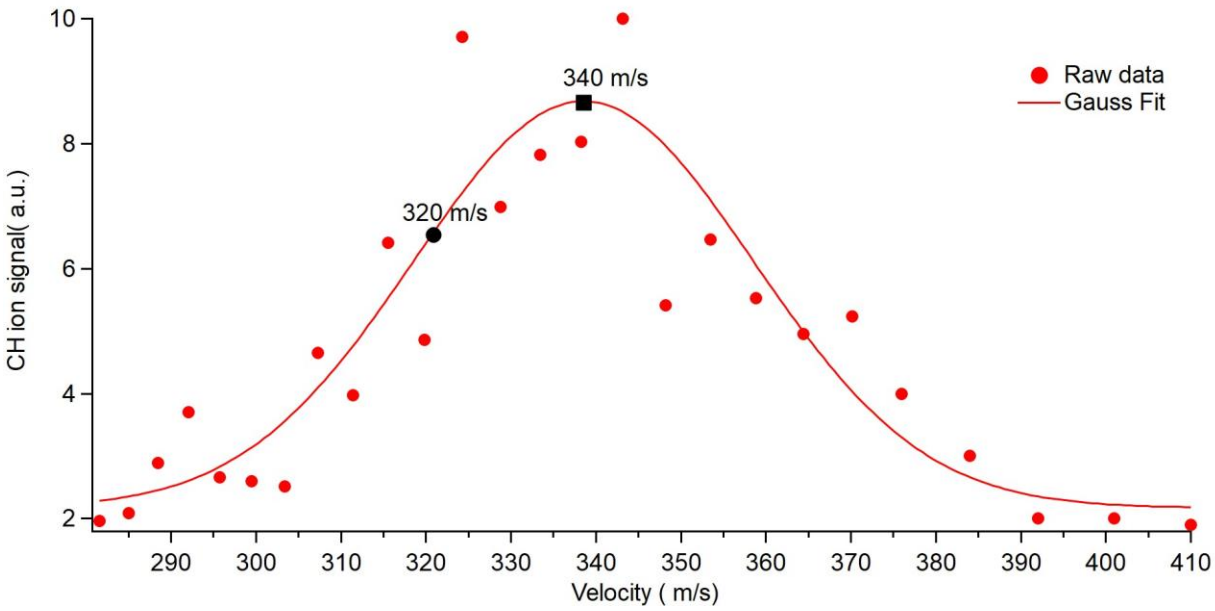

Figure 4-10: Free time spectrum for a mixture of CH_4 and krypton gas. The concentration of CH4 was 15% and a discharge voltage of 1.1 kV was applied

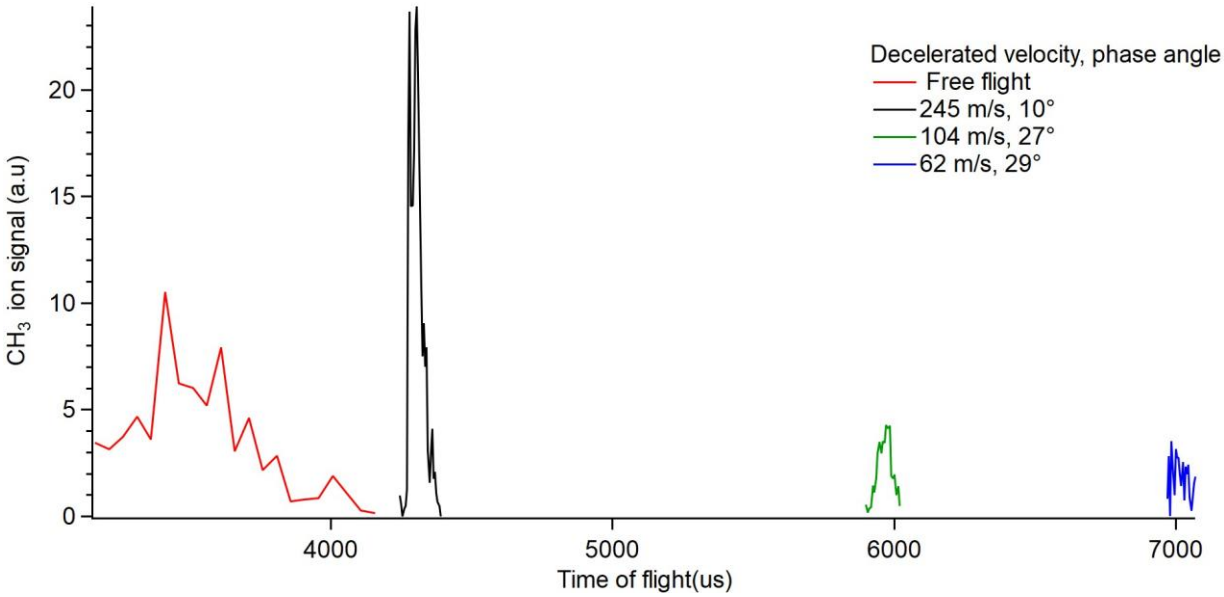

Figure 4-11: Free time of flight and decelerated time of flight traces of methyl radical molecular beam

Figure 4-12 shows a time-of-flight (TOF) feature of the REMPI signal of CH_3 at the center of the trap. In order to eliminate background signals and other noise sources effectively, experiments with the Zeeman decelerator on and off (i.e., no deceleration) were executed alternatively in each sequence, and the on and off signal intensities of each set were subtracted before taking their averages. The zero-intensity line shown in Fig. 4-12 (the dotted line) corresponds to the case with no radicals in the trap and is the measured baseline, while positive values indicate that some radicals decelerated by the decelerator were detected inside the trap. As shown in Fig. 4-12, a strong REMPI signal was observed at TOF 7.0 ms –7.5 ms, which corresponds to the first entry of a dense decelerated radical packet into the trap region. After that, signals were detected continuously, which confirms that the decelerated CH_3 radicals were successfully confined in the

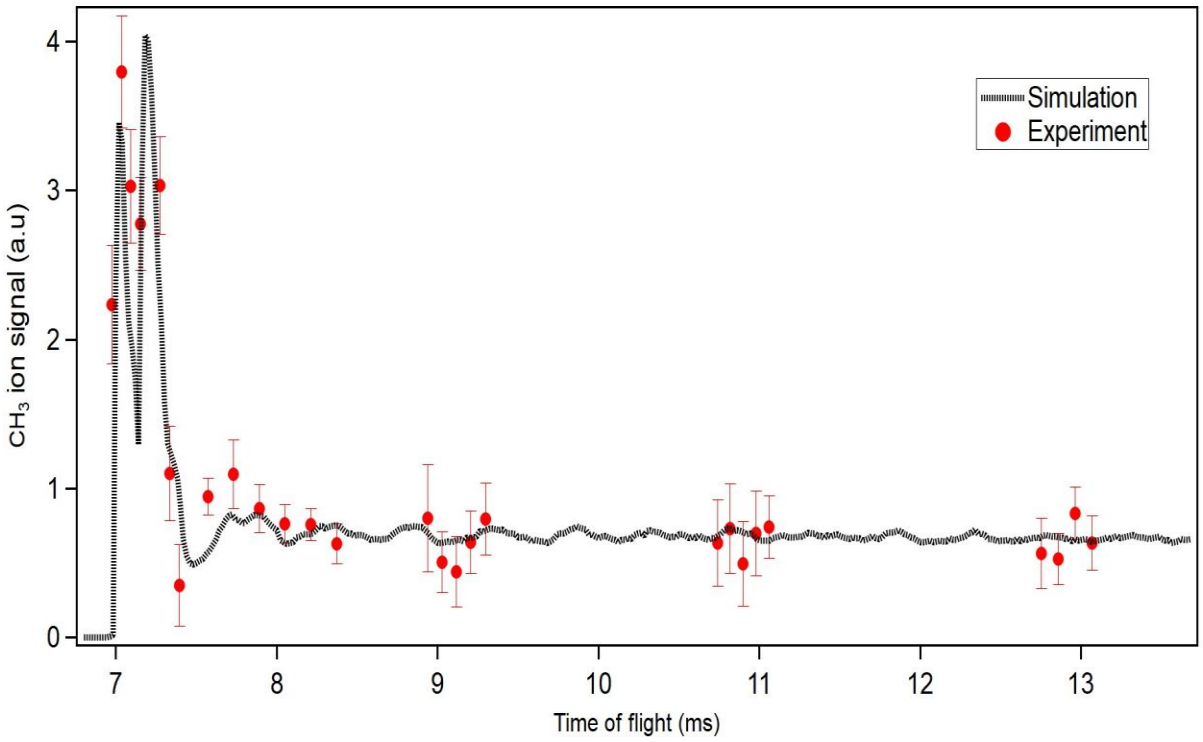

Figure 4-12: Time-of-flight distribution of the decelerated packet. The peak around 7 ms corresponds to entry of the decelerated packet after it has been slowed down from 60 m/s to 38 m/s by the front coil. After this time, the red dots show the oscillation of radicals inside the trap. The dotted trace is produced from simulations.

trap. The observed TOF feature was well reproduced by trajectory simulations of the radicals inside the trap, which is shown as a dotted trace in Fig. 4-12. The trapped signal showed an exponential decay overtime for 1 s. The two traces shown in Fig. 4-13, which were recorded every 100 ms with a 10 Hz pulsed laser, correspond to the cases where the background pressure was 3.8 × 10^{-9} Torr (filled circle) and 6.3 × 10^{-9} Torr (filled triangle). The fitted 1/e lifetime, τ, of the trapped radicals was τ =1.03 ± 0.19 s and 0.70 ± 0.16 s, respectively. The shorter trap time at higher background pressure indicates that the trap lifetime of CH_3 is limited by collisions with residual background gases. Under such conditions, the number of trapped radicals, N_{CH3}, may obey a first order differential equation $dN_{CH3}/dt=-(1/\tau)\ N_{CH3}$, where the lifetime, τ, is inversely

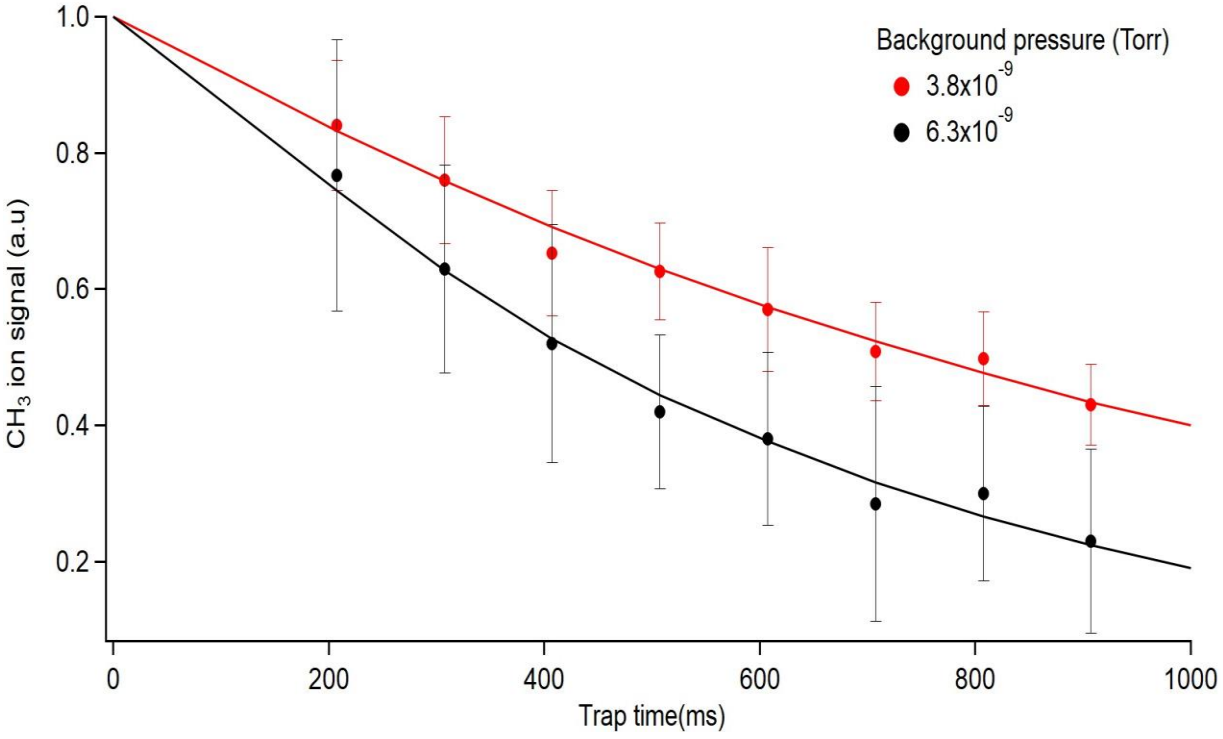

Figure 4-13: Exponential decay of trapped signal at two different background pressure

proportional to the average of the product of the cross section, σ, velocity, v, and the density, n, of background gas particles. The measurement of background gases by a residual gas analyzer revealed that the major component of the background gas in our vacuum chamber was H_2 (or H) with some N_2 as a minor component (less than 1/3 of H_2). By assuming that the trap loss is entirely induced by H_2 molecules (v = 1950 ms−1 mean velocity at 300 K), the average of the cross section for the trap loss caused by H_2 molecules is estimated to be $\langle\sigma\rangle_{H2} \sim 380$ Å^2 at the present trap depth of 300–500 mK. The cross section obtained here is an effective cross-section that depends on the trap depth and the velocity of the collision partners.

4.4.2 Collision experiments with other background gases:

In order to calculate the elastic cross section between trapped methyl radical and different background gases, a leak valve was installed in the detection chamber. Using the leak valve, helium and argon gases at a known background pressure were leaked in the detection chamber. The background gas density is known using an ionization gauge which is cross-calibrated with a residual gas analyzer. The background gas has a Maxwell Boltzmann distribution at 298 K.

Figure 4-14 shows the loss of methyl radicals from the trap over time in presence of helium and argon gases. The red trace was measured without any leaked gas and the background pressure was 3.8×10^{-9} Torr. The τ for red trace was found to be 1.03 ± 0.068 s. After this measurement, helium gas was introduced such that the pressure in the detection chamber was 1.8×10^{-7} Torr. The τ for this measurement was found to be 0.33 ± 0.006 s. Similarly, argon was introduced inside the detection chamber at a pressure of 2.9×10^{-8} Torr and the lifetime, τ was found to be 0.6 ± 0.01 s. Using the lifetime measurement of trapped radicals in the presence of helium and argon together

with the lifetime measurement when no gas was leaked, we found the cross section of trapped radicals with helium and argon to be 31.4 and 275.2 $Å^2$ respectively.

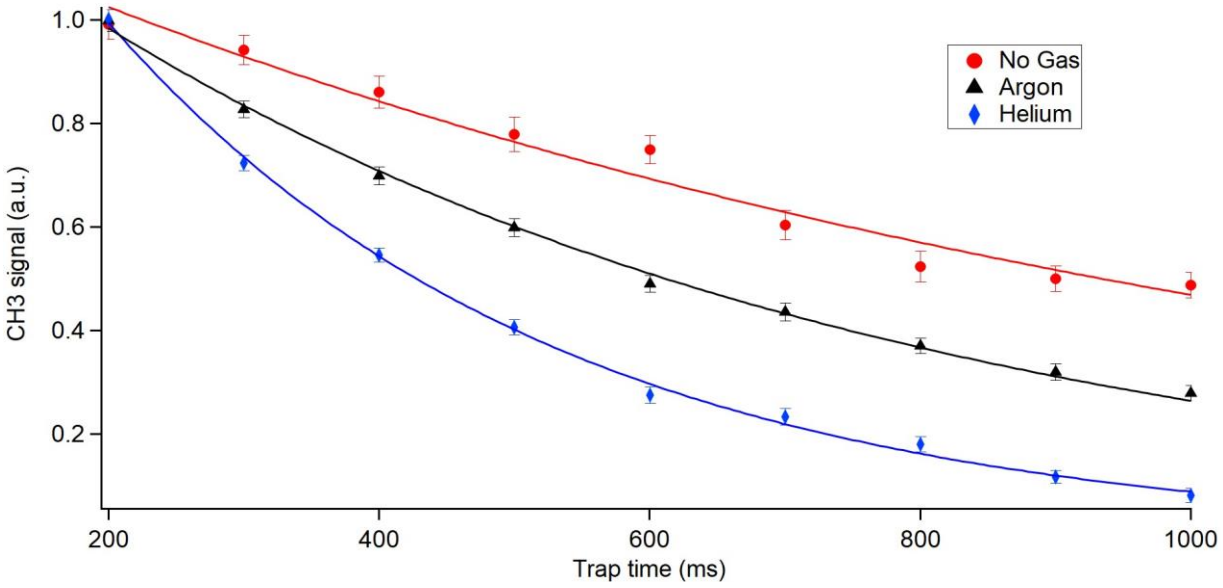

Figure 4-14: Trap lifetime curves in presence of different background gases

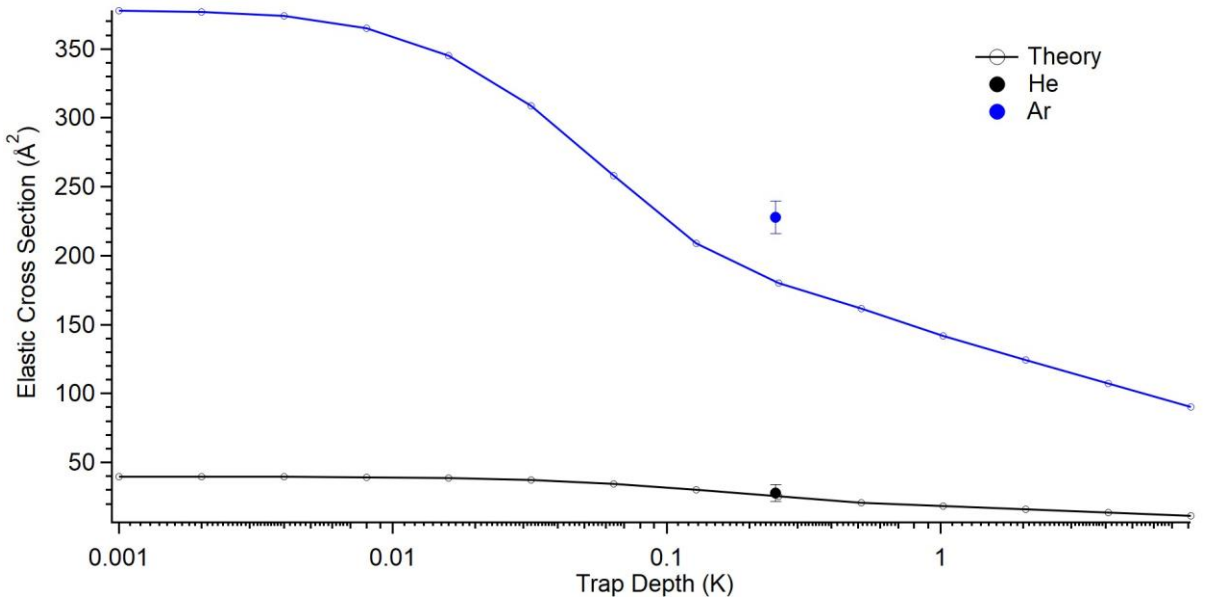

Figure 4-15 : Cross section of different background gases as a function of trap depth.

The theoretical calculations accuracy can be improved by using a more accurate potential energy surface between the trapped radicals and the specific background gas. The role of anisotropy due to planar nature of methyl radical and spherically symmetric noble gas atom can be revealed using an accurate potential. The overestimation of elastic cross section in our experiment with the current calculations show that the loss mechanism of the trap is not limited to elastic collisions with background gas. Since the experimental measured lifetime of the trap consists of elastic, inelastic collisions with background as well as intermolecular collisions within the trap. Since our trap is made up of permanent magnets, measuring cross section at a different trap depth is not straight forward. Measurement of trap lifetime at different depth can reveal the dominant loss mechanism and their time scales. In a static trap it is not possible to distinguish elastic and inelastic collisions with the trap as well as trap loss due to background gas collisions. One possibility to carry out this measurement is to cool the trapped radicals further. This cooling can be achieved using by applying MW radiation in the trap region to eject fast moving radicals allowing the trap temperature to reduce and thus increasing the lifetime of trap. Since the trap temperature decreases, therefore the lifetime of trap should be limited by inelastic collisions with the background. Another possibility is to use a superconducting DC trap such that the trap depth can be varied by changing the DC current [98]. A varying trap depth can also be used for evaporative cooling of the trapped ensemble in order to reach ultra cold regime and quantum degeneracy.

The number of trapped radicals and its density can be estimated from the efficiency of the 2+1 REMPI process with the help of simulations. This is described in more details in the appendix section. The 2+1 REMPI process of CH_3 is less efficient than other molecules due to predissociation at the intermediate 4p Rydberg state. Indeed, the REMPI spectrum shown in Fig. 3-4 has a linewidth of 4.5 cm^{-1} in the Q branch, which must be limited by the predissociation

lifetime. A predissociation rate of 8.3 $\times 10^{11}$ s^{-1} estimated from the linewidth is faster than the ionization rate of 7.0 $\times$ 10^{10} s^{-1}, assuming a standard ionization cross section of $\sigma^{(i)}$= 1.0 $\times$ 10^{-17} cm^2 and a photon flux of F = 7.0 $\times$ 10^{27} cm^{-2} s^{-1} of our pulse. By using a steady state approximation [99,100] with a two-photon excitation cross section of 50 GM (5 $\times$ 10−49 cm^4 s) and a 10% quantum efficiency for the MCP detector to detect positive ions, signal intensities of the ions are predicted to be 0.0022 N, where N is the number of radicals in the ground state. This estimation indicates that 450 radicals are necessary in the detection volume (a cylinder of 40 μm radius and 600 μm length) to obtain one signal count at the MCP. Furthermore, our simulation predicts that about 0.8% of the trapped radicals reside inside the detection volume (see Appendix). Therefore, the total number of trapped radicals is estimated to be 55 000, which is equivalent to a density of 5.0 $\times 10^7$ cm^{-3} in the effective trap volume (a cylinder of 300 μm radius and 4 mm length). The above estimation is a lower bound for the trapped radicals. The two-photon cross section of 50 GM is a good approximation for molecules with a large two-photon cross-section [101] and therefore it might be overestimated for CH_3.

It is noted that the peak density of the trapped OH radicals in Ref. [91] was determined to be 5 $\times$ 10^{10} cm^{-3}, in which the production rate of the radicals as well as the efficiency of the deceleration are roughly similar to our experiments. Our simulation indicates that the velocity deviation of CH_3 in the present trap is about ±10 ms^{-1}, corresponding to a translational temperature of 200 mK (FWHM) in the trap.

4.5 Conclusion and future work

One immediate application of the trapped cold radicals is precision spectroscopy for the determination of molecular parameters of the radicals precisely by resolving hyperfine structures

in infrared transitions. Another application is the observation of cold reactive collisions. The thermal de Broglie wavelength of CH_3 at this temperature is 1.0 nm, which is already a few times larger than the classical molecular size of CH_3 (0.4 nm). A deviation in the collisional behavior from high-temperature collisions might be detected with this fundamental intermediate in hydrocarbon chemistry, which will shed light on reactions at low temperature environments such as planetary atmospheres and the interstellar medium.

5 A superconducting Fabry Perot cavity for trapping polyatomic polar molecules

5.1 Introduction

Manipulation of molecules by optical dipole force is one of the key techniques that is required for a precise control of molecular motion in any quantum states. MW radiation that are close to the resonance frequency of a polar molecule, can be used to manipulate any quantum state by choosing an appropriate detuning frequency. This force arises due to the AC Stark effect in polar molecules. In 2004, proposal by DeMille et al., to trap polar molecules inside a cavity was based on the AC stark effect [102]. In 2005, Enomoto et al. had proposed a deceleration of polar molecules by using a time-varying MW standing waves in a Fabry-Perot type cavity [103]. Merz et al. demonstrated deceleration of NH_3 molecules from 20 m/s to 16 m/s using the $TE_{1,1,12}$ mode inside a closed cylindrical cavity [104]. A stark decelerator was used to pre-slow the NH_3 molecules to 20 m/s before they entered the cylindrical cavity. This cavity was made up of copper and cooled to 77 K providing a quality factor of 9100.

In 2013, a MW lens effect for the rotational ground state of CH_3CN by combining a slow molecular beam generated by a pulsed counter rotating nozzle and MW standing waves in a cylindrical waveguide cavity was observed by Steffan et al. [105]. The MW AC dipole force due to the MW field nearly resonant to the $|J,K\rangle = |1,0\rangle \leftarrow |0,0\rangle$ transition was strong enough to change the momentum of the CH_3CN molecules. Instead of a Stark decelerator, a counter rotating nozzle which has been discussed in chapter 4 of this thesis was used to pre-decelerate molecules in order to manipulate the J=0 state of a polar molecule. So far, trapping of any polar molecules using MW inside a cavity has not been reported. However, a MW trap was reported using Cesium atoms with a trap lifetime of 1 second [106]. A Fabry Perot cavity aimed for co-trapping of CaF and Lithium

using MWs has been constructed by the group at Imperial College, London [107]. The resonator mode used in these experiments is $TEM_{0,0,3}$ mode at a frequency of 14.5 GHz. The cavity is made up of oxygen-free copper with a quality factor of 50,000 at a temperature of 77 K. In this chapter, a characterization of a similar cavity is discussed. The first step towards trapping of NH_3 molecules using a superconducting Fabry Perot cavity by directly measuring the AC stark effect in NH_3 is presented.

5.2 Experimental setup

Figure 5-1 shows the experimental setup used to measure the AC stark shift of NH_3. It consists of two differentially pumped chambers separated by a skimmer with a diameter of 2 mm. The source chamber houses a CRUCS valve that generates a supersonic beam of ammonia molecules seeded in Argon gas with a mixing ration of 5% at a pressure of 3 bar at room temperature. After the skimmer, which is placed at 10 cms downstream of the nozzle, the molecular beam enters the MW cavity through a hole drilled with a diameter of 5 mm and a length of 6 mm in the center of the cavity mirror at distance of 45 cms. The two mirrors of the cavity are made from copper whose inner surfaces are electrochemically plated with an alloy of lead and tin, which is a superconducting material with a critical temperature, Tc=7-8 K. The two mirrors are cooled by a pulsed tube refrigerator to a temperature of 3 K. The whole cavity and the cold head of the refrigerator is attached to the detection chamber using a flexible bellow which is used for aligning the transmission holes in the cavity with the nozzle and the skimmer. Each mirror has a radius of curvature, R=80 mm and diameter, D=90 mm. The distance between the mirror is around 60 mm which can be varied by 5 mm to shift the frequency of the desired resonator mode. In addition to

the center holes, one of the mirrors has a coupling hole with a diameter of 3 mm for the introduction of MWs inside the cavity.

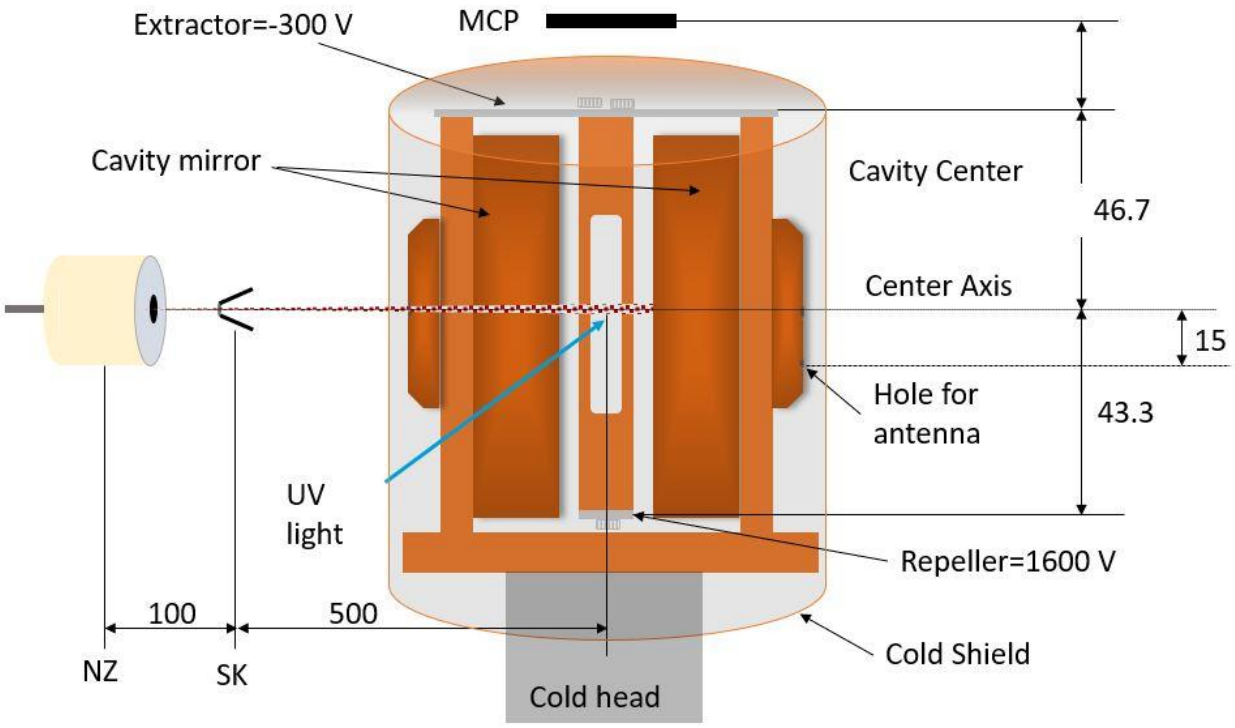

Figure 5-1: Experimental schematic for measurement of AC stark shift in ammonia consisting of a pulsed nozzle (NZ), a skimmer (SK), MW resonator, ion-optics and MCP for detection of ionized ammonia molecules by laser radiation.

The detection chamber consists of the superconducting Fabry Perot cavity, a micro-channel plate (MCP) detector and a coupling antenna to input MW radiation in the cavity. The ionized molecules are directed towards the MCP plate using two metallic plates (repeller and extractor) which are 90 mm apart. The two plates are attached to a detachable frame which is insulated from the cavity using plastic spacers. The design of the repeller and extractor plates was determined using SIMION program. The particle trajectories shown in Figure 5-2 were simulated using SIMION to find the appropriate dimensions of the plates. The repeller and the extractor plates are supplied a DC

voltage of 700 V and -400 V, respectively to guide the ions towards MCP. A 10 Hz Nd-YAG laser at 532 nm is used to pump a dye laser (Narrow scan) to generate UV light that is focused using a 1000 mm lens onto the molecular beam. The ionized molecules arrive at the MCP to generate the signal which was further amplified using a RF mini circuits amplifier.

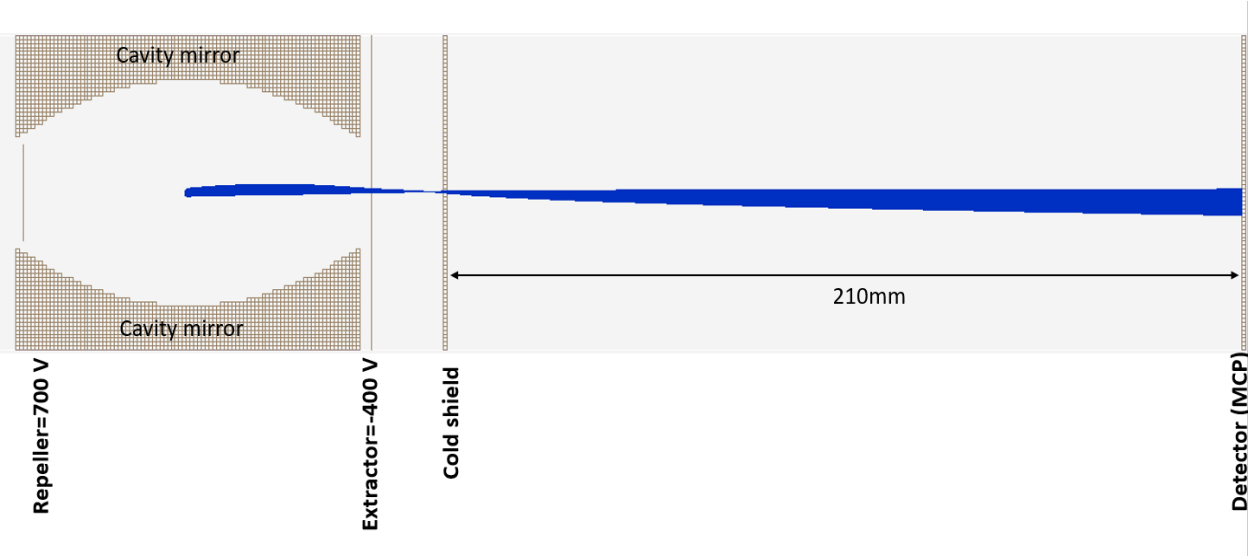

Figure 5-2: Trajectories of particles ionized inside the cavity (blue traces).

The schematic experimental setup used to characterize the cavity is shown in Figure 5-3. The MW signal is generated by a synthesizer (Anritsu MG3693C) and amplified by a K-band amplifier (MKU 2410 A) to 10 W. The coupling antenna is developed from a semi-rigid coaxial cable and inserted into the cavity through a coupling hole in the rear mirror. The antenna is made up of cupro-nickel and located at the tip of the semi-rigid cable. The semi-rigid cable is anchored to the cold shield in order to reduce the temperature of the antenna and maximize the quality factor. The coupling antenna is also used for measuring the reflected signal from the cavity to determine the coupling strength and the resonance frequency of the cavity.

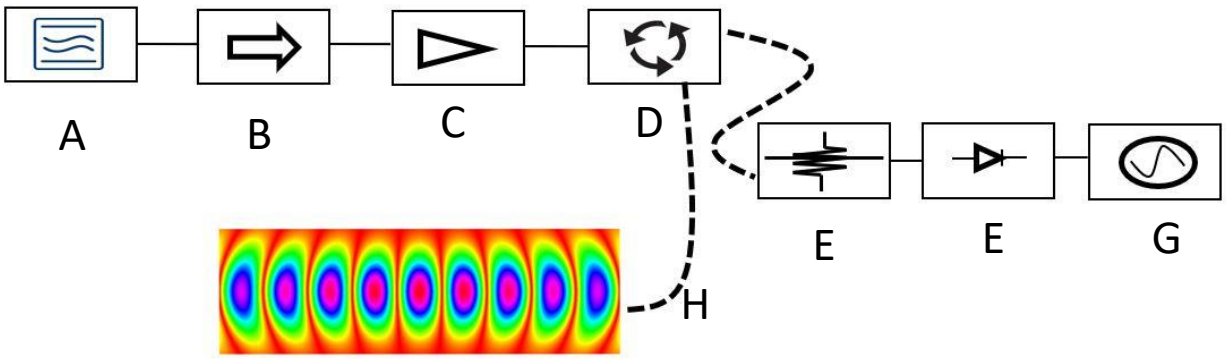

Figure 5-3: Schematic overview of the MW electronics: (a) signal generator (Anritsu MG3693C) , (b) Isolator, (c) power amplifier MKU{2410 A (30 dB gain, maximum output power 40 dBm, Kuhne elektronic), (d) circulator SMC1826 (18-26 GHz, Sierra MW), (e) adjustable attenuator AF868-10 (14-26 GHz, Advanced Technical Materials), F) Detector diode 8437C (0.01-26.5 GHz, Agilent),(g) oscilloscope, (h) coaxial SME cable

5.3 Cavity characterization

The two mirrors in our cavity have same radius of curvature i.e. $R_1=R_2=R=80$ mm. Here R_1, R2 are the radii of curvature of the two mirrors. The field distribution, $A_{m,n}$ of stationary fields inside an open resonator which are called as modes are given by Hermite-Gaussian modes [85].

$$A_{mn}(x,y,z) = C^* H_m(x^*) H_n(y^*) e^{\frac{-r^2}{w^2}} e^{-i\phi(z,r,R)} \tag{5.1}$$

In the above equation, m and n denotes the number of nodes in the x and y direction, respectively. C* is a normalization factor, H_m and H_n are the Hermite polynomials of m^{th} and n^{th} order respectively. The phase factor denoted by ϕ, accounts for the phase change after reflection from cavity mirrors. The modes that have m = n = 0 are called as axial modes or fundamental modes whereas modes with m, n > 0 are called as transverse modes. Each mode is denoted by $TEM_{m,n,p}$ where p is the axial mode number.

The resonant frequency of any $TEM_{m,n,p}$ modes, ν_c in a Fabry Perot cavity whose mirrors are separated by a distance L, is given by [85]

$$\nu_c = \frac{c}{2L}\left(p + \frac{(m+n+1)}{\pi} cos^{-1}\left(1 - \frac{L}{R}\right)\right) \tag{5.2}$$

Figure 5-4 shows the frequency of different modes calculated according the equation above for L=59.5 mm. The reflected signal of the cavity as the input frequency is scanned from 14 - 26 GHz is shown in Figure 5-5. The resonance modes are identified by a decrease in the reflection signal which appears as sharp peaks in the reflection spectrum. The mode assignment and the reflection spectra are also depicted in Figure 5-5.

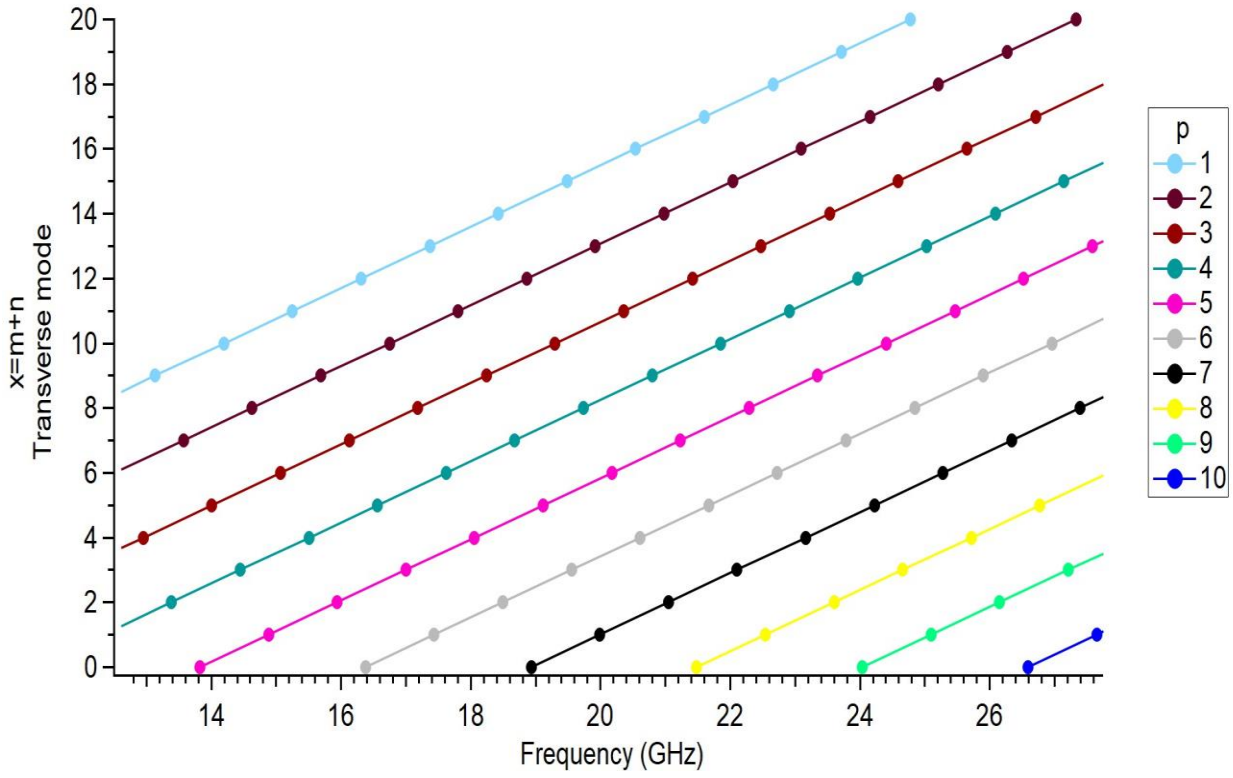

Figure 5-4: Frequency of various modes inside the Fabry Perot resonator calculated using equation (4-8) with L=60 mm

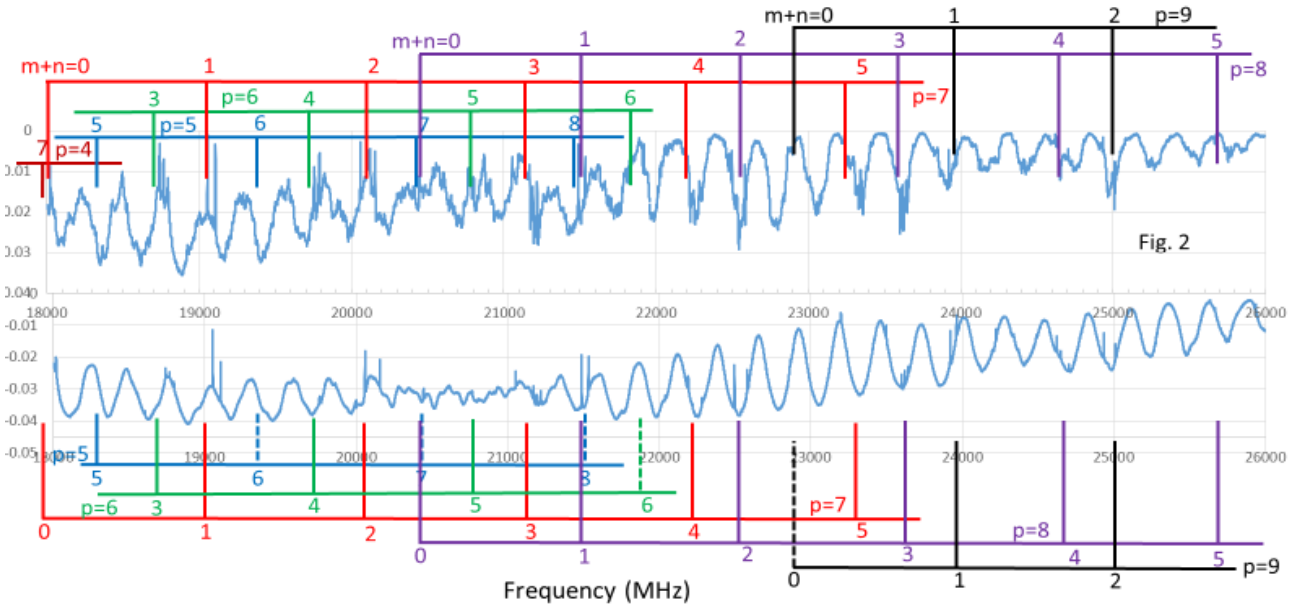

Figure 5-5: Mode assignment inside the cavity. The top panel shows the expected locations of peaks and the bottom panel shows the experimentally measured reflection signal as a function of input frequency. The signal generator is used to scan the input frequency from 14-26 GHz and only a part of that spectrum is shown in the figure (18-26 GHz).

5.3.1 Quality factor

The quality factor of a cavity depends on the energy loss inside it. In general, it is defined as

$$Q = \frac{2\pi\nu W dt}{dW} \tag{5.3}$$

Here, W is the energy stored in the cavity and ν is the input frequency. It is the ratio of energy stored to the energy lost per cycle inside the cavity. This implies that the energy stored inside a cavity, W at a time t, can be expressed as,

$$W = W_O e^{-\frac{\omega t}{Q}} \tag{5.4}$$

where W_O is the energy stored at time t=0.

The unloaded quality factor $Q_{O,}$ can be expressed as [81]

$$\frac{1}{Q_O} = \frac{1}{Q_r} + \frac{1}{Q_d} + \frac{1}{Q_{others}} \tag{5.5}$$

where Q_r, Q_d and Q_{others} are the quality factors due to the energy loss from finite surface resistance, diffraction and other factors such as the coupling to input antenna, and contact resistance in cavity parts, respectively.

a) The diffraction loss is caused by the finite diameter of the mirror. The quality factor determined by this loss is given as

$$Q_{diff} = \frac{2\pi\nu L}{c} \exp\left(\frac{D^2}{2w^2\left(\frac{L}{2}\right)}\right) \tag{5.6}$$

For our case with D=80 mm, $Q_{diff} = 2 \times 10^7$

(b) The surface resistance R_S is given as $R_0 + R_{BCS}$, where R_0 is the surface resistance at 0 K. The temperature dependence of surface resistance is considered by R_{BCS} which is proportional to temperature as [110],

$$R_{BCS} \propto \frac{\vartheta^b}{T} e^{-\frac{\Delta}{k_B T}} \tag{5.7}$$

At T>2 K, R_{BCS} is dominant. The value of R_{BCS} at a frequency of 24 GHz and a temperature of 4.17 K is 0.16 mΩ, which corresponds to a $Q_r = 1.8 \times 10^7$.

(c) The molecular beam and the MW antenna are introduced through holes at the center of the mirrors. For the hole radius with a_h = 2.5 mm and hole length d_h = 6 mm, the quality factor Q_h is of the order of 10^8.

Therefore, the estimated quality factor for our cavity at 3 K is 8×10^6 .

The Q factor is also related to FWHM of the reflected signal from the cavity and is given by

$$Q_L = \frac{\vartheta}{\delta\vartheta} \tag{5.8}$$

where ϑ is the resonance frequency and $\delta\vartheta$ is FWHM of the reflection signal. Here, Q_L is the loaded quality factor of the cavity and is related to the unloaded Q factor, Q_O as

$$\frac{1}{Q_L} = \frac{1}{Q_O} + \frac{1}{Q_C} = \frac{1+\beta}{Q_O} \tag{5.9}$$

In the above equation, Q_C is the quality factor due to input coupler and the parameter β, called as coupling parameter and is defined as

$$\beta = \frac{Q_O}{Q_C}$$

At critical coupling, which occurs when all the input power goes into the cavity and the reflection signal is zero, $\beta = 1$ and $Q_O = 2Q_L$.

The Q factor also depends on the insertion depth of the antenna inside the cavity. We have measured the Q factor as well as the coupling strength at various insertion depth of the antenna which is shown in Figure 5-6. The x axis in this figure represents the insertion depth of the antenna inside the cavity. At zero position on the x axis, the antenna is completely inside the cavity. As the value on x axis increases or as the nut on the feedthrough is rotated in counterclockwise direction, the antenna is pulled out of the cavity. At the far right on x axis, the antenna is completely out of the cavity and no reflection signal was thus observed beyond this position. The coupling strength is directly proportional to amplitude of the reflection signal. To get the maximum electric field inside the cavity, critical coupling is desired when all the power goes inside the cavity. At very high insertion depth (<1.75 turns), the cavity is over coupled, and the Q factor decreases as the antenna acts as a normal conductor thereby, causing loss of energy from the cavity. At critical coupling, the reflected signal pulse amplitude is maximum. Pulling the antenna further out from the critical coupling position (1.75 turns), the amount of power going into the cavity decreases but the quality factor increases and is termed as under coupling regime. The increase of Q factor as

the antenna is pulled out is due to decrease in the surface resistance of the cavity as the antenna acts as a part of the mirror surface.

By using equation 5-8, and the reflection signal measurements, we can measure the Q factor experimentally. Figure 5-7 shows the reflection signal for $TEM_{0,1,9}$ mode as the input frequency is swept near resonance frequency (24.0127 GHz). The y axis is the reflection signal and there is an offset of 0.9 mV due to our detector. So, 0.9 mV corresponds to no reflection signal from the cavity. The solid trace is the fit curve of the experimental data using a Lorentzian function.

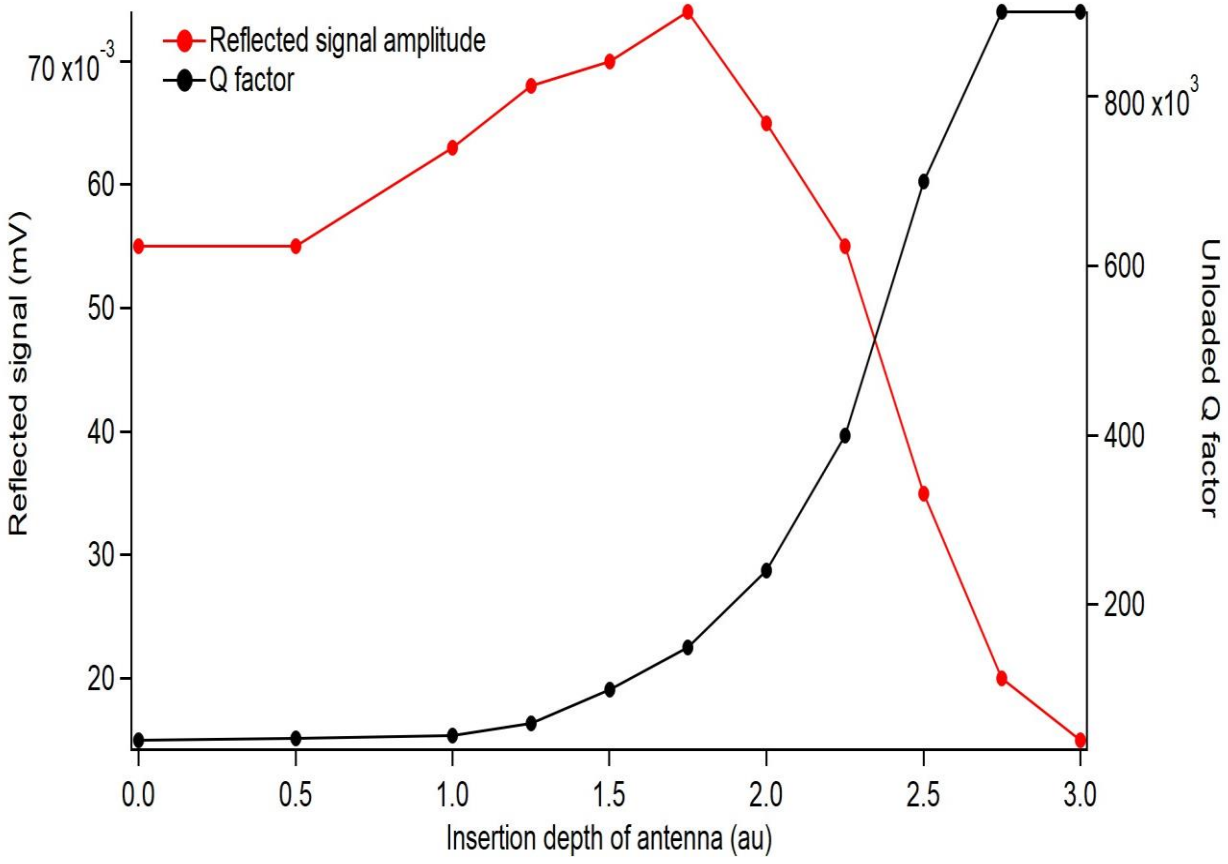

Figure 5-6: Reflected signal amplitude and Q factor dependence on the insertion depth of antenna. The mode used is TEM_{019}. The insertion depth can be controlled by a nut located outside the chamber on the input feedthrough for antenna. The x axis denotes the number of turns rotated in a counter clockwise direction.

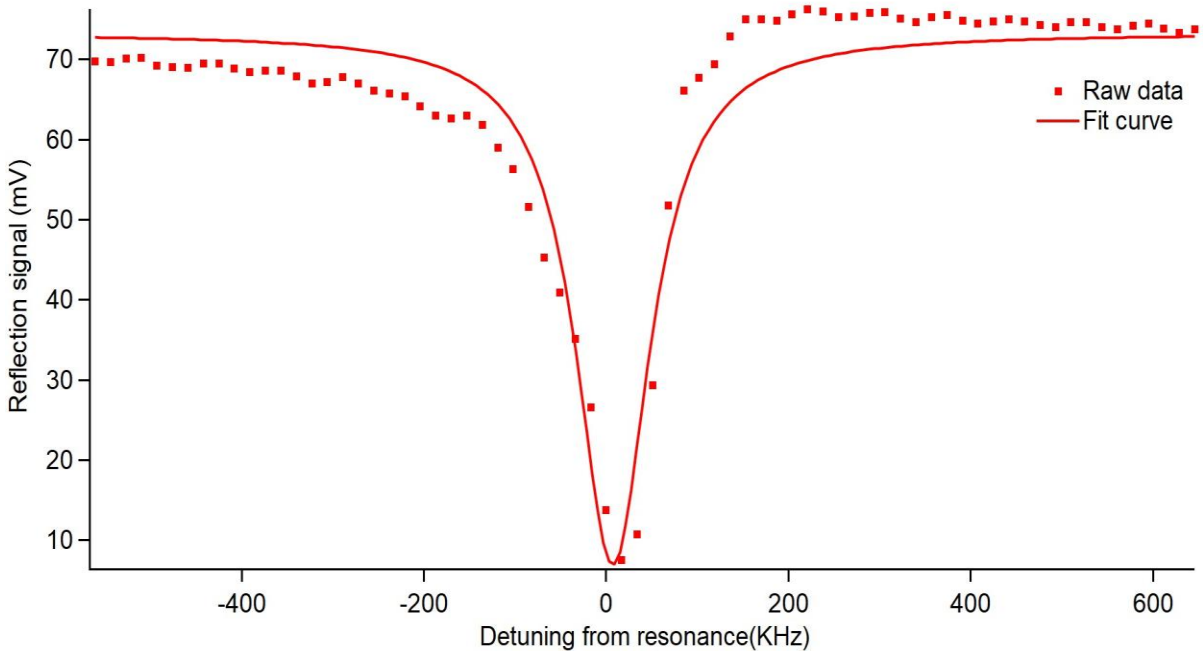

Figure 5-7: Reflection signal of TEM_{019} mode to determine the Q factor experimentally. The y axis is the reflection signal and the resonance frequency is determined when this signal is minimum. The resonance frequency for TEM_{019} mode is 24.0127 GHz.

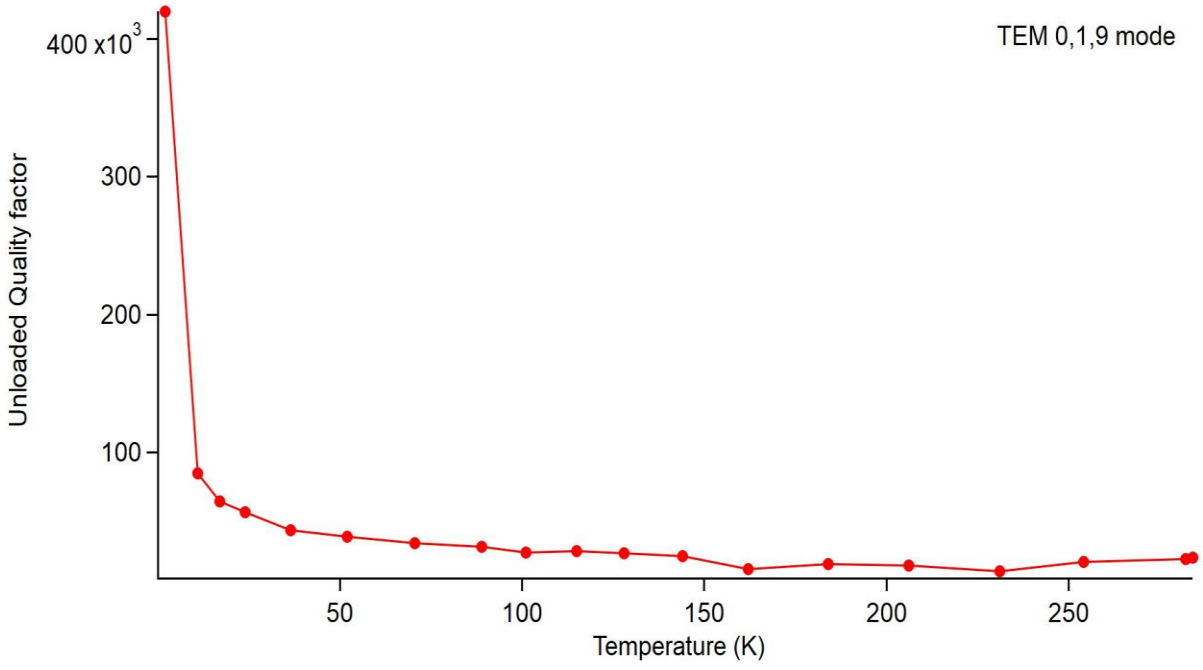

Figure 5-8: Unloaded quality factor of TEM_{019} mode as a function of temperature. The critical temperature for the superconducting material (Pb-Sn) is 7-8 K. The antenna position is put in critical coupling position.

The temperature dependence of the quality factor is shown in figure 5-8. The quality factor increases with decreasing temperature as the surface resistance decreases. The quality factor suddenly increases at very low temperature, and Q_O exceeds 400,000 at 3 K, where the Pb/Sn surface of the cavity becomes superconductor. The superconducting material has a critical temperature of 7-8 K. This result indicates that $Q_0 = 2 \times 10^4$ obtained at a room temperature is dominantly limited by the surface resistance and not by the diffraction loss which suggests that reducing the temperature of the surface resistance, we can achieve a higher quality factor with the current design of the cavity.

The Q factor of different modes inside the cavity is given in Table 5-1. As can be seen in equation (5-2), some modes for which m+n>0, have identical frequency, so it is difficult to identify those modes in the reflection spectrum. For example, TEM_{038}, TEM_{128}, TEM_{218}, TEM_{308} have same frequency and their reflection signal is closely spaced in the reflection spectrum. One way to distinguish the higher order transverse modes from lower order transverse modes is their low Q factor as can also be seen in Table below. The axial modes for which m=n=0 have very low Q factor in our cavity, which is due to loss from the transmission holes in the two mirrors. We could only identify $TEM_{0,0,7}$ mode inside our cavity as other higher axial modes were difficult to observe. As the cavity is cooled from room temperature to 3 K, the distance between the mirror changes. We measured the frequency shift of a resonance mode (TEM_{019}) as the cavity is cooled from room temperature to 3 K. The frequency change due to temperature was found to be 60 MHz If the distance between the mirrors is changed by 0.5 mm, it corresponds to a shift of 196 MHz approximately. After mode assignment is performed at a given length, the mirror spacing can be changed at room temperature in order to shift the resonance frequency of the cavity to the desired value.

Table 5-1:Mode parameters of the Fabry Perot cavity at 3 K. The mirror spacing is 61 mm.

Mode $TEM_{m,n,p}$	Frequency (GHz)	Q_O factor (x 10^5)
007	18.08	0.14
017/107	19.118	4.9
018/108	21.56	5.5
019/109	24.02	4.02
027/207/117	20.126	2.4
028/208/118	22.573	4.5
029/209/119	25.018	5
036/126/216/306	18.83	0.23
037/307/127/217	21.125	0.36
	21.266	0.18
038/308/128/218	23.576	1.68
	23.681	0.43
	23.701	1.08

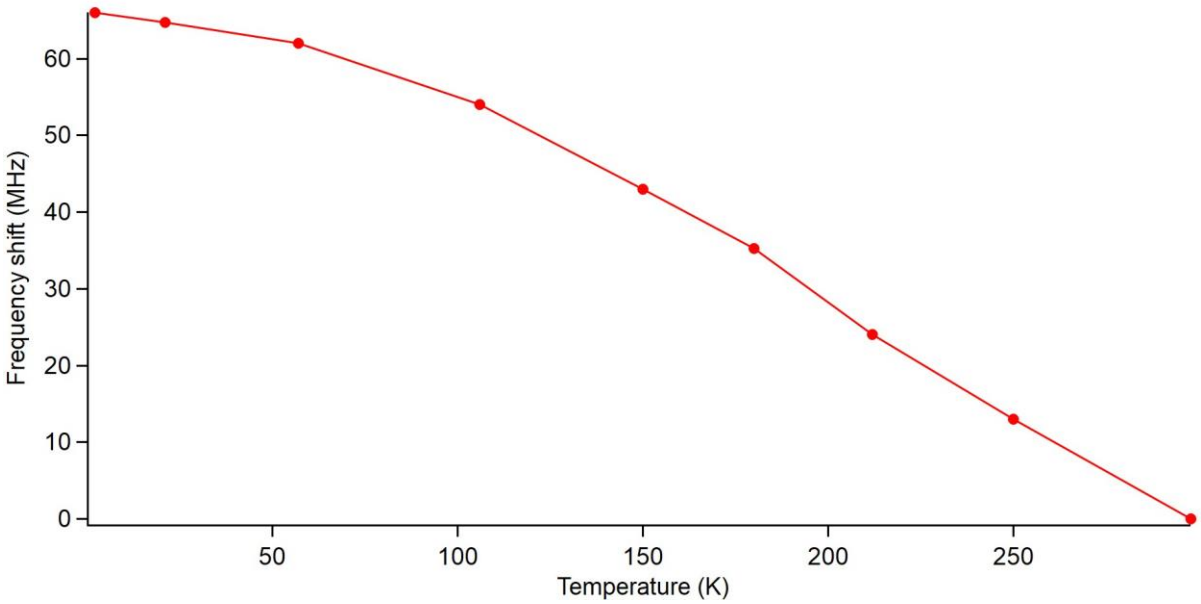

Figure 5-9: Shift in resonance frequency for mode TEM_{019} as a function of temperature. The resonance frequency is blue shifted by 60 MHz as the cavity is cooled from 298 K to 3 K.

5.4 Results and discussion

We had chosen $TEM_{0,0,9}$ mode as the resonator mode for trapping NH_3 molecules. In such a mode, the electric field is maximum on the longitudinal axis as there are no transverse excitations. The

$TEM_{0,0,9}$ mode has nine antinodes located axially along the length of the cavity. But, the quality factor of all the axial modes was very small due to scattering losses from the transmission holes in the mirrors. So, we used TEM_{029} mode which has a much larger Q factor than $TEM_{0,0,9}$ as well as a maximum electric field at the center of the cavity. The need of maxima at the center of cavity arises for detection purpose. If the ammonia molecules are ionized away from the cavity center, the detection efficiency of ion optics decreases.

5.4.1 Rotational assignment of transitions in ammonia molecular beam

We used PGOPHER program to assign the rotational transitions in ammonia. The rotational temperature of the ammonia molecular beam mixed with Argon gas at a pressure of 3 bar was estimated to be 5 K using PGOPHER. We also confirmed the rotational assignments using a Stark decelerator in guiding mode which is depicted in Figure 5-10. The ammonia molecular beam was passed through the Stark decelerator while it was operating in guiding mode. In guiding mode, all the electrodes are kept at a certain voltage so that the stark decelerator can provide a focussing force for LFS states of ammonia molecules. Since, the lower inversion doublet is a HFS state, the intensity of this transition decreased when the ammonia beam was passed through the stark decelerator.

5.4.2 Broadening of line width with laser power

We measure the AC stark shift by comparing the J=1, K=1 transition by turning the MW radiation on and off inside the cavity. As the magnitude for AC stark shift is quite small, in order to differentiate between the two traces (MW on and off), it was helpful to minimize the line width of

the transition by reducing the laser power. This broadening of spectral line shape at a high laser power is termed as power broadening. At the same time, the signal intensity of ionized NH_3

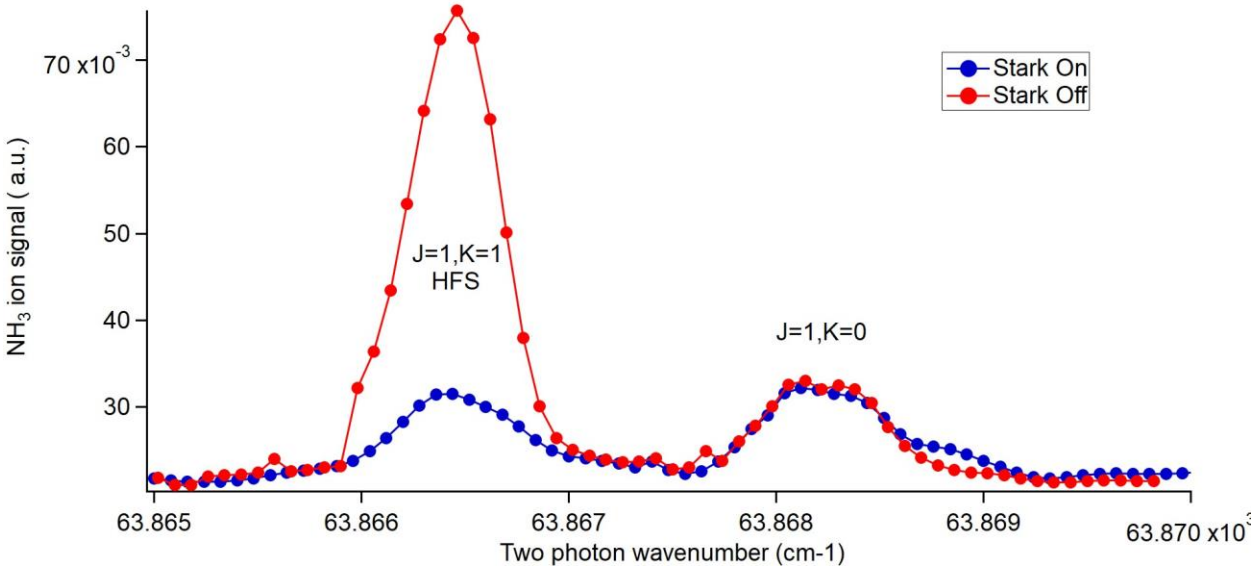

Figure 5-10: Rotationally resolved frequency spectrum of ammonia mixed with Argon gas at a pressure of 3 bar after passing through a stark decelerator. The blue trace is recorded by applying a voltage of +-5kV on all electrodes while the red trace is recorded with 0 kV.

the transition by reducing the laser power. This broadening of spectral line shape at a high laser power is termed as power broadening. At the same time, the signal intensity of ionized NH_3 molecules decreases as it is directly proportional to laser power. Therefore, the minimum signal to noise ratio required in order to measure the AC stark shift was calculated and the laser power was reduced to such level. Figure 5-11 shows the J=1, K=1 transition which is measured in the ammonia beam at different laser energy. The three measurements are normalized to each other. The laser energy was varied between 0.38 -1.6 mJ and the FWHM of each measurement is shown in Table 5-2. As the FWHM was least at 0.38 mJ, we used this laser energy in our experiment to measure the AC stark shift for NH_3.

Table 5-2: FWHM of J=1, K=1 transition at different laser energy.

Laser energy (mJ)	FWHM(cm^{-1})
0.38	0.46
1.1	0.50
1.6	0.64

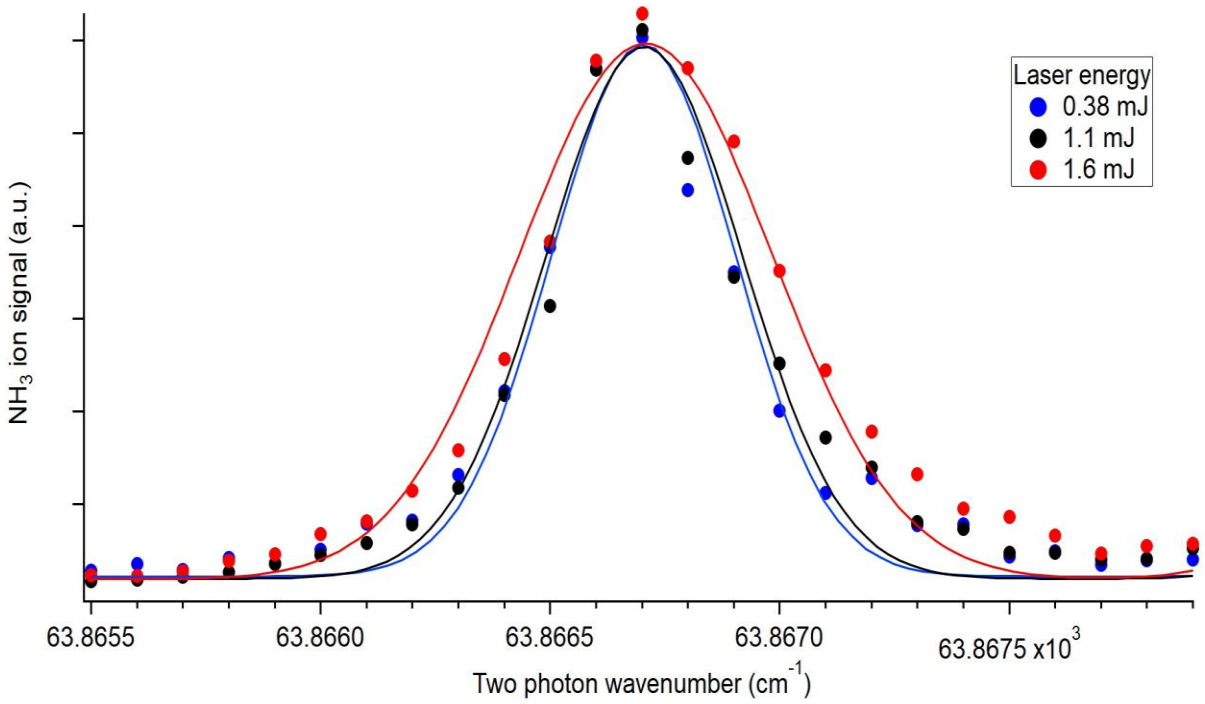

Figure 5-11: Power broadening in the J=1, K=1 transition in NH_3 molecular beam mixed with argon gas at a pressure of 3 bar at different laser energy.

5.4.3 AC Stark shift in NH_3

Figure 5-12 shows the AC stark shift in ammonia molecule inside the superconducting Fabry Perot cavity using the TEM_{029} mode. The blue trace corresponds to J=1,K=1 transition when a MW pulse with a duration of 300 μs was applied inside the cavity. The laser delay was set to the peak

time of flight distribution of the ammonia molecular beam. At a Q factor of 5 x 10^5, the build up time for the standing waves or the electric field is around 20 μs,which can be calculated using equation 5.4. Therefore,the MW pulse was turned on atleast 150 μs before the time of arrival of the molecular beam. The black trace shows the difference between the fit curves of the experimental data. The experimentally measured AC stark shift is 0.02 cm^{-1} which is measured by the difference on the x axis between the two traces at a wavenumber of 63866.4 cm^{-1}. This shift is smaller than expected which is 0.05 cm^{-1} at an electric field of 1 MV/m and a blue detuned frequency of 385 MHz as shown in Figure 5-13.

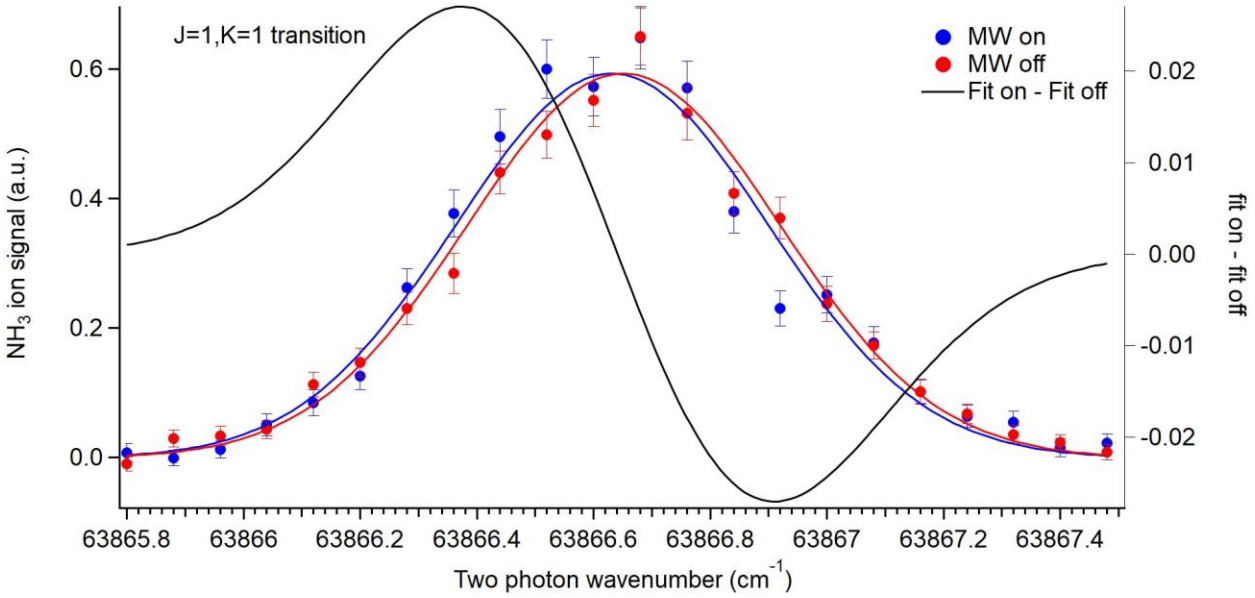

Figure 5-12: J=1, K=1 transition in ammonia molecular beam for measurement of AC stark shift. The blue trace is measured in presence of MW radiation inside the cavity whereas the red trace is measured without any MW radiation. A MW pulse of total duration of 300 us is applied such that the ionized ammonia experiences electric field due to MW radiation. Alternatively, on and off shots are measured. Each point is an average of 256 shots. The black trace is the difference between the fitted curves of raw data.

The difference between the experimental measurement and the expected shift could be due to two reasons. Firstly, the power loss due to the antenna is unaccounted for and more detailed measurement needs to be carried out in order to correctly estimate the power going into the cavity.

Secondly, in order to record the maximum AC stark shift, the laser detection point and the electric field maxima location inside the cavity must overlap, which is difficult to confirm. These two factors need to be carefully examined in the future, to account for the deviation between the theoretical and experimental measurement.

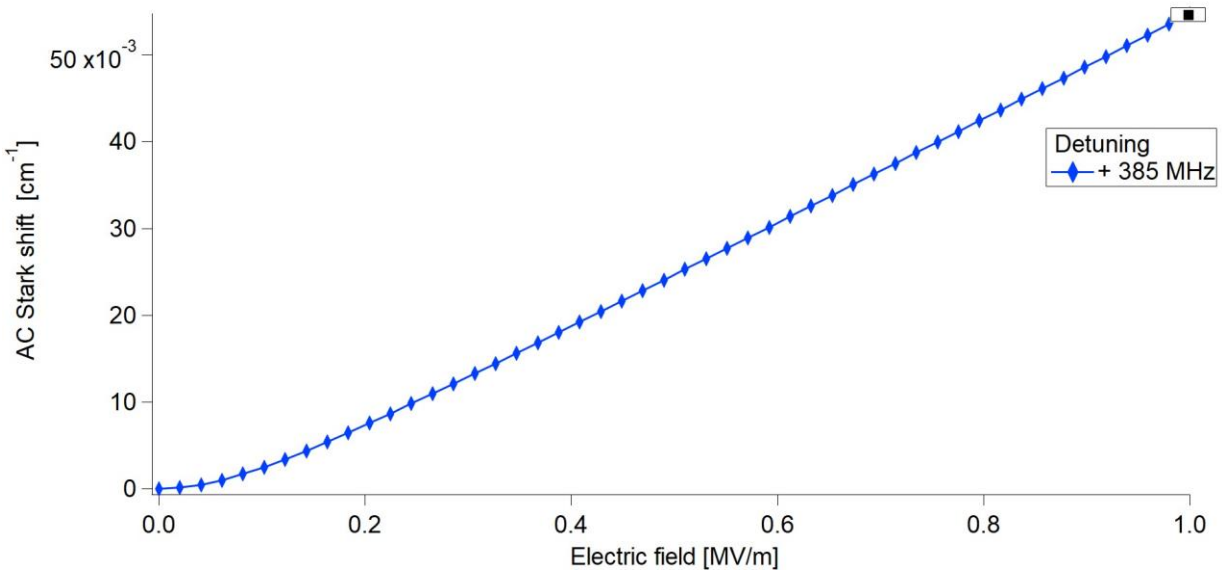

Figure 5-13: AC stark shift of NH_3 in lower level of the inversion doublet at a detuning frequency of 385 MHz, power input of 10 W and a Q factor of 5 x 10^5. The black dot on the trace denotes the expected AC stark shift at the experimental conditions.

5.5 Conclusion and future outlook

In this chapter, the characterization of a superconducting Fabry Perot cavity is discussed. At a Q factor of 5 x 10^5 and a power input of 10 W, an electric field of 1 MV/m was generated. The AC stark shift of ammonia was measured using a molecular beam of ammonia mixed with argon gas at this electric field. The next step is to attach the cavity at the exit of a Stark decelerator for trapping. The stark decelerator will reduce the speed of ammonia molecules such that they can be trapped in the MW cavity. Figure 5-14 shows the cavity attached behind a stark decelerator. A hexapole is placed between the cavity and the stark decelerator in order to guide the decelerated

ammonia molecules to the cavity. The trap depth of our cavity at an electric field of 1 MV/m is around 80 mK which corresponds top a speed of 10 m/s. In order to increase the trap depth, we are constructing a new cavity which will have smaller transmission holes in the center such that scattering loss through the center is minimized. We could use the axial modes for trapping of ammonia since the axial modes have a higher Q factor in comparison to transverse modes. With the new cavity, if a Q factor of 10^7 is achieved, at MW power input of 10 W, the trap depth for can be increased to 250 mK corresponding to a speed of 15 m/s. Once, ammonia is trapped, the power input can be lowered such that the trap depth is slowly reduced in order to reduce the temperature of ammonia molecules using evaporative cooling.

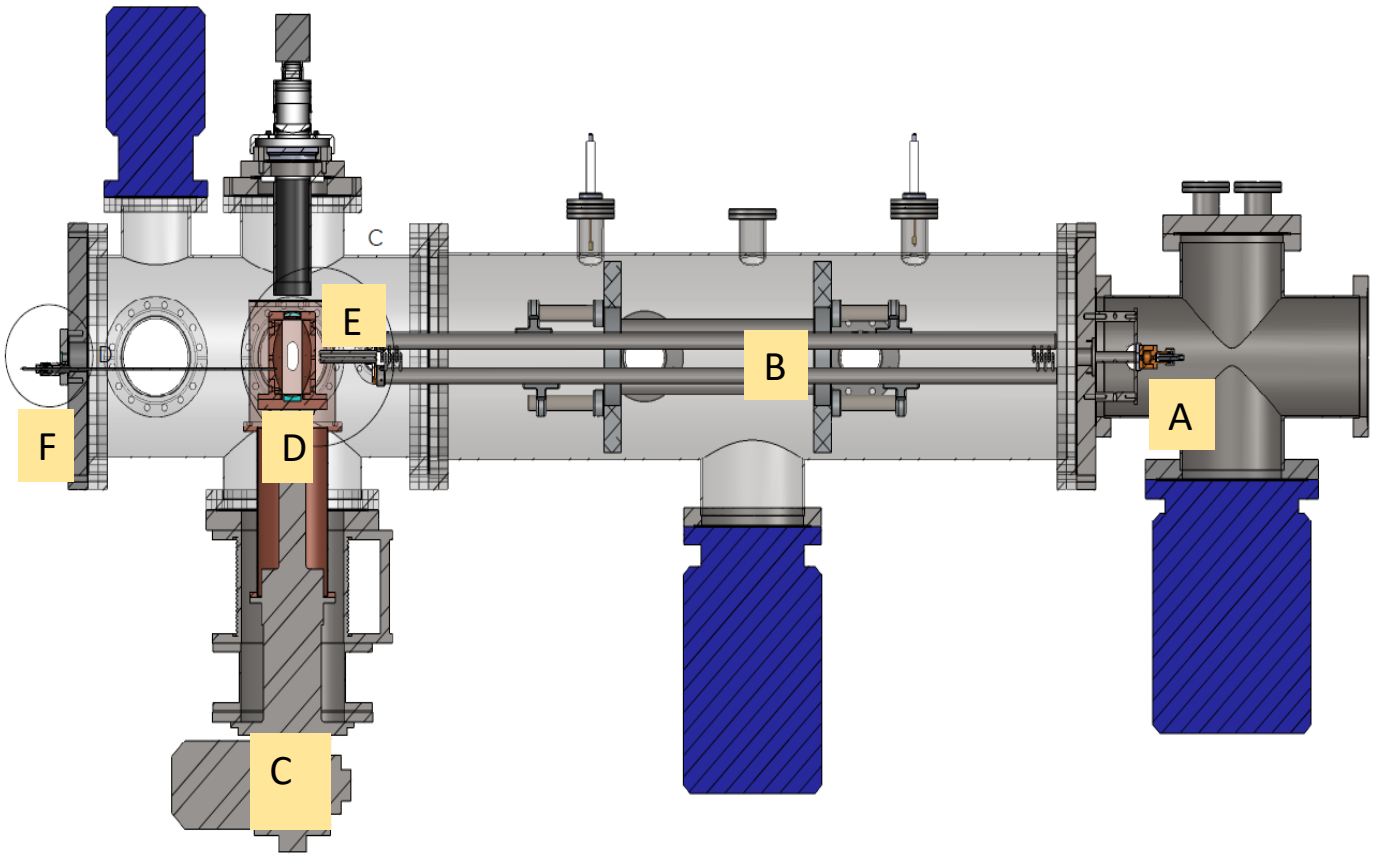

Figure 5-14: Experimental setup for the trapping of ammonia in a MW cavity. It consists of a pulsed nozzle (A), 180 electrodes stark decelerator (B), closed cycle refrigerator (C), MW cavity (D), hexapole (E) and MW feedthrough (F).

6 Slowing polyatomic molecules using a counter rotating nozzle

6.1 Introduction

This chapter describes a mechanical method to slow down any type of atom or molecule using a counter rotating source. The first use of a rotating source to manipulate the motion of molecules was reported by Philip Moon in 1950 [111]. He used the rotating source to generate fast and intense beams for crossed beam studies of chemical reactions. However, the technique to generate slow molecules by mechanical means was pioneered by Gupta and Hersbach [112]. They employed a counter rotating nozzle to reduce the translational kinetic energy of atoms relying on the principle of Galilean transformation between the laboratory rest frame and the nozzle's moving frame. However, their design had several shortcomings such as the use of a special aluminium alloy barrel as the rotor which was difficult to machine. Secondly, the gas injection system which was a polymer needle inserted into the rotor suffered abrasion resulting in gas leakage inside the source chamber. This was a serious limitation in order to produce dense beams which were attenuated as a result of collision with background gas in the nozzle chamber. Strebel et al. [113] improved upon these two shortcomings and reported density of the order of 10^{11} /cc from a CRN source using argon atoms. Their design used a continuous source for gas inside the rotor which limited the pressure behind the nozzle. The maximum reported pressure was around 450 Torr as it leads to detrimental effects on the molecular beam due to background gases in the nozzle chamber. Sheffield et all [114,115] also use a pulsed source for CRN and they have reported a density of the order of 10^{13}/cc at a pressure of 900 Torr. In this chapter, we consider this mechanical method of producing cold molecules and atoms with several modifications to the previous designs. With the installation of a pulsed source and high speed gated shutter in front of the skimmer in our

experimental setup, we have been successful in reducing the background pressure and hence, in achieving dense and cold molecular beams. Longitudinal temperature as low as 160 mK with translational speed of less than 110 m/s has been observed for acetone molecules seeded in krypton gas and a density of the order of 10^{16} /cc is estimated using argon atoms.

6.2 Experimental setup

The experimental setup is illustrated in Figure 6-1, which consists of a counter rotating nozzle(A), shutter(B), skimmer(C), copper cavity(D), UV laser(E), ion optics(F) and a micro channel plate(G) for detection of ionized molecules.

The molecular beam source is comprised of a counter rotating nozzle(A) with a diameter of 200 μm mounted on the end of a carbon fiber tube. The carbon fiber tube is hollow with an inner diameter of 2.5 mm and an outer diameter of 4.0 mm. The rotor is made of carbon fiber due to its high strength to withstand high centrifugal forces at the operating rotation frequency of the rotor. The rotor is rotated by a brushless DC motor in a vacuum chamber as shown in Figure 6-2. The length of the carbon fiber tube is about 36 cm while the length from the titanium nozzle tip to the spindle is 19 cm.

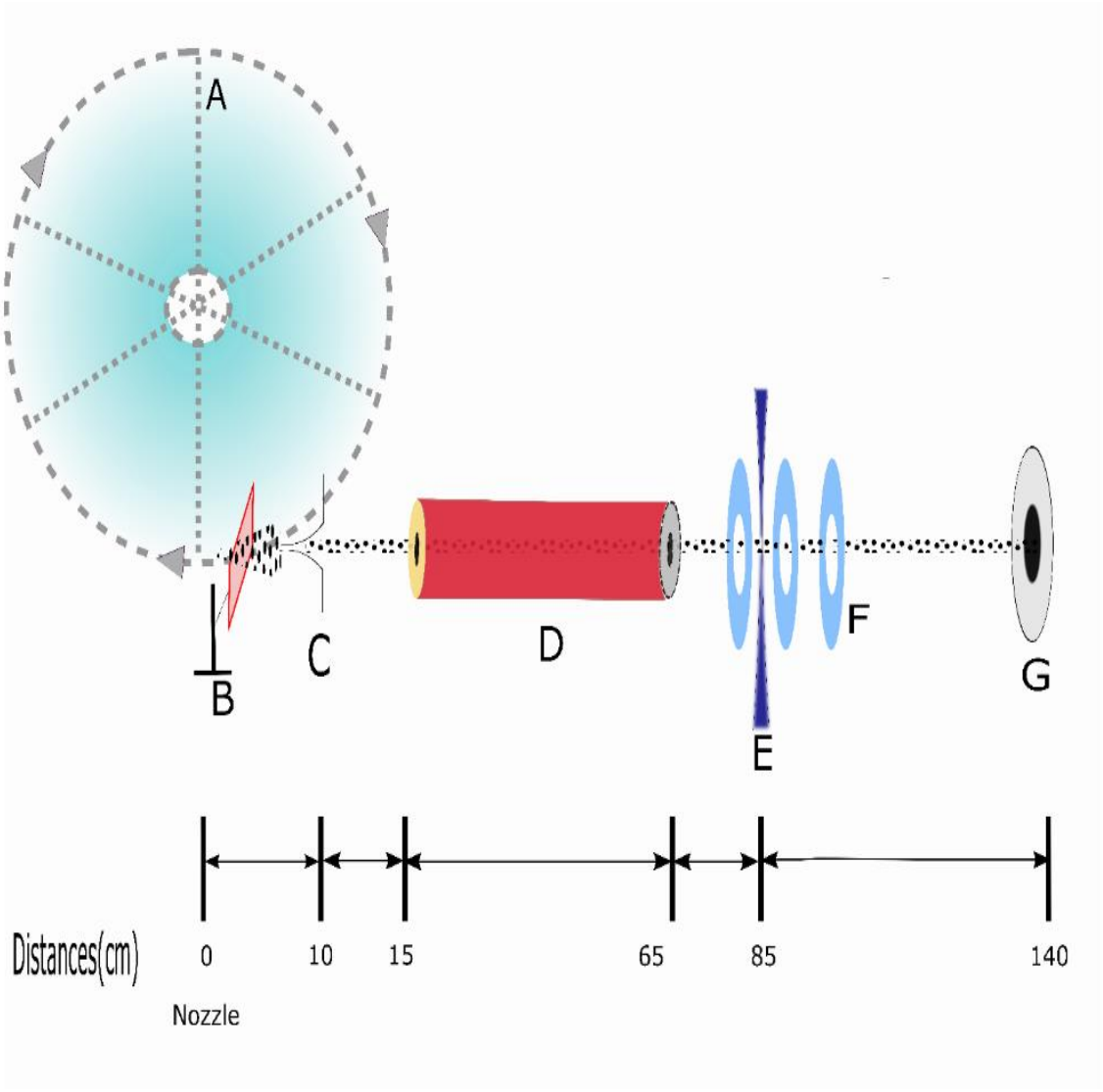

Figure 6-1: Schematic overview used for characterizing quasi-pulsed and counter rotating nozzle source. consists of counter rotating nozzle(A), shutter(B), skimmer(C), copper cavity(D), UV laser(E), ion optics(F) and micro channel plate(G) for detection of ionized molecules

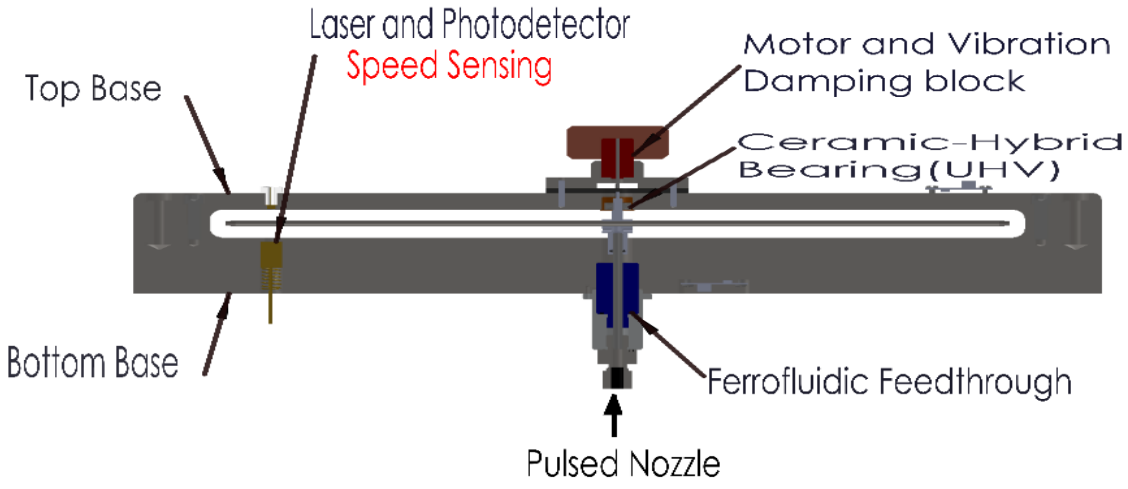

Figure 6-2:Cross section view of the rotor assembly

The center of the rotor is attached to a ferrofluidic feed through for inlet of gases inside the tube. The valve and ferrofluidic feed through are coupled through an aluminum ferrule that fits closely into a housing. The spindle (titanium) O-ring is sealed to the ferrofluidic shaft. The opposite side of spindle is coupled to the motor with soft silicone tubing. A large copper block attached to the motor is water cooled to remove excess heat from the motor.

A pulsed valve (General Valve, 9 Series) is attached at the inlet of the ferrofluidic feed through to allow gas input to the rotating nozzle. The gas mixture is made by bubbling krypton gas through acetone which is stored as a liquid in a small tube. Hence, the krypton gas reaching the valve is saturated with acetone molecules.

Our source chamber is pumped by an 800 l/s turbo pump and detection chamber is pumped by a 300 l/s turbo pump. Maintaining a pressure of 4 bar behind the nozzle, the peak background pressure in the source chamber remains close to 10^{-4} Torr during experiments. At a distance of 10

cms from the nozzle, a skimmer separates the source chamber from the detection chamber. A mechanical shutter is placed between the skimmer and the nozzle to restrict gas flow contributed by continuous molecular beams from the rotating nozzle. Furthermore, there is a superconducting cavity installed after the skimmer for application of MW dipole force on the molecular beam. The characterization of this cavity has been discussed in previous work by our group [92]. The pressure in detection chamber does not rise considerably during valve operation as the cavity is maintained at 3 K which condenses any background gases. The cavity is constructed from a 508 mm long, 12.6 mm inside diameter copper tube and two copper end caps with a thickness of 4mm. Each end cap has a hole at the center to let molecular beam pass. The diameter of the entrance hole is 6 mm and that of the exit hole is 4.5 mm.

Behind the exit of the copper cavity, ion optics are installed for guiding the laser ionized molecules in the molecular beam towards a micro channel plate in the detection chamber. The MCP output signal is further amplified by two RF voltage amplifiers. The output signal from RF amplifiers is recorded on an oscilloscope which is acquired by a LabVIEW program.

6.3 Theory

For characterization of CRN, we measure the time of flight (TOF) distribution of acetone molecules seeded in krypton gas. Using MPI detection scheme, we measure the peak velocity and the FWHM of velocity distribution, whereas using RGA detection, we calculate the density of the beam from the CRN. This is due to the slow response of RGA which convolutes the measured signal, whereas, the MPI scheme provides direct measurement of velocity deviation of molecular beams. But, MPI cannot provide any information about the density, therefore we used RGA for density measurement. The gas mixture is composed of krypton gas which is bubbled through

acetone. The vapor pressure of acetone at room temperature is 0.25 bar. Thus, in a gas mixture with a total pressure of 4 bar, the mole fraction of acetone is 0.06. Using this concentration of acetone, the estimated initial velocity of the molecular beam is 430 m/s.

The experimentally measured time of flight distributions have been fitted in the same manner as by Strebel et al. as the experimental setup is identical in principal. The fitting function used to derive the FWHM of the molecular beams along the z direction which is the longitudinal direction at different conditions is given by [113]:

$$n_z = \sqrt{\pi}\sum_{i=1}^{3} A_i \left(\frac{1}{\Delta v_z^2} + \frac{t^2}{\Delta z_i^2}\right)^{\frac{-1}{2}} e^{\frac{-(z-z_i-v_0 t)^2}{\Delta z_i^2 + \Delta v_z^2 t^2}} \tag{6.1}$$

In the above equation, A_i denotes the amplitude factors which are found out by measuring the TOF from CRN at a very slow speed, as the measured TOF mainly shows effect of rotating nozzle in front of skimmer as the longitudinal spread in velocity is negligible due to high speed of molecular beam. The angle subtended by the rotor arm for detectable positions in our set up is ±7.2 degrees which is calculated as

$$\phi = \cos^{-1}(1-r/R)$$

where r is the radius of skimmer and R is the distance from spindle to nozzle. In our setup, r=1.5 mm and R=19 cm. As a result, the final measured TOF distribution is a convolution of shutter function and the velocity distribution of the molecular beam. The shutter function s_z, was calculated by fitting the experimentally measured TOF at 10 Hz and fitting it to a product of three Gaussian beams given by:

$$s_z(z) = \sum_{i=1}^{3} A_i e^{\frac{-(z-z_i)^2}{\Delta z_i^2}} \tag{6.2}$$

Where A_i are the amplitude factors, z_i are the center positions and Δz_i are the width for the three Gaussian beams.

We also determined the shutter function in the same manner. The measured TOF at 10 Hz using a beam of pure argon is shown in Figure 6-3.

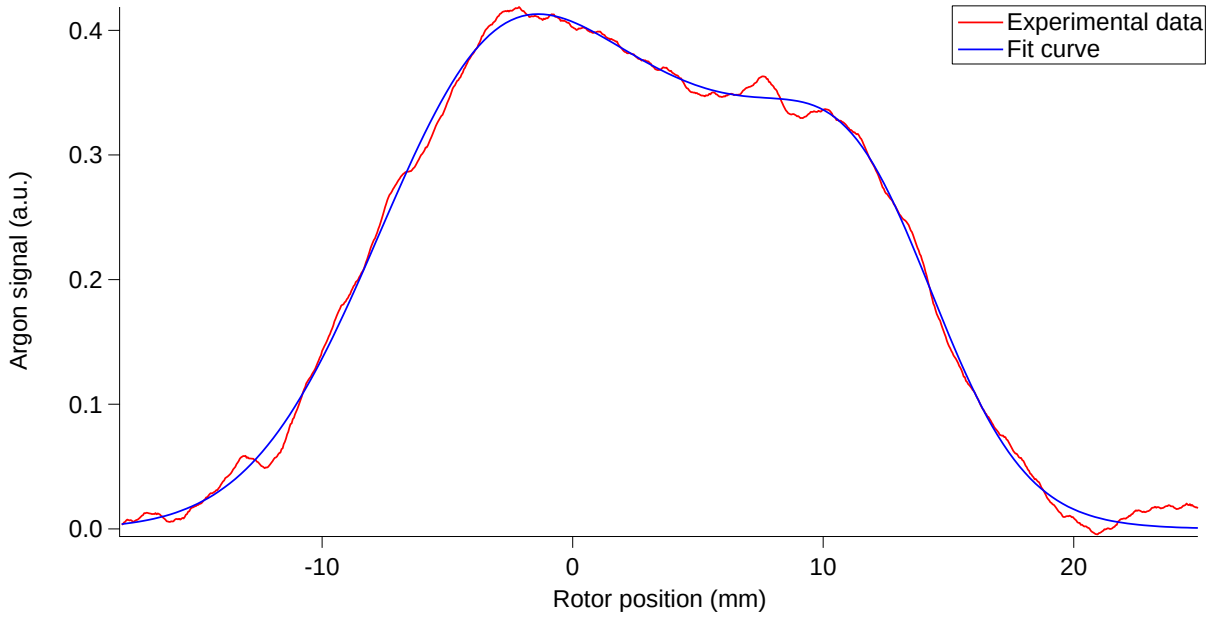

Figure 6-3: Shutter function measured at 10 Hz using a beam of argon atoms. The blue curve is a sum of three Gaussians centered at different positions on x axis

The pulsed valve is attached farther away from the tip of the rotating nozzle. The rotor volume acts as a reservoir which charges upon opening of valve. The valve opening duration controls the pressure inside the rotor. On the other hand, once the valve is closed, the rotor discharges from the CRN. The pressure-time relation inside the rotor can be found by integrating mass flow equations as given in [117]. For charging of rotor, the solutions can be written as:

$$P_{rotor} = VP_{source}\frac{tk}{A_v s}\frac{(k+1)}{2}^{\frac{k+1}{2(k-1)}} \tag{6.3}$$

Similar treatment during the flow of gases from the tip of the nozzle leads to pressure-time relations during discharge process.

$$P_{rotor} = P_i \left[1 + \frac{tsA_n}{V} \left(\frac{k-1}{2} \right) \left(\frac{k+1}{2} \right)^{\frac{-(k+1)}{2(k-1)}} \right]^{\frac{-2k}{(k-1)}} \tag{6.4}$$

where V is volume of rotor, P_i is the initial pressure in rotor, s is the speed of sound in the filling gas, A_n is the nozzle area, A_v is the area of general valve attached to the rotor.

6.4 Results and discussion

6.4.1 Effect of pressure

The total number of molecules per pulse is directly proportional to pressure behind the nozzle [113]. Figure 6-4 displays the increase intensity of acetone signal as the pressure behind the nozzle is increased from 1 bar to 4 bar. The variation in the peak velocity of the molecular beam at different pressure is due to increase in the mole fraction for krypton molecules in the gas mixture as the pressure is increased as the vapor pressure of acetone is constant. Since krypton is heavier than acetone, the beam slows as the pressure increases. In order to confirm this, the same experiment was done using a beam of pure argon atoms and detected by the RGA. There was no shift in the time of flight distribution of pure argon atoms as the pressure was increased from 1 bar to 6 bar as shown in Figure 6-5.

Table 6-1:Beam parameters at different pressure behind the nozzle rotating at 100 Hz with a valve opening duration of 4 ms of acetone molecules seeded in krypton gas

Pressure (bar)	FWHM (m/s)	Velocity(m/s)	Longitudinal Temperature(K)
1	113	413	44.5
2	96	376	32.1
3	74	339	19.1
4	59	330	12.1

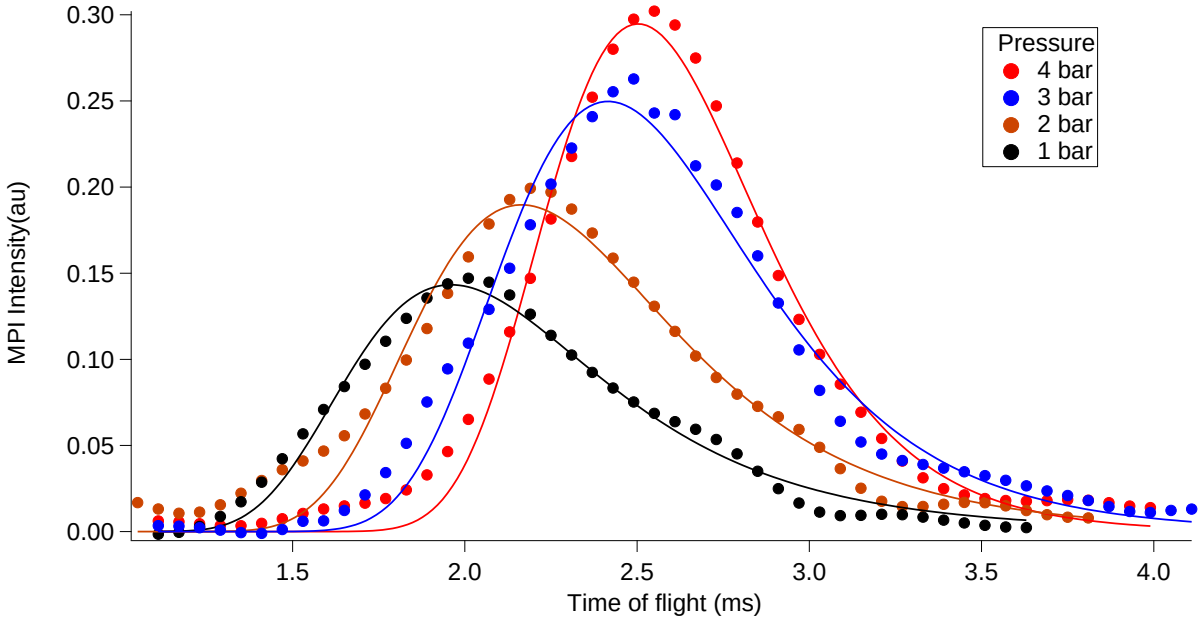

Figure 6-4: Time of flight distribution of acetone molecules seeded in krypton gas at different pressure using MPI detection scheme. The rotation speed of nozzle is 100 Hz. The valve opening duration is 4 ms.

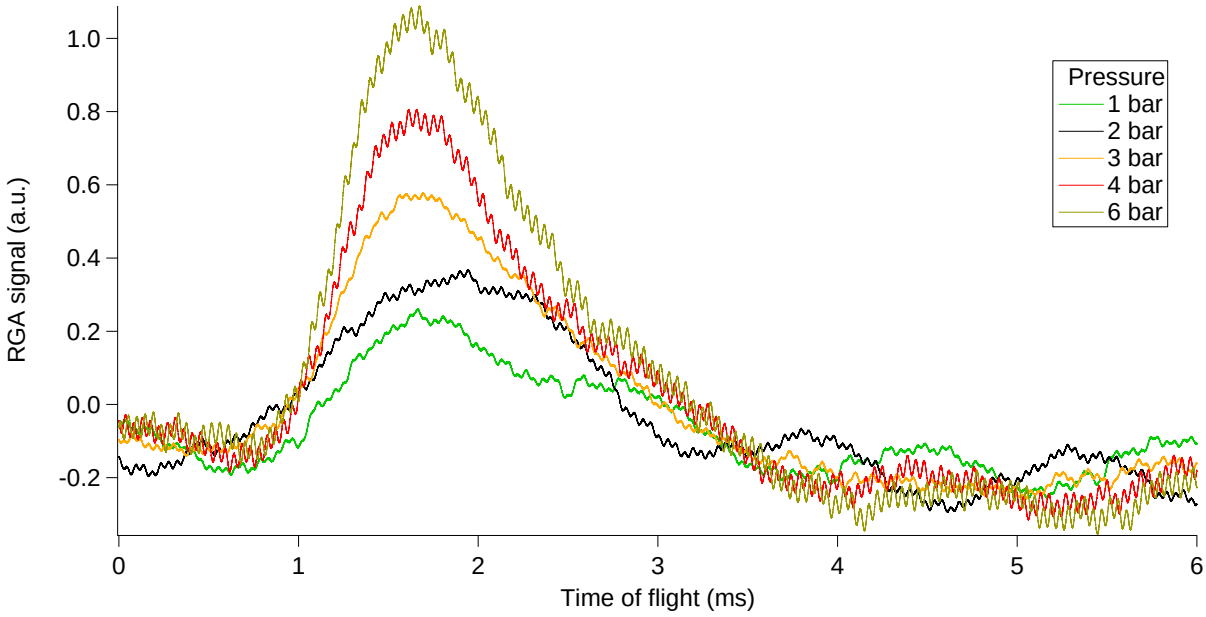

Figure 6-5:Time-of-flight distribution of pure argon beam from counter rotating nozzle at a speed of 50 Hz using RGA detector.

6.4.2 Discharge of rotor

For comparison of the theory for discharge of gas from the rotor with the experimental data, the peak pulse amplitude for successive pulses from the CRN are measured. Figure 6-6 shows the successive pulses of pure argon beam from the CRN rotating at a speed of 20 Hz. The pressure behind the nozzle was 4 bar with a valve opening duration of 2.5 ms. The y axis in Figure 6-6 is the signal measured using RGA detector. As the valve is opened at t=0 s, the first pulse which is selected by RGA is emitted from the CRN at 50 ms, corresponding to one period of rotation at 20 Hz. The amount of time required to fill the rotor is much less than one period of rotation such that the pressure in the rotor reaches a maximum for the first pulse and it decreases as the nozzle continues to emit gas. Due to decrease in pressure, the amplitude for successive pulses also decreases. Figure 6-7 shows the comparison of the decay curve of pressure inside the rotor according to equation 6.4 and the peak amplitudes of pulses at the same time.

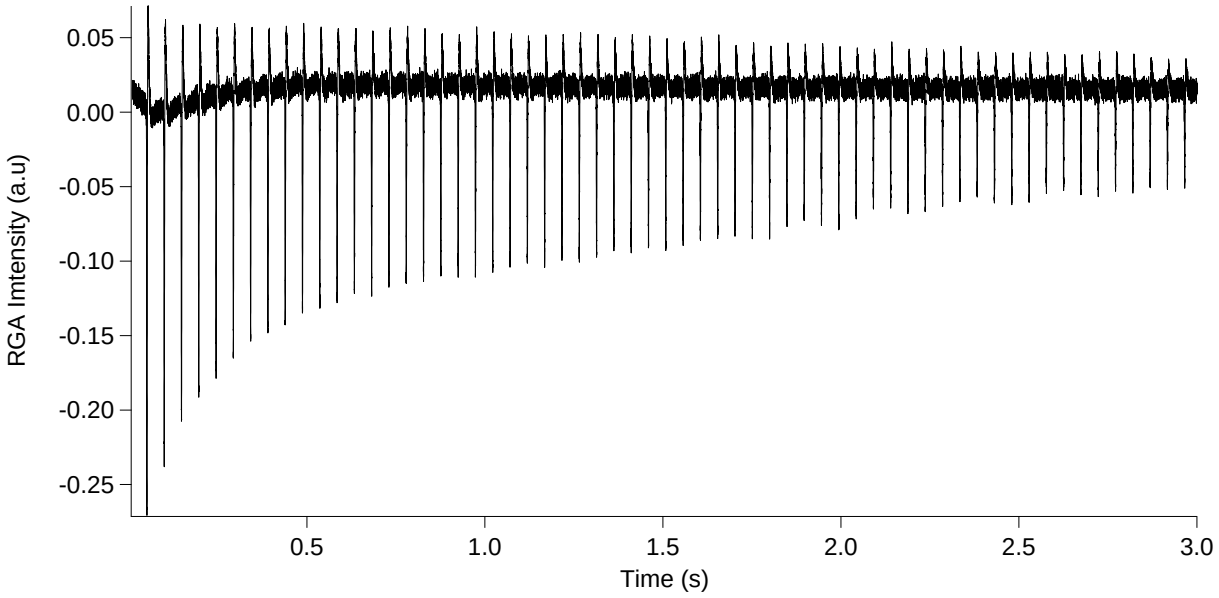

Figure 6-6: Successive pulses from a counter rotating nozzle at a rotation speed of 20 Hz using argon gas. Each pulse is separated by 50 ms which is the period of rotation of the counter rotating nozzle.

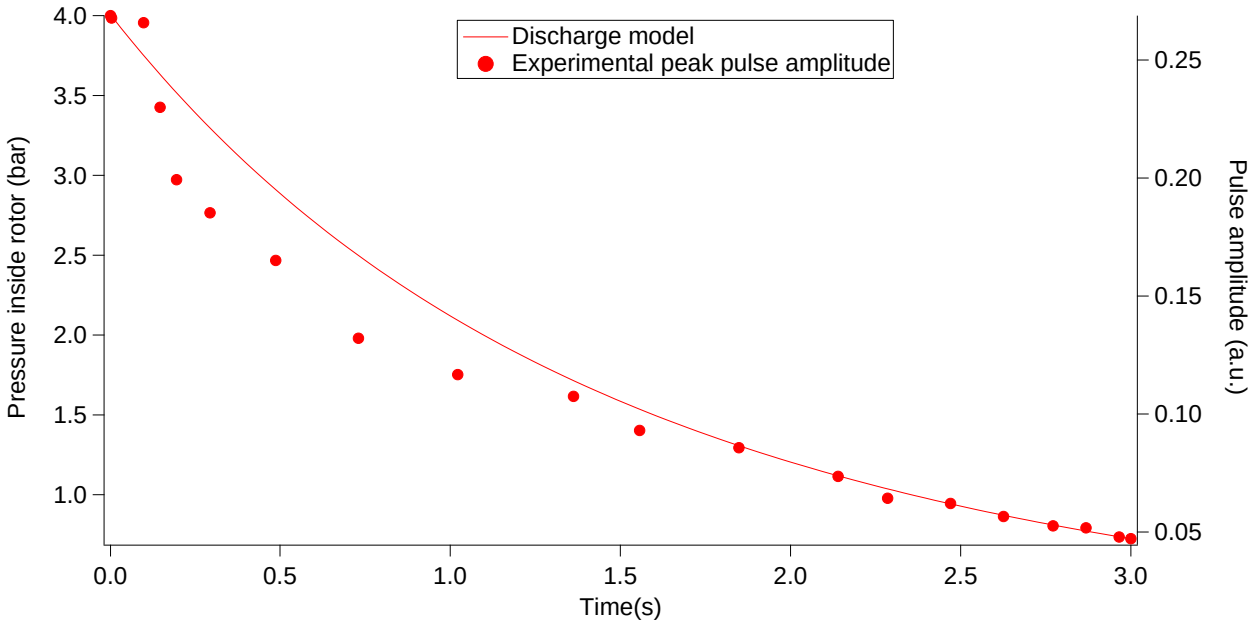

Figure 6-7: Discharge of rotor as a function of time. The red dots denote the peak pulse amplitude at a specific time as measured from Figure 6-6 and the red trace shows the decay of pressure inside a rotor which is filled to 4 bar at time t=0 with argon gas as calculated from equation 6-4.

6.4.3 Effect of valve opening duration

The valve opening duration determines the pressure of gas inside the rotor. The minimum valve opening duration for the General valve is 400 μs as we did not see any pressure rise in the nozzle chamber. The time taken to fill the rotor can be calculated according to equation 6.3. The pressure-time relation for charging of the rotor when the pressure behind the valve is 4 bar, is shown in Figure 6-10. Inside the rotor, the pressure rises to 4 bar at 2 ms which is same as the source pressure. The source pressure is the pressure behind the pulsed valve. Due to the rise in pressure as the valve opening duration is increased, the intensity of the beam increases as well. This can be seen in Figure 6-8 and 6-9.

In Figure 6-8, we can see that the intensity increases beyond an opening duration of 2 ms and the peak velocity of the molecular beam also varies as the valve duration is varied. This can also be explained as a result of increase in concentration of acetone in the gas coming out of nozzle. At longer valve opening durations, as the pressure decreases near the valve opening, acetone flows from the bubbler towards the valve. As a result, acetone sticks along the entire gas line in the form of liquid. As the concentration of acetone increases, the beam becomes faster and the signal increases as well. This behaviour was not observed using pure argon gas which can be seen in Figure 6-9. After 2 ms, the pressure inside the rotor is same as the pressure behind the pulsed valve, hence leading to no increase the molecular beam intensity beyond a valve opening duration of 2 ms.

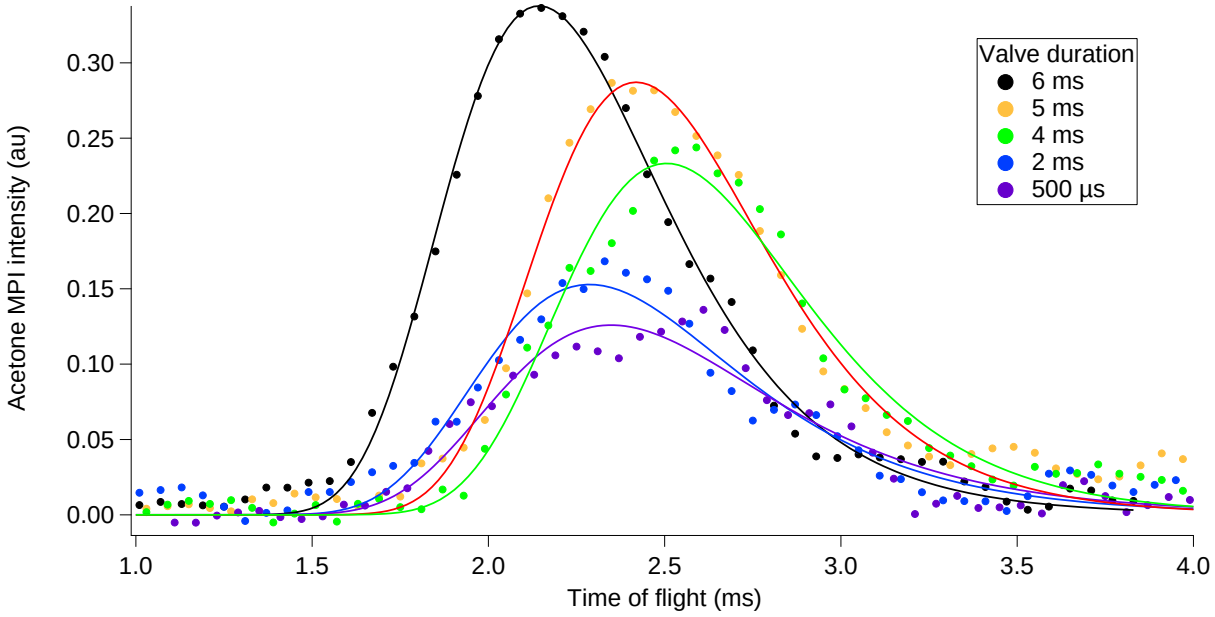

Figure 6-8: Time-of-flight distribution of acetone molecules seed in krypton gas from counter rotating nozzle at 100 Hz with a backing pressure of 4 bar at different valve opening duration.

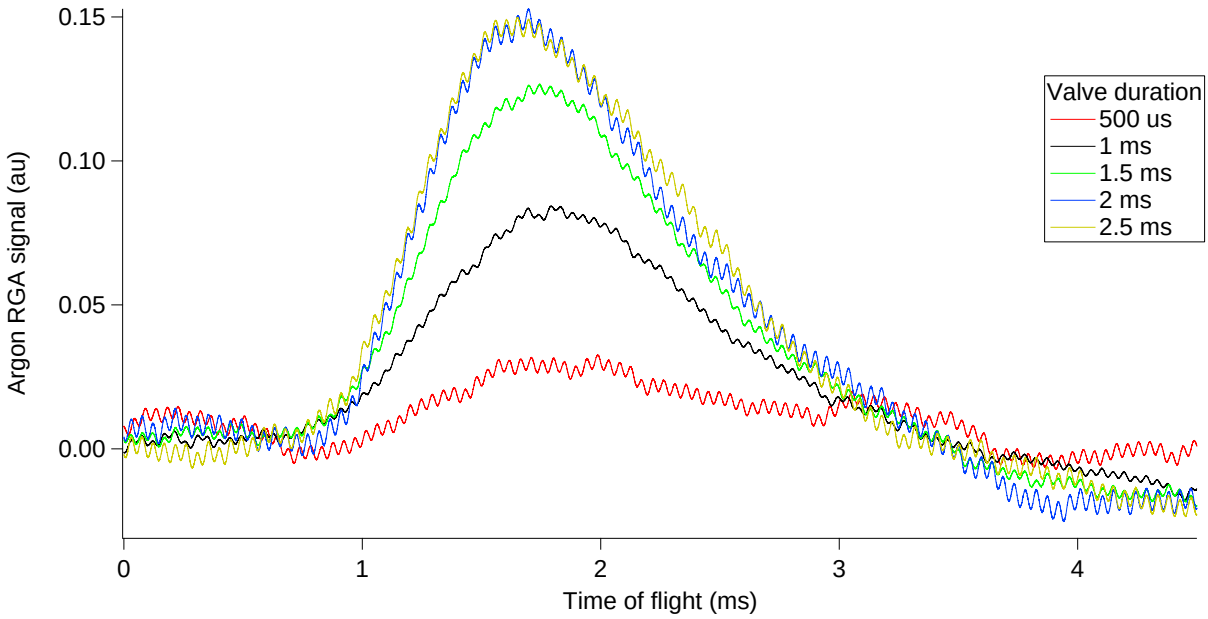

Figure 6-9: Time-of-flight distribution of pure argon gas from counter rotating nozzle at 100 Hz with a backing pressure of 4 bar at different valve opening duration.

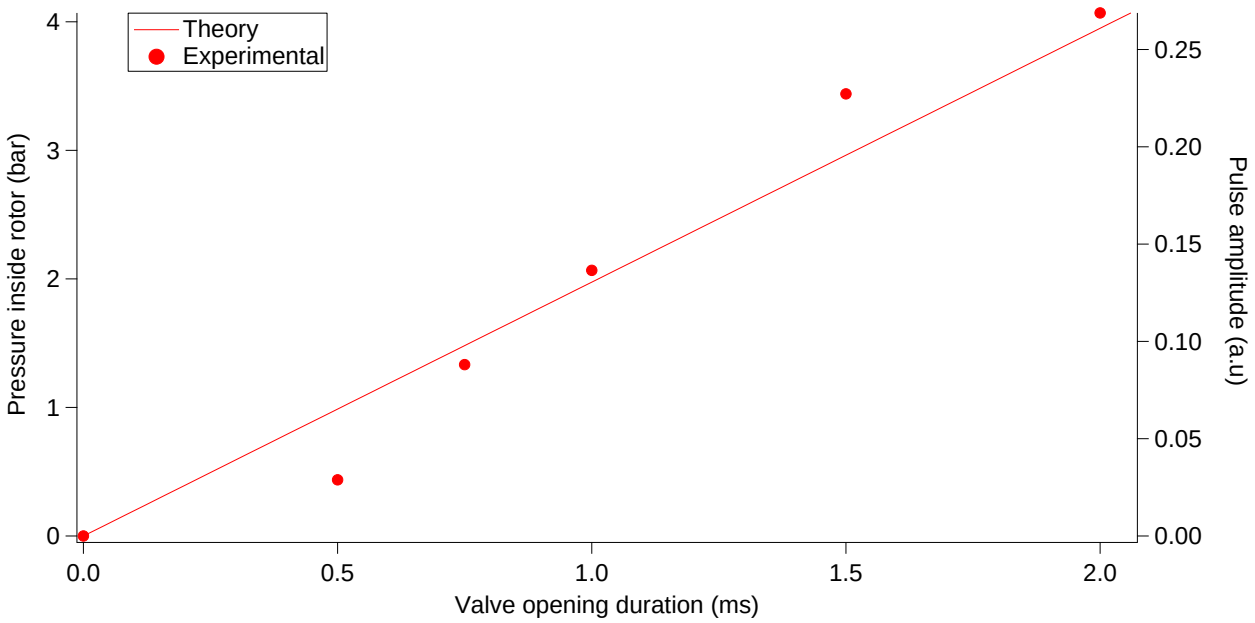

Figure 6-10: : Charging of rotor as a function of time. The red dots denote the peak pulse amplitude (in Figure 6-9) at a rotation speed of 50 Hz and the red line shows the rise of pressure inside a rotor as valve duration is increased from 0 to 2 ms with a source pressure of 4 bar of argon gas as calculated from equation 6-3.

Table 6-2:Beam parameters for acetone beam mixed with krypton gas at different valve opening duration of the pulsed valve. The nozzle rotation speed is 100 Hz with a backing pressure of 4 bar.

Valve opening duration (ms)	**FWHM (m/s)**	**Velocity (m/s)**
0.5	87	359
2	84	361
4	66	331
5	68	352
6	81	386

6.4.4 Effect of rotation speed

The slowed beam velocity through a CRN can be obtained by the expression below:

$$V_{slow} = V_{initial} - 2\pi R\omega \tag{6.5}$$

where V_{slow} is the slowed velocity in the lab frame, $V_{initial}$ is the velocity of molecular beam from a stationary nozzle, ω is the frequency of rotation and R is the radius of rotor arm. The measured time-of-flight distribution of acetone molecules seeded in krypton gas at different rotation speeds is shown in Figure 6-11. As a result of increase in rotation speed, the pressure at the tip of the nozzle, P_{tip} increases than the pressure due to the gas inside the rotor, P_{in}, due to centrifugal effect the which is given by

$$P_{tip} = P_{in} e^{\frac{mV_{rot}^2}{2k_B T_o}} \tag{6.6}$$

Due to centrifugal enhancement of pressure, the FWHM of the beam decreases as the rotation speed increases. Table 6-3 shows the different beam parameters at different rotation speed of the CRN. The decelerated velocity deviates more from the estimation at faster rotation speeds of the nozzle. This might be caused due to the centrifugal effect causing a separation of acetone and krypton as they differ in their mass. krypton atoms being the heavier of the two, are pushed more towards the tip of the nozzle leaving behind acetone molecules and causing a change of mole fraction of krypton in the gas mixture coming out of the nozzle. So, it might be higher than the estimated initial velocity of 430 m/s resulting in higher velocity of acetone molecules than estimated.

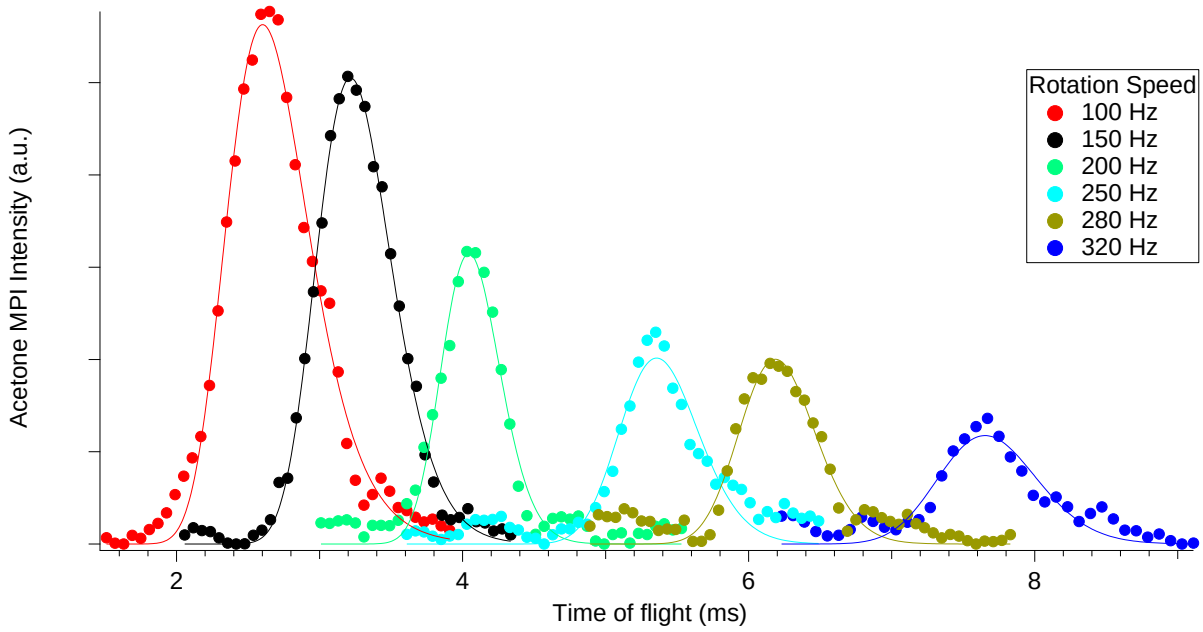

Figure 6-11: Measured time-of-flight distribution of acetone seeded in krypton gas at different speed of rotation at a pressure of 4 bar and a valve opening duration of 4 ms.

Table 6-3:Beam parameters at different rotation speed of nozzle with a valve opening duration of 4 ms and a backing pressure of 4 bar using acetone molecules seeded in krypton gas.

Rotation Speed (Hz)	Decelerated Velocity(m/s)	Estimated Velocity (m/s)	FWHM(m/s)	Longitudinal Temperature(K)
100	330	312	51	27.71
150	261	253	30	3.14
200	209	193	15	0.75
250	157	133	11	0.44
280	136	97	8	0.22
320	110	50	6	0.16

6.4.5 Density measurements

The total number of molecules per pulse N is given by [113]

$$N = \frac{A p_o v \Delta z_{slit}}{k_B T v_{rot}} \sqrt{\frac{2\gamma}{\gamma+1}} \left(\frac{\gamma+1}{2}\right)^{\frac{1}{1-\gamma}} \tag{6.7}$$

Where $A=\pi(d/2)^2$ is the nozzle orifice area, p_o is the pressure, Δz_{slit} is the total distance the nozzle can see the detector ~ 2cms as can be seen in the shutter function (Figure 6-3).

Figure 6-12 shows the number of argon atoms per pulse from three different research groups who have worked with CRN. The maximum pressure used by the groups at Freiburg, Texas and UBC was 220 Torr, 900 Torr and 4560 Torr, respectively. The nozzle diameter in our CRN is 250 μm whereas it is 100 μm in the other two sources. A rotation speed of 300 Hz corresponds to a beam velocity of 200 m/s in our CRN. The number of atoms per pulse in the CRN at this rotation speed from Freiburg, Texas and UBC is 10^{13},10^{14} and 6 x 10^{15}, respectively. Due to installation of the pulsed valve and a leak proof gas line which could withstand a pressure of 8 bar, the comparison between the number of molecules per pulse between the three sources shows that we have an improvement by a factor of two over others.

The density of the beam coming out of CRN is measured using argon atoms with an RGA detector as shown in Figure 6-14. The pressure sensor is used to measure the pressure rise as the gas coming out from the counter rotating nozzle enters the detection chamber. This value, together with the

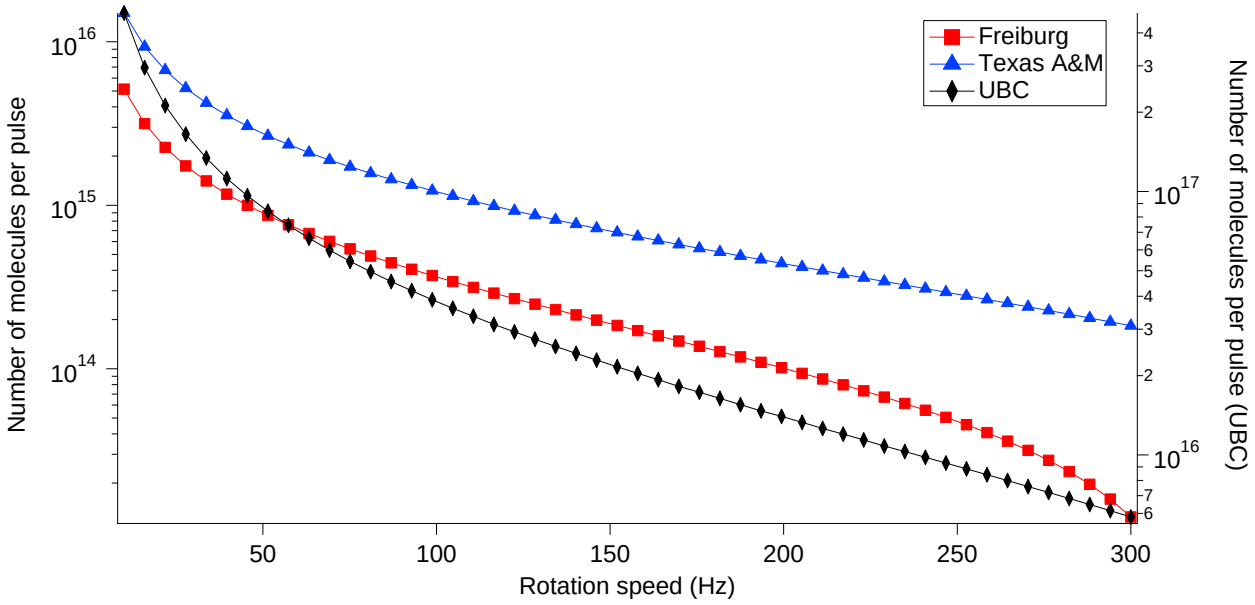

Figure 6-12: Number of Argon atoms per pulse vs rotation speed of nozzle for (a) Freiburg with a continuous nozzle at P=220 Torr, d=0.01 cms (Red trace and y scale on the left), b) Texas A&M with a pulsed source at P=900 Torr,d=.01 cms (Blue trace and y scale on the left) and c) UBC with a pulsed source at P=4560 Torr and d=.025 cms (Black trace and y scale on the right)

corresponding RGA signal amplitude of the background, is used to calculate the number density of the argon gas in the detection chamber. The ratio of pulse to background amplitude can then be used to calculate the density of the molecular beam. This is illustrated in Figure 6-13.

The number density of argon beam can be written as:

$$n_{Ar} = \frac{(P_b - P_p)N_A}{RT} \times \frac{pulse\ RGA\ amplitude}{background\ RGA\ amplitude}$$

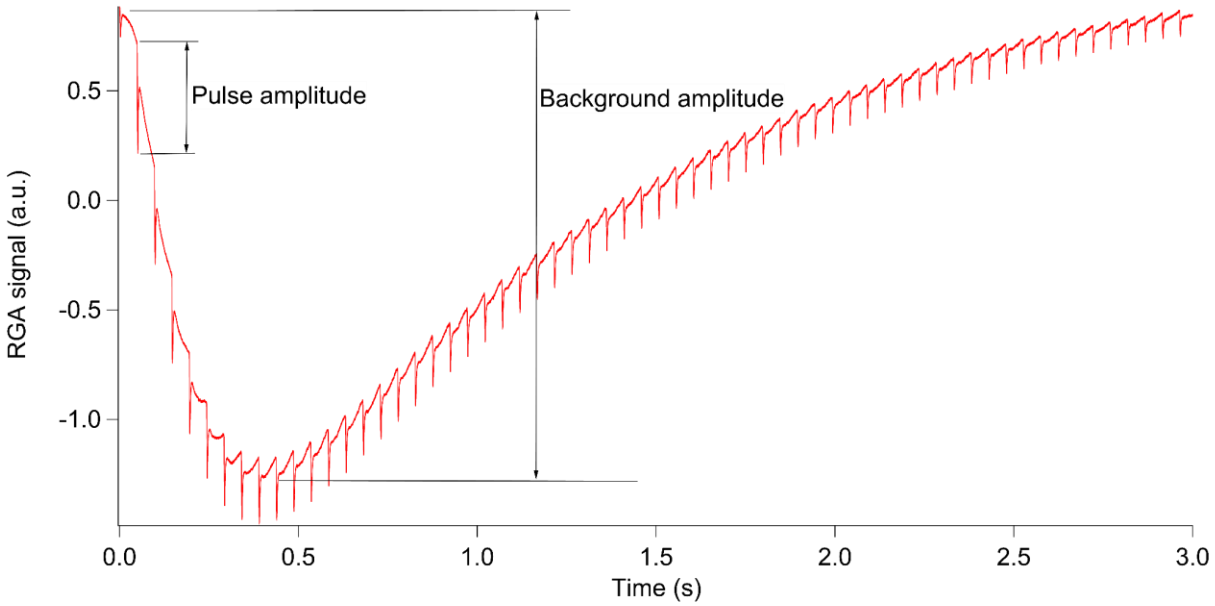

Figure 6-13:RGA signal for a beam of pure argon gas at a nozzle rotation speed of 20 Hz. The experimental period was 3 seconds i.e. the valve is opened every 3 seconds.

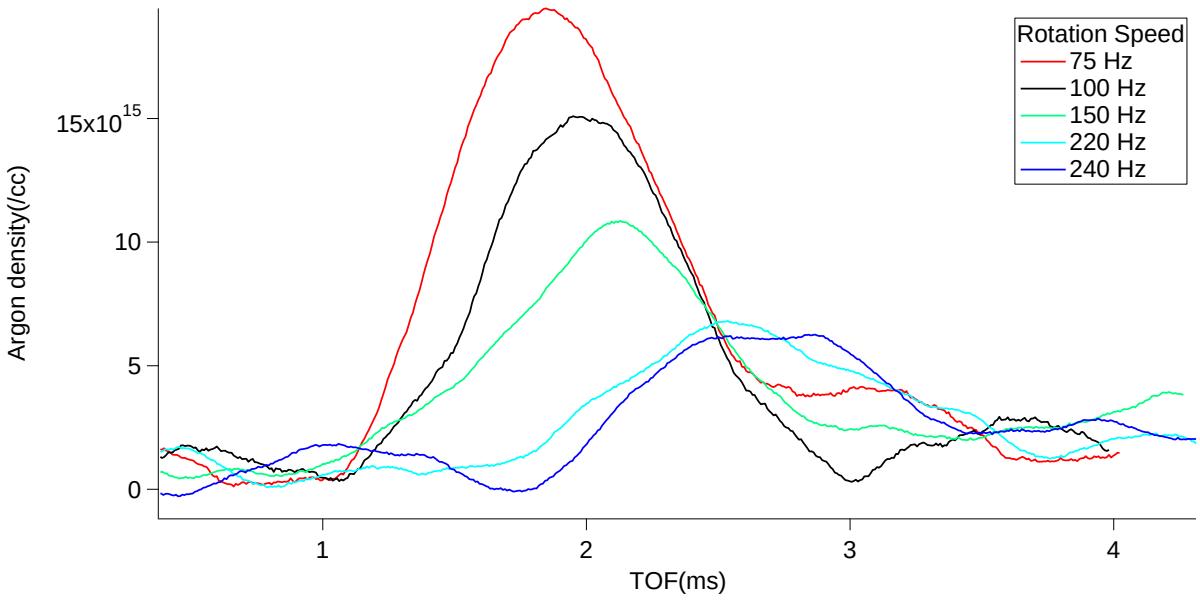

Figure 6-14: Density of pure argon beam at different rotation speed of counter rotating nozzle using RGA. The pressure and the valve opening duration used for this measurement was 4 bar and 2.5 ms, respectively.

6.5 Conclusion and outlook

In this chapter, acetone molecules have been slowed to 110 m/s with a temperature of 160 mK in the moving frame by using a CRN spinning at a frequency of 320 Hz. The density has also been measured at various rotation speed of the CRN using argon atoms. The beam coming out from the CRN can be slowed to any speed by varying its rotation speed. Therefore, in merged beam experiments, CRN can be useful as the collision energy can be easily varied between the two beams. The CRN source can also prove to be useful in aiding the conventional Stark or Zeeman decelerators. The length of Stark or Zeeman decelerators depends on the initial and final speed of the sample molecule such that it is slow enough to be captured inside a trap. CRN can be used to pre-decelerate molecules such that the length of a Stark or Zeeman decelerator can be reduced. Ideally, we should compare the decelerated signal from a decelerator and CRN at the same final speed for a given molecule, in order to see if the beam density can be improved using a combination of CRN with decelerators. One example of this application was the use of CRN in combination with a cylindrical cavity providing focussing force on a beam of CD_3CN molecules by our group [105]. The force due to MW radiation was enough to manipulate the CD_3CN beam which was pre slowed from the CRN before entering the cylindrical cavity.

Unlike, other slowing techniques, CRN has not gained much attention in the field of cold molecules research. The primary reason for this, despite its simplicity, is the decrease in density as the rotation speed increases. The highest reported density from a CRN source is around 10^{12} atoms/cc [115]. With the use of a pulsed valve in our setup, allowing us to produce intense and cold beams with density as high as 10^{15} atoms/cc, CRN might prove to be a useful technique in aid to the current existing methods in support of future developments in cold molecules research.

7 Conclusion and Future work

This thesis presented the first trapping of methyl radicals using an 85 coil Zeeman decelerator. The methyl radicals were decelerated from 320 m/s to 60 m/s before entering the trap region in which they were trapped for more than one second. The temperature of the methyl radicals was 200 mK. The loss of trapped radicals with time was measured at two different background pressure proving that the lifetime of the trapped radicals is dependent on the background pressure. In addition to measurement of trap lifetime at two different background pressure, helium and argon were also introduced in the trap region. These experiments were used to measure the elastic cross section between helium, argon and trapped radical.

The trap lifetime was over 1 second at a background pressure of 3 $x10^{-9}$ Torr. The lifetime reduced to 700 ms when the background pressure was 6.3 $x10^{-9}$ Torr. This suggests that the trap lifetime was limited by background gas collisions. Therefore, in order to increase the trap lifetime, this background pressure needs to be reduced in future. The increased lifetime of the trap will be needed for sympathetic cooling of methyl radicals in order to reduce the temperature below 200 mK. For sympathetic cooling, the ultra cold atoms collide with the relatively hot molecular ensemble to reduce the temperature of the molecular ensemble. During such collisions, the ratio of elastic to inelastic collisions, called as γ, should be larger than 1000 [119]. Tsecherbul et al. have shown the possibility of sympathetic cooling of methyl radicals including 17 other polyatomic radicals using laser cooled alkaline earth atoms.

We are also working towards increasing the density of the trapped radicals as sympathetic cooling will lead to loss of some of the trapped radicals. The trapped radical density can be increased by optimizing the timing sequence for trap loading as shown in appendix. Our simulation shows that

the trapping efficiency can be increased by optimizing the timing sequence for the front coil and rear coils . So far, we have seen an increase up to 5 times, in the number of trapped radicals as per our simulations in comparison to timings calculated by the position and velocity of the synchronous molecule. The increase in trapped radical density can also improve the accuracy of elastic cross section measurement of any background gas with trapped radicals. On the other hand, our lab is working towards building a newer generation of Zeeman decelerator which can increase the density of trapped radicals by two orders of magnitude [118].

A counter rotating nozzle was also used in order to generate cold and dense polyatomic molecular beam. Acetone molecules and argon atoms were used in order to characterize the CRN source at UBC. Acetone molecules seeded in krypton gas was slowed from 430 m/s to 110 m/s with the counter rotating nozzle at a speed of 320 Hz. Using Argon, the beam density coming out of CRN was estimated to be ~10^{15} atoms/cc which is higher than reported value from any other CRN source We have tested our CRN up to a rotation speed of 400 Hz. The time period of one revolution at 400 Hz is 2.5 ms. This duration is enough so that there is no collision between the slowed molecular beam and the rotating nozzle before the beam enters the skimmer. Our deceleration is limited to 110 m/s at 320 Hz for acetone is due to our detection scheme. With the use of a more sensitive detection scheme such as REMPI, we can detect much slower acetone molecules from our CRN. Another way to detect acetone at even slower speeds using the current detection scheme is to move the detection position closer to the nozzle. The distance between the nozzle and the detection point was 85 cms due to the presence of the superconducting cavity.

Some of the improvements which can be made in the current CRN to increase the beam density are as follow. In case of polar molecules, an electrostatic guide can be installed after the skimmer in order to reduce the loss of molecules due to transverse spreading of the molecular beam. Also,

if a pulsed nozzle can be attached to the tip of the rotor, it is possible to reduce the increase in the background pressure in the source chamber which can further increase the density of the slowed beam from a CRN. Lastly, the gas coming out of the CRN can be cooled below room temperature such that the initial supersonic speed of the gas coming out of the CRN is reduced. At the same final slowed velocity from the CRN, a much smaller rotation speed would be needed when the gas is cooled in comparison to the nozzle at room temperature. As the density from the CRN reduces as the rotor speed increases, cooling CRN can also lead to increased density.

Finally, a Fabry Perot cavity was constructed in order to trap ammonia molecules using MW radiation. The Fabry Perot cavity was coated with a superconducting cavity in order to enhance the quality factor. The quality factor of the superconducting cavity was measured to be 5×10^5. At this Q factor and a power input of 10 W, an electric field of 1 MV/m is generated inside the cavity. At this electric field, this trap can capture NH_3 molecules with a speed of less than 10 m/s.

For trapping of ammonia inside the superconducting cavity using MW radiation, the superconducting cavity is installed at the end of Stark decelerator. The Stark decelerator will decelerate ammonia molecules from 400 m/s to 10 m/s which is the trap depth of our MW trap. Another cavity will be constructed as the Q factor for axial modes in the current cavity was very low. The new cavity will be designed in order to minimize the energy loss through the transmission holes in the center. With the new cavity, ammonia molecules can be further decelerated using the axial modes. Deceleration using the transverse modes of the Fabry Perot cavity is technically challenging as the electric field distribution is more complex in comparison to an axial mode. The axial modes quality factor should be higher than the transverse modes and hence the trap depth could be increased using the new cavity. Trapping of ammonia molecules using MW radiation

can be further used for their evaporative cooling. Successful demonstration of evaporative cooling using ammonia in a MW trap can lead to application of the MW trap to any other polar molecules.

Bibliography

1. V. Andreev, D.G. Ang, D. DeMille, et al. Improved limit on the electric dipole moment of the electron. *Nature* 562, 355–360 (2018).
2. Y. Nakai, & M. Reece, Electric dipole moments in natural super symmetry. *J. High Energy Phys*. 8, 31 (2017).
3. S.M. Barr, A review of CP violation in atoms. *Int. J. Mod. Phys. A* 08, 209–236 (1993).
4. M. Pospelov, & A. Ritz, Electric dipole moments as probes of new physics. *Ann. Phys.* 318, 119–169 (2005).
5. Christopher J Pethick and Henrik Smith. Bose-Einstein condensation in dilute gases. *Cambridge university press, 2002.*
6. R. V. Krems, Cold controlled chemistry. *Phys. Chem. Chem. Phys*. 10, 4079 (2008).
7. Zugang Mao & Susan B. Sinnott, Separation of Organic Molecular Mixtures in Carbon Nanotubes and Bundles: Molecular Dynamics Simulations. *J. Phys. Chem. B* 105, (2001) 6916 – 6924.
8. Robert C. Dunbar. Deriving the Maxwell distribution. *Chem. Ed*. 1982, 59, 22-23.
9. Peter F. Bernath. Spectra of atoms and molecules. *Oxford University Press*, (1995).
10. M. H. Anderson, J. R. Ensher, M. R. Matthews, C. E. Wieman, E. A. Cornell, Observation of bose-einstein condensation in a dilute atomic vapor. *Science* 269, 198–201 (1995).
11. K. B. Davis et al., Bose-Einstein condensation in a gas of Sodium atoms. *Phys. Rev. Lett.* 75, 3969 (1995).
12. C. C. Bradley, C. A. Sackett, J. J. Tollet, R. G. Hulet, Evidence of Bose-Einstein Condensation in an Atomic Gas with Attractive Interactions. *Phys. Rev. Lett*. 75, 1687 (1995).

13. Dale G. Fried, Thomas C. Killian, Lorenz Willmann, David Landhuis, Stephen C. Moss, Daniel Kleppner, and Thomas J. Greytak, A Bose-Einstein condensation of atomic Hydrogen. *Phys. Rev. Lett*. 81, 3811 (1998).

14. A. Robert, O. Sirjean, A. Browaeys, J. Poupard, S. Nowak, D. Boiron, C. I. Westbrook, A. Aspec, A Bose-Einstein condensation of metastable atoms. *Science* 292, 461 (2001).

15. S. L. Cornish, N. R. Claussen, J. L. Roberts, E. A. Cornell, and C. E. Wieman, Stable ^{85}Rb Bose-Einstein Condensates with Widely Tunable Interactions.*Phys. Rev. Lett*. 85, 1795 (2000).

16. 10. K. B. Davis, M. -O. Mewes, M. R. Andrews, N. J. van Druten, D. S. Durfee, D. M. Kurn, and W. Ketterle. Bose-Einstein Condensation in a Gas of Sodium Atoms. *Phys. Rev. Lett.* 75, 3969 (1995).

17. S.L. Gilbert, & C.E. Wieman, Atomic-beam measurement of parity nonconservation in cesium. *Phys. Rev. A* 34, 792–803 (1986).

18. M.C. Noecker, P.B. Masterson, & C.E. Wieman, Precision measurement of parity nonconservation in atomic cesium: A low-energy test of the electroweak theory. *Phys. Rev. Lett*. 61, 310–313 (1988).

19. M. Takamoto, F.L. Hong, R. Higashi, & H. Katori, An optical lattice clock. *Nature* 435, 321–324 (2005).

20. C. W. Hoyt, Z. W. Barber, C. W. Oates, T. M. Fortier, S. A. Diddams, and L. Hollberg, Observation and absolute frequency measurements of the $^1S_0$-$^3P_0$ optical clock transition in neutral ytterbium. *Phys. Rev. Lett*. 95, 083003 (2005).

21. A. V. Taichenachev, V. I. Yudin, C. W. Oates, C. W. Hoyt, Z. W. Barber, and L. Hollberg, Magnetic field-induced spectroscopy of forbidden optical transitions with application to lattice-based optical atomic clocks. *Phys. Rev. Lett*. 96, 083001 (2006).

22. A.D. Ludlow et al., Sr lattice clock at 1 x 10^{-16} fractional uncertainty by remote optical evaluation with a Ca clock. *Science* 319, 1805–1808 (2008).

23. T. Rosenband et al., Frequency ratio of Al+ and Hg+ single-ion optical clocks; metrology at the 17th decimal place. *Science* 319, 1808–1812 (2008).

24. J. Ulmanis, M. Deiglmayr, R. Repp, M. Wester, Weidemller, Ultra cold Molecules Formed by Photoassociation. *Chem. Rev*., 112 (9) (2006).

25. M.R. Andrews et al., Observation of Interference Between Two Bose Condensates. *Science* 275, 637-641 (1997).

26. Lincoln D Carr, David DeMille, Roman V Krems and Jun Ye. Cold and ultracold molecules: science, technology and applications., Volume 11, May 2009.

27. H.L. Bethlem and G. Meijer, Production and application of translationally cold molecules. *Int. Rev. Phys. Chem*. 22, 73 (2003).

28. S.Y.T. van de Meerakker, H.L. Bethlem, and G. Meijer, Taming molecular beams. *Nature Physics* 4, 595 (2008).

29. S. Y.T. van de Meerakker and G. Meijer, *Faraday Disc.* 142, 113 (2009).

30. S.D. Hogan, D. Sprecher, M. Andrist, N. Vanhaecke, and F. Merkt, Zeeman deceleration of H and D. *Phys. Rev. A* 76, 023412 (2007).

31. S.D. Hogan, Ch. Seiler and F. Merkt, Rydberg-State-Enabled Deceleration and Trapping of Cold Molecules. *Phys. Rev. Lett*., 103, 123001 (2009).

32. E. Narevicius, A. Libson, C.G. Parthey, I. Chavez, J. Narevicius, U. Even, and M.G. Raizen, Stopping Supersonic Beams with a Series of Pulsed Electromagnetic Coils: An Atomic Coilgun. *Phys. Rev. Lett*. 100, 093003 (2008).

33. E. Narevicius, A. Libson, C.G. Parthey, I. Chavez, J. Narevicius, U. Even, and M.G. Raizen, Stopping supersonic oxygen with a series of pulsed electromagnetic coils: A molecular coilgun. *Phys. Rev. A* 77, 051401 (2008).

34. M.G. Raizen, Comprehensive Control of Atomic Motion, *Science* 324. 1403 (2009).

35. T. Momose, Y. Liu, S. Zhou, P. Djuricanin, & D. Carty, Manipulation of translational motion of methyl radicals by pulsed magnetic fields. *Phys. Chem. Chem. Phys*. 15, 1772–1777 (2013).

36. J.D. Weinstein, R. deCarvalho, T. Guillet, B. Friedrich, and J.M. Doyle, Magnetic trapping of calcium monohydride molecules at millikelvin temperatures. *Nature* 395, 148 (1998).

37. S.E. Maxwell, N. Brahms, R. DeCarvalho, D.R. Glenn, J.S. Helton, S.V. Nguyen, D. Patterson, J. Petricka, D. DeMille and J.M. Doyle, *Phys. Rev. Lett*. 95, 1 (2005).

38. D. Patterson and J.M. Doyle, Bright, guided molecular beam with hydrodynamic enhancement. *J. Chem. Phys*. 126, 154307 (2007).

39. M. Gupta and D. Herschbach, A Mechanical Means to Produce Intense Beams of Slow Molecules. *J. Phys. Chem. A* 103, 10670 (1999).

40. M. Strebel, F. Stienkemeier, and M. Mudrich, Improved setup for producing slow beams of cold molecules using a rotating nozzle. *Phys. Rev. A* 81, 033409 (2010).

41. Schnell, M. and Meijer, G. (2009), Cold Molecules: Preparation, Applications, and Challenges. *Angewandte Chemie International Edition*, 48: 6010-6031.

42. S. R. Logan, The origin and status of the Arrhenius equation, *J. Chem. Educ*. 1982, 59, 4, 279 (1982).

43. Ahren W. Jasper, Stephen J. Klippenstein, Lawrence B. Harding, and Branko Ruscic, Kinetics of the Reaction of Methyl Radical with Hydroxyl Radical and Methanol Decomposition, *J. Phys. Chem.* A 2007, 111, 3932-3950.

44. A. B. Henson, S. Gersten, Y. Shagam, J. Narevicius, E. Narevicius, Observation of Resonances in Penning Ionization Reactions at Sub-Kelvin Temperatures in Merged Beams, *Science* 12 Oct 2012: Vol. 338, Issue 6104, pp. 234-238.

45. Jacqueline van Veldhoven, Rienk T. Jongma, Boris Sartakov, Waldo A. Bongers, and Gerard Meijer, Hyperfine structure of ND_3, *Phys. Rev. A* 66, 032501.

46. G. Scoles, Atomic and Molecular Beam Methods, vol. 1. *Oxford University Press*.

47. A. Amirav, U. Even, J. Jortner, Cooling of large and heavy molecules in seeded supersonic beams, *Chem. Phys*., 51 (1980), pp. 31-42.

48. H. Pauly, Atom, Molecule and Cluster Beams I, *Springer*.

49. C. Yamada, E. Hirota and K. Kawaguchi, Diode laser study of the ν_2 band of the methyl radical. *J. Chem. Phys*. 75, 5256 (1981).

50. W.C. Wiley, and I. H. McLaren, 1955, *Rev. Sci. Instrum*. 26, 115.

51. Jeffrey W. Hudgens, T. G. DiGiuseppe, and M. C. Lin, Two photon resonance enhanced multiphoton ionization spectroscopy and state assignments of the methyl radical, *J. Chem. Phys.* 79, 571 (1983).

52. Moana Nolde, Karl-Michael Weitzel and Colin M. Western, The resonance enhanced multiphoton ionisation spectroscopy of ammonia isotopomers NH3, NH2D, NHD2 and ND3, *Phys. Chem. Chem. Phys*., 2005,7, 1527-1532.

53. Christian Brackmann, Odd Hole,Bo Zhou,Zhongshan S. Li,Marcus Aldén, Characterization of ammonia two-photon laser-induced fluorescence for gas-phase diagnostics, *Appl. Phys. B* (2014) 115: 25.

54. Tomasz Gierczak, James B. Burkholder, Stefan Bauerle, A.R.Ravishankara, *Chemical Physics* 231 1998 229–244.

55. J.C. Whitehead, *Rep. Prog. Phys*. 1996, 59, 993

56. T.G. DiGiuseppe,; J.W. Hudgens,.; Lin, M. C. *J. Phys. Chem*. 1982, 86, 36.

57. Robinson, G. N.; Nathanson, G. M.; Continetti, R. E.; Lee, Y. T. J. Chem. Phys. 1988, 89,

58. Zahedi, M.; Harrison, J. A.; Nibler, J. W. J. Chem. Phys. 1994, 100, 4043.

59. Holt, P. L.; McCurdy, K. E.; Weisman, R. B.; Adams, J. S.; Engel, P. S. J. Chem. Phys. 1984,81, 3349.

60. Davis, S.; Anderson, D. T.; Duxbury, G.; Nesbitt, D. J. J. Chem. Phys. 1997, 107, 5661.

61. Ishiguro, M.; Imajo, T.; Harada, K.; Matsubara, M.; Tanaka, K.; Tanaka, T. Chem. Phys.Lett. 1996, 263,629

62. Anderson, D. T.; Davis, S.; Zwier, T. S.; Nesbitt, D. J. Chem. Phys. Lett. 1996, 258, 207

63. Kogelschatz, U. Plasma Chem. Plasma P. 2003, 23

64. Lewandowski, H.; Hudson, E. R.; Bochinski, J.; Ye, J. Chem. Phys. Lett. 2004, 395, 53.

65. Raunhardt, M.; Sch• afer, M.; Vanhaecke, N.; Merkt, F. J. Chem. Phys. 2008, 128, 164310.

66. Luria, K.; Lavie, N.; Even, U. Rev. Sci. Instrum. 2009, 80, 104102.

67. Ploenes, L.; Haas, D.; Zhang, D.; van de Meerakker, S. Y. T.; Willitsch, S. Rev. Sci. Instrum.2016, 87, 053305.

68. van Beek, M. C..; ter Meulen, J. J. Chem. Phys. Lett. 2001, 337, 237.

69. Roth, J. R. Industrial Plasma Engineering; Boca Raton:CRC Press, 1995; Vol. I

70. Phelps, A. V.; Pack, J. L.; Frost, L. S. Phys. Rev. 1960, 117, 470

71. Halfmann, T.; Koensgen, J.; Bergmann, K. Meas. Sci. Technol. 2000, 11, 1510

72. Even, U. EPJ Tech. Instrum. 2015, 2, 17

73. S. Y. T. van de Meerakker, H. L. Bethlem, N. Vanhaecke, and G. Meijer, Chem. Rev. 112, 4828 (2012).

74. N. Vanhaecke, U. Meier, M. Andrist, B. H. Meier, and F. Merkt, Phys. Rev. A 75, 031402 (2007).

75. S. D. Hogan, A.W. Wiederkehr, H. Schmutz, and F. Merkt, Phys. Rev. Lett. 101, 143001 (2008).

76. E. Narevicius, A. Libson, C. G. Parthey, I. Chavez, J. Narevicius, U. Even, and M. G. Raizen, Phys. Rev. Lett. 100, 093003 (2008).

77. E. Narevicius, A. Libson, C. G. Parthey, I. Chavez, J. Narevicius, U. Even, and M. G. Raizen, Phys. Rev. A 77, 051401 (2008).

78. A.W. Wiederkehr, H. Schmutz, M. Motsch, and F. Merkt, Mol. Phys. 110, 1807 (2012).

79. Y. Liu, S. Zhou, W. Zhong, P. Djuricanin, and T. Momose, Phys. Rev. A 91, 021403(R) (2015).

80. R. deCarvalho, J. M. Doyle, B. Friedrich, T. Guillet, J. Kim, D. Patterson, and J. D. Weinstein, Eur. Phys. J. D 7, 289 (1999).

81. M. Motsch, P. Jansen, J. A. Agner, H. Schmutz, and F. Merkt, Phys. Rev. A 89, 043420 (2014).

82. P. Jansen, L. Semeria, L. E. Hofer, S. Scheidegger, J. A. Agner, H. Schmutz, and F. Merkt, Phys. Rev. Lett. 115,133202 (2015).

83. T. Momose, Y. Liu, S. Zhou, P. Djuricanin, and D. Carty, Phys. Chem. Chem. Phys. 15, 1772 (2013).

84. J. D. Weinstein, R. deCarvalho, T. Guillet, B. Friedrich, and J. M. Doyle, Nature (London) 395, 148 (1998).

85. H.-I. Lu, I. Kozyryev, B. Hemmerling, J. Piskorski, and J. M. Doyle, Phys. Rev. Lett. 112, 113006 (2014).

86. E. Tsikata, W. C. Campbell, M. T. Hummon, H.-I. Lu, and J. M. Doyle, New J. Phys. 12, 065028 (2010).

87. J. Riedel, S. Hoekstra, W. Jäger, J. J. Gilijamse, S. Y. T. van de Meerakker, and G. Meijer, Eur. Phys. J. D 65, 161 (2011).

88. B. C. Sawyer, B. L. Lev, E. R. Hudson, B. K. Stuhl, M. Lara, J. L. Bohn, and J. Ye, Phys. Rev. Lett. 98, 253002 (2007).

89. B. Friedrich, J. D. Weinstein, R. deCarvalho, and J. M. Doyle, J. Chem. Phys. 110, 2376 (1999).

90. B. C. Sawyer, B. K. Stuhl, D. Wang, M. Yeo, and J. Ye, Phys. Rev. Lett. 101, 203203 (2008).

91. B. K. Stuhl, M. T. Hummon, M. Yeo, G. Quemener, J. L. Bohn, and J. Ye, Nature (London) 492, 396 (2012).

92. C. Yamada, E. Hirota, and K. Kawaguchi, J. Chem. Phys. 75, 5256 (1981).

93. S. Hoekstra, J. J. Gilijamse, B. Sartakov, N. Vanhaecke, L. Scharfenberg, S. Y. T. van de Meerakker, and G. Meijer, Phys. Rev. Lett. 98, 133001 (2007).

94. Y. Miyamoto, M. Fushitani, D. Ando, and T. Momose, J.Chem. Phys. 128, 114502 (2008).

95. T. V. Tscherbul, H. G. Yu, and A. Dalgarno, Phys. Rev. Lett. 106, 073201 (2011)..

96. J. T. Hougen and T. Oka, Science 310, 1913 (2005).

97. Z.-D. Sun, K. Takagi, and F. Matsushima, Science 310,139805.

98. Segev Y., Pitzer M., Karpov M., Akerman N., Narevicius J. & Narevicius E. (2019) Nature. 572, 7768, p. 189-193

99. B. Zheng, M. Lin, B. Zhang, and W. Chen, Opt. Commun.73, 208 (1989).

100. J. Zhou, J. J. Lin, W. Shiu, S.-C. Pu, and K. Liu, J. Chem.Phys. 119, 2538 (2003).

101. P. Chandra Jha, Y.Wang, and H. Ågren, ChemPhysChem 9,111 (2008).

102. D. DeMillea, D.R. Glenn, and J. Petricka, MW traps for cold polar molecules, Eur. Phys. J. D 31, 375–384 (2004).

103. Katsunari Enomoto and Takamasa Momose, MW Stark decelerator for polar molecules, PHYSICAL REVIEW A 72, 061403_R_ _2005.

104. Simon Merza,b,c, Claudia Briegerc,†, Nicolas Vanhaeckec,d, Gerard Meijerc,e and Melanie Schnell, Manipulating the motion of polar molecules with MW radiation, Molecular Physics, 2013 Vol. 111, Nos. 12–13, 1855–1864.

105. Steffen Spieler , Wei Zhong , Pavle Djuricanin , Omid Nourbakhsh , Ilja Gerhardt , Katsunari Enomoto , Frank Stienkemeier & Takamasa Momose, MW lens effect for the J = 0 rotational state of CH3CN, Molecular Physics, 2013,111:12-13, 1823-1834.

106. R.J.C. Spreeuw, C. Gerz, Lori S. Goldner, W.D. Phillips, S.L. Roiston, C.I. Westbrook, AIP Conference Proceedings 290, 40 (1993)

107. D P Dunseith et al 2015 J. Phys. B: At. Mol. Opt. Phys. 48 045001

108. C.H. Townes and A.L. Schawlow, MW spectroscopy, Dover Publications.

109. W. Demtroder, Laser Spectroscopy, Springer,3rd edition.

110. J. Bardeen, L. N. Cooper , and J. R. Scrieffer, Phys. Rev., vol. 108, no. 5, p. 1175, 1957.

111. Moon Philip Burton Pulse compression and intensity enhancement in rotor-propelled molecular beams435Proc. R. Soc. Lond. A.

112. M. Gupta and D. Herschbach, A Mechanical Means to Produce Intense Beams of Slow MoleculesJ. Phys. Chem. A 103, 10670 (1999).

113. M. Strebel, F. Stienkemeier, and M. Mudrich, Improved setup for producing slow beams of cold molecules using a rotating nozzle,Phys. Rev. A 81, 033409 (2010).

114. L. Sheffield, M.S. Hickey, V. Krasovitskiy, K.D.D. Rathnayaka, I.F. Lyuksyutov, and D.R. Herschbach, Pulsed rotating supersonic source formerged molecular beams,Rev. Sci. Instrum. 83, 064102 (2012).

115. L. S. Sheffield, S. O. Woo , K. D. D. Rathnayaka, I. F. Lyuksyutov, and D. R. Herschbach, Production of high density molecular beams with wide velocity scanningRev. Sci. Instrum. 87, 064102 (2016).

116. Katsunari Enomoto, Pavle Djuricanin, Ilja Gerhardt,Omid Nourbakhsh, Yoshiki Moriwaki, Walter Hardy ,Takamasa Momose, Superconducting MW cavity towards controlling the motion of polar molecules, Appl. Phys. B (2012) 109:149–157.

117. J. Craig Dutton and Robert E. Coverdill, Experiments to Study the Gaseous Discharge and Filling of Vessels, Int. J. Engineering Ed. Vol. 13, No. 2, p. 123-134, 1997.

118. Etay Lavert-Ofir, Sasha Gersten, Alon B Henson, Itamar Shani, Liron David, Julia Narevicius and Edvardas Narevicius, A moving magnetic trap decelerator: a new source of cold atoms and molecules. *New J. Phys*. 13 103030,2011

Appendix A.

A.1 Density estimation of trapped radical from 2+1 REMPI process

A.1.1 Laser beam parameters

The laser pulse from dye laser has a pulse width of 5 ns at 286 nm. In our experiments, we use a laser energy of 5 mJ/pulse. The diameter of laser beam is around 5 mm. Now, we can calculate the laser beam parameters after the focussing lens which has a focal length of 300 mm.

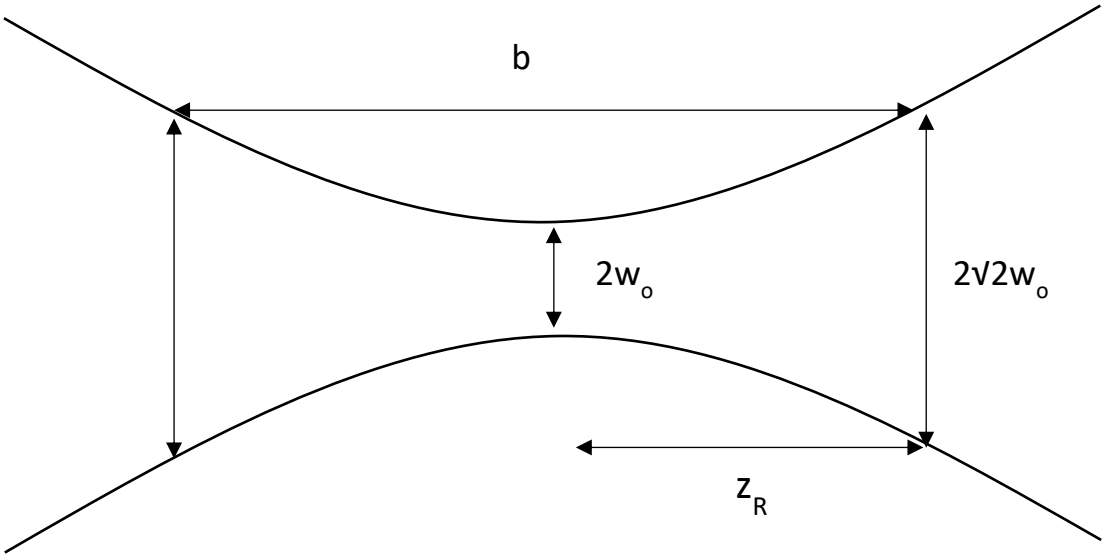

Figure A-1: Laser beam parameters

- Beam waist at focal point, $2w_o = (\frac{4\lambda}{\pi})(\frac{F}{D})$=21.8 μm
- Confocal parameter, b = 2 $Z_R = \frac{2\pi}{\lambda} w_o^2 = \left(\frac{8\lambda}{\pi}\right)\left(\frac{F}{D}\right) = 2.6\, mm$
- Detection volume (laser) ~ $\pi\left(\sqrt{2w_o}^2\right)$ b = 1.5 x $10^{-6}\ cm^3$
- Focal point area, A = $\pi \times \left(\left(\frac{27.3}{2}\right) * 10^{-4}\right)^2 = 3.7 \times 10^{-6}\ cm^2$
- Energy of 1 photon at 286 nm, E = hν = 6.95 x 10^{-19} J

- Total number of photons in one pulse, T = 0.005/E =7.2 x 10^{15} photons
- Photon flux, F = T / (A x 8 x 10^{-9}) = 7 x 10^{27} photons/cm^2/s

A.1.2 2+1 REMPI process parameters

The methyl radicals initially in the ground state n_1 are excited by absorption if two photons to the intermediate excited state n_2. Following another photon absorption, the methyl radical is excited to an ionized state n_3. In order to calculate the density of trapped radicals, we calculate the minimum number of radicals needed at n_1 state in order to get one ionized methyl radical at n_3 state. This will provide us a lower bound for the density estimate.

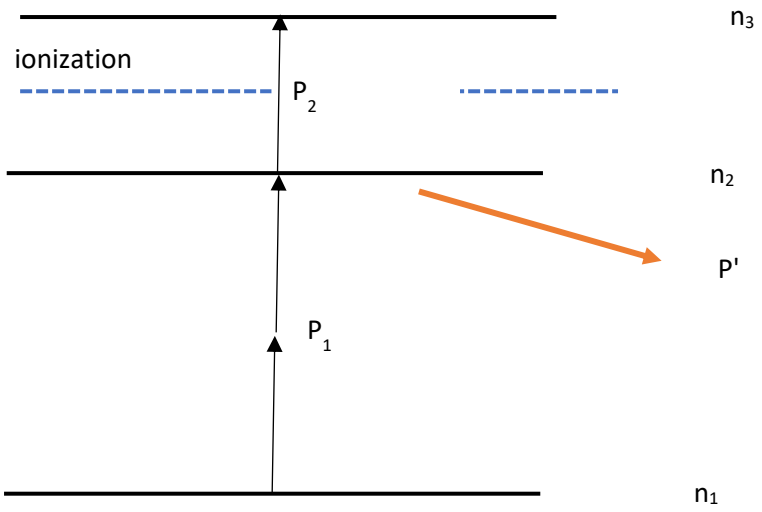

Figure A-2: 2+1 REMPI scheme

Initial conditions:

$n_1(0) = n$

$n_2(0) = n_3(0) = 0$

Time interval = pulse interval = Δt

A simple kinetic model to describe the 2+1 REMPI process is described here [reference]. The time dependence of the population of various states can be written as:

$$\frac{dn_3}{dt} = n_2 P_2 I \tag{10}$$

$$\frac{dn_2}{dt} = n_1 P_1 I^2 - n_2(P_2 I + P') \tag{11}$$

$$\frac{dn_1}{dt} = -n_1 P_1 I^2 \tag{12}$$

Where n_1 is the number of trapped radicals, n_2 is that in the intermediate state after absorption of two photons, n_3 is proportional to ion signal intensity, P_1 denotes two photon transition probability, P_2 denotes ionization transition probability, P' is the predissociation rate of the intermediate state and I is the laser intensity.

The units used for relevant quantities are listed below:

I: Energy flux [W cm^{-2}] = [J s^{-1} cm^{-2}] or I: Photon flux [Photon s^{-1} cm^{-2}]

P_2: 1-photon excitation rate [cm^2 W^{-1} s^{-1}] P_2: 1-photon excitation rate [cm^2 $Photon^{-1}$ s^{-1}]

P_1: 2-photon excitation rate [cm^4 W^{-2} s^{-1}] or [cm^4 $Photon^{-2}$ s^{-1}]

In the steady state,

$$\frac{dn_2}{dt} = 0$$

$$P_1 I^2 n_1 = n_2 (P_2 I + P')$$

$$n_2 = \frac{P_1 I^2 n_1}{P_2 I + P'} \tag{13}$$

$$\frac{dn_3}{dt} = \frac{P_2 I}{P_2 I + P'} P_1 I^2 n_1 = \frac{P_2 I}{P_2 I + P'} P_1 I^2 n \exp(-P_1 I^2 t)$$

$$n_3(\Delta t) = \frac{P_2 I}{P_2 I + P'} N[1 - \exp(-P_1 I^2 t \Delta t)] \quad (14)$$

The intermediate state in our 2+1 REMPI is the 4p Rydberg state. The REMPI spectra shows that the FWHM of the Q branch is 4.5 cm-1. The width of this branch is mainly determined by the predissociation in the 4p Rydberg state.

The lifetime of this transition and the predissociation rate can be calculated as,

$$\tau_{PD} = \frac{1}{2\pi \times 135 \times 10^9} = 1.2\, ps$$

$$P' = \frac{1}{1.2 \times 10^{-12}} = 8.3 \times 10^{11}\, s^{-1}$$

a) Two photon absorption cross section σ:

$$\frac{dI}{dx} = -\beta I^2$$

$$\beta = \frac{n1}{h\vartheta}\, \sigma^2$$

$$\frac{dI}{dx} = -\frac{n1}{h\vartheta}\, \sigma^2 I^2$$

$$\frac{dn_2}{dt} = W_t^2 n$$

$$W_t = \frac{\beta I^2}{2nh\vartheta}$$

Where , β is the two-photon absorption coefficient, σ is the two-photon absorption cross section, x is the interaction length and W_t is the two-photon transition rate [s^{-1}].

$$\frac{dn_2}{dt} = \frac{1}{2}\,\delta N F^2 \tag{15}$$

Where F is the number of photons per unit area per sec (photon flux) given by

$$F = \frac{I}{h\vartheta}$$

$$\frac{F}{c} = \frac{I}{ch\vartheta}$$

where (F/c) is the photon density.

$$\frac{dn_2}{dt} = \frac{1}{2}\sigma^2 I^2 N \tag{16}$$

The change in the number of molecules in intermediate state is two times the change in number of photons.

$$2dn_2 = -d\left(\frac{I}{ch\vartheta}\right)$$

$$\frac{dn_2}{dt} = -\frac{1}{2ch\vartheta}\frac{dI}{dt}$$

$$\frac{dn_2}{dt} = \frac{1}{2}\delta F^2 N = \frac{1}{2}\delta N\left(\frac{I}{h\vartheta}\right)^2$$

$$\frac{dI}{dt} = -ch\vartheta\delta N F^2 = -c\delta N\frac{I^2}{hv}$$

$$dx = cdt$$

Therefore,

$$\frac{dI}{dx} = -n\frac{\delta}{h\vartheta}I^2 = -\beta I^2$$

$$\beta = n\frac{\delta}{h\vartheta}$$

Also, $\beta = n\frac{\sigma^2}{h\vartheta}$

Therefore,

$$\delta = \sigma^2 \tag{18}$$

b) Number of molecules excited per second

$$\frac{dn_2}{dt} = W_T N = \frac{1}{2}\delta N F^2$$

$$W_T = \frac{1}{2}\sigma^2 F^2 = \frac{1}{2}\frac{h\vartheta\beta}{n}\left(\frac{I}{h\vartheta}\right)^2 = \frac{1}{2}\sigma^2\left(\frac{I}{h\vartheta}\right)^2$$

Two photon excitation rate

$$\frac{dn_1}{dt} = -P_1 I^2 n_1 = W_T\ n_1 = \frac{1}{2}\sigma^2\left(\frac{I}{h\vartheta}\right)^2 n_1$$

Therefore,

$$P_1 = \frac{1}{2}\sigma^{(2)}\left(\frac{1}{h\vartheta}\right)^2$$

Case (a) Assume $\sigma^{(2)} \sim 5 \times 10^{-49} cm^4\ s\ molecule^{-1}$,

$$P_1 I^2 = 0.5 \times 5 \times 10^{-49} \times (7 \times 10^{27})^2 = 1.2 \times 10^7\ s^{-1}$$

Since,

$$n_3(\Delta t) = \frac{P_2 I}{P_2 I + P'} N[1 - \exp(-P_1 I^2 \Delta t)]$$

Assume photo ionization cross section of $P_2 = 10^{-17}$ cm^2 from the 4p (3p) state,

$$P_2 I = 10^{-17} \times 7 \times 10^{27} = 7 \times 10^{10}\ s^{-1}$$

The number of ions are given by

$$n_3(\Delta t) = \frac{P_2 I}{P_2 I + P'} N[1 - \exp(-P_1 I^2 \Delta t)]$$

$$n_3(\Delta t) = 2.2 \times 10^{-2} N$$

Taking into account the 10% detection efficiency of MCP, the total number of ions detected i.e. $n_3 = 0.0022$ N. Therefore, 450 radicals are needed in order to obtain 1 radical at MCP. The detection volume, V_D is given by

$$V_D \sim 1.5 \times \pi w_o^2 b = 1.5 \times 10^{-6}\ cm^3$$

A.1.3. Density estimate from simulations

Our sample is made up of a mixture of methane and krypton. The concentration of CH_4 in Krypton is 15%. We can calculate the density of methane gas in this mixture using ideal gas law just before the supersonic expansion. From ideal gas law the methane density n, is given by

$$n = \frac{P}{kT} \tag{4.9}$$

At a pressure P=4 bar and a nozzle temperature T=150 K, n = 2.85 x 10^{19} cm^{-3}.

This is the density of methane gas before the supersonic expansion. Our nozzle opens for 60 μs (Δt) and has a diameter (d) of 250 μm. Taking these number into account and a beam velocity (v) of 340 m/s, the number of CH_4 molecules per pulse can be calculated.

Number of CH_4 molecules per pulse $^{=}$ Nozzle area * v *Δt = 2.85 x 10^{16}

After the supersonic expansion, we assume an efficiency of 1% in the discharge process, 5 % for skimmer, 1% for deceleration and 5 % for trapping. This is calculated by calculating the ratio of molecules at different stages to the initial number of molecules through our simulations. After taking these numbers into account, we estimate the total number of trapped radicals to be 7x10^9.

In order to calculate the density of the trapped radicals, Figure A-3 shows a snapshot of the spatial distribution of the trapped radicals inside the magnetic trap along the longitudinal and transverse directions, respectively, as predicted by particle simulations. Although the maxima of the magnetic fields along the longitudinal direction are separated by 8 mm, 75% of the radicals are confined within ±1 mm at the center of the trap, and 95% are within ±2 mm. On the other hand, about 90% of the radicals are confined within ±300 μm along the transverse direction due to the focusing effect of our Zeeman decelerator coils. Hence, the total effective trap volume V_T is given by

$$V_T = \pi \times 0.3^2 \times 4 = 1.1\, mm^3 = 1.1\ \times 10^{-3}\, cm^3$$

Table A-1 : Efficiency and number of radicals at different stages in the trapping experiment.

Process	Efficiency (%)	Number of radicals
Discharge	1	2.85×10^{14}
Skimmer	5	1.4×10^{13}
Deceleration	1	1.4×10^{11}
Trap	5	7×10^{9}

Hence, the density of trapped radicals is 7×10^{12} /cc, according to our simulations.

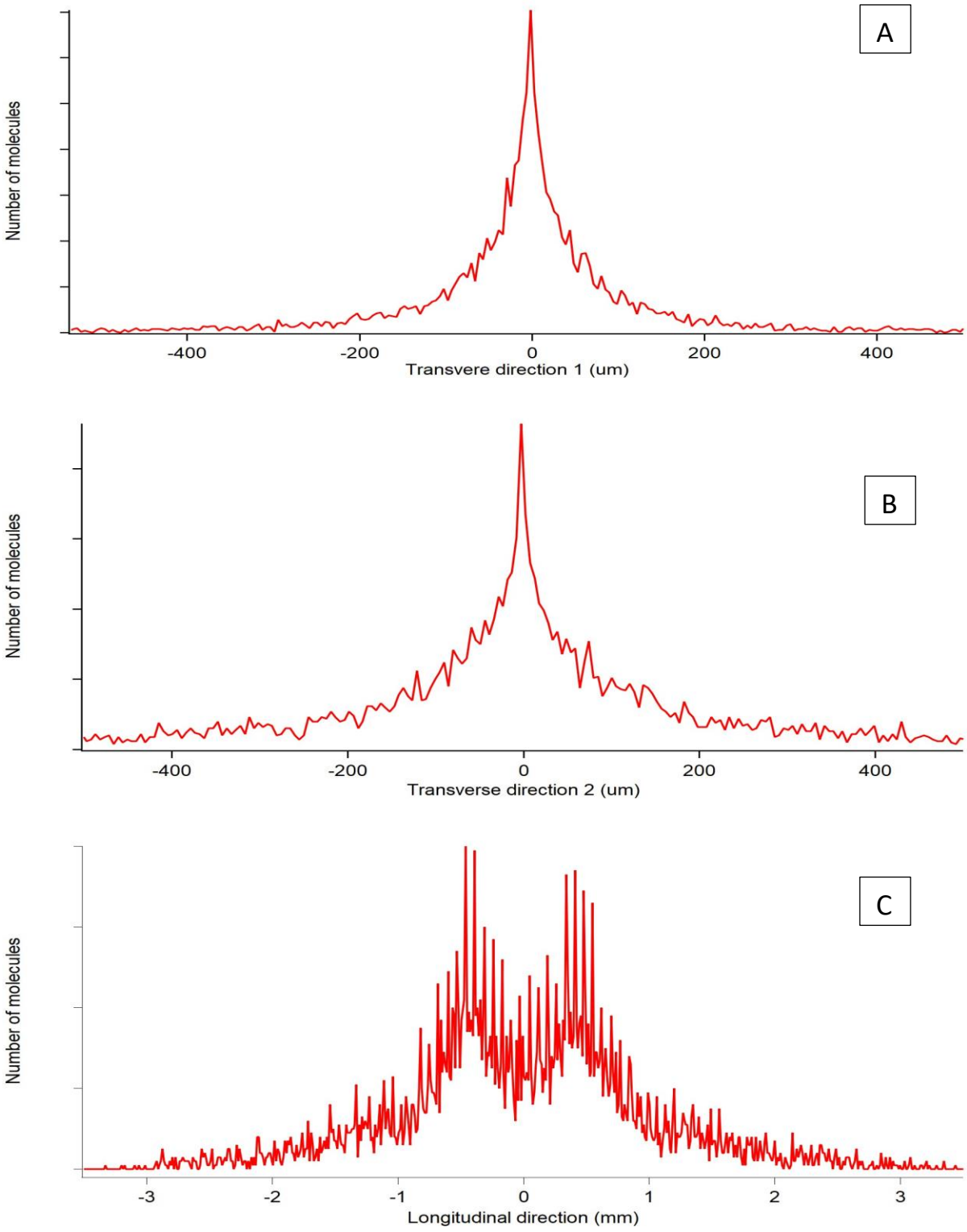

Figure A-3: Spatial distribution of trapped radicals inside the trap region. Figure A shows the distribution along the beam axis whereas Figure B and C shows the distribution in the transverse directions.

A.2 Optimizing number of trapped radical

The number of trapped radicals depends on the timing sequence of the trapping coils. The timing sequence consists of duration of each trapping coil and the delay between them. The phase space plot of the decelerated packet in which the synchronous molecule is travelling at 60 m/s is shown below.

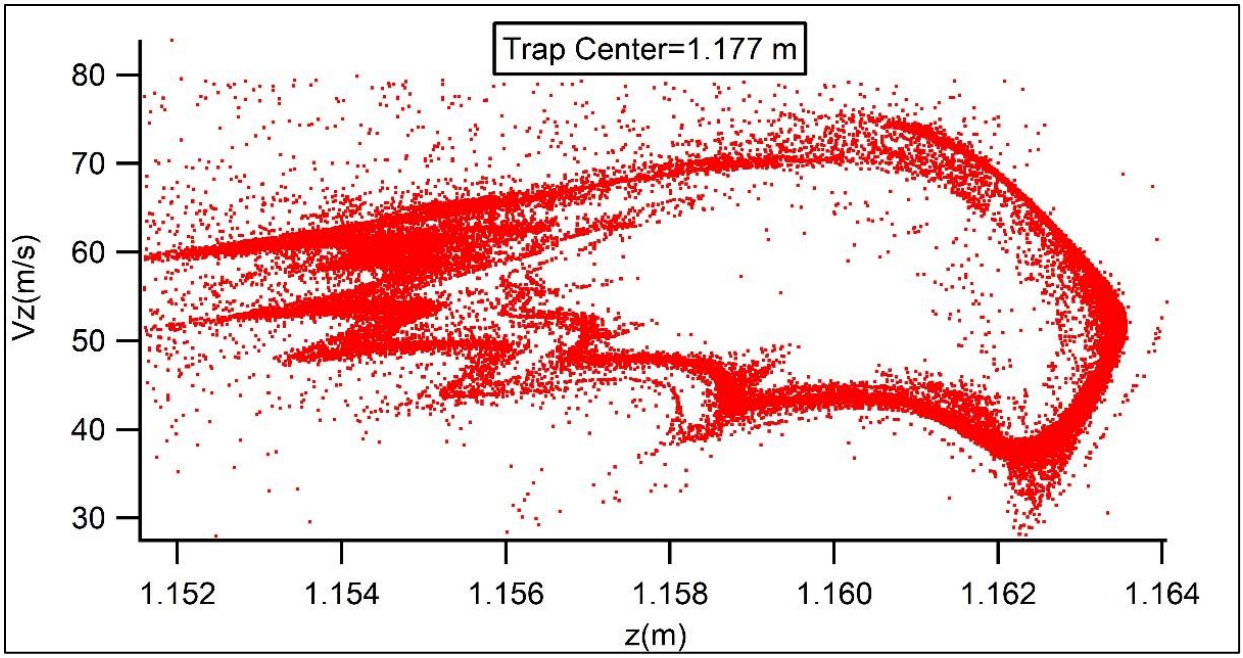

Figure A-4: Phase space plot of a decelerated packet before entering the trap. The velocity of its synchronous molecule is 60 m/s.

The timing sequence which is calculated based on the scheme described in chapter 4 is shown in Table A-2. The duration and the delay of each trapping coil is calculated according to the position and velocity of a single molecule. However, as can be seen in the phase space plot of the decelerated packet, the distribution of molecules is not uniform in space. This suggests that the number of trapped molecules will be different if the timing sequence of trapping coils is different.

On varying the duration and delay between the trapping coils, it was found that the delay between the coils was more sensitive than the duration.

Table A-2: Timing sequence of trapping coils as per position and velocity of the synchronous molecule

	On (μs)	**Off (μs)**	**Duration (μs)**
Front coil (TF)	6820	7020	200
Rear coil (TR)	7130	7300	180

For the decelerated packet shown above, the number of trapped radicals as per the timing sequence in Table A-2 was 940. The total number of radicals in the decelerated packet was 19538. Figure A-3 shows a contour plot of trapped radicals at different front and rear coil timings. The duration of each coil was fixed to 230 μs. The same calculation was done by fixing the coil durations to 170 and 230 μs and the maximum number of trapped radicals was identical in all the cases. The number of trapped radicals increased from 940 to 4810. The only difference among the three cases was the shift of time when the coils are turned on. The number of trapped radicals increased if the front coil was turned on earlier than 6820 us and accordingly, the optimum timing for rear coil was also shifted earlier. This depends on the shape of the decelerated packet i.e. in order to trap the maximum number of radicals, the densest part of the decelerated packet should be targeted. The shape of a decelerated packet varies depending on the initial molecular beam condition, initial velocity of synchronous molecule and the phase angle chosen to obtain the final desired velocity.

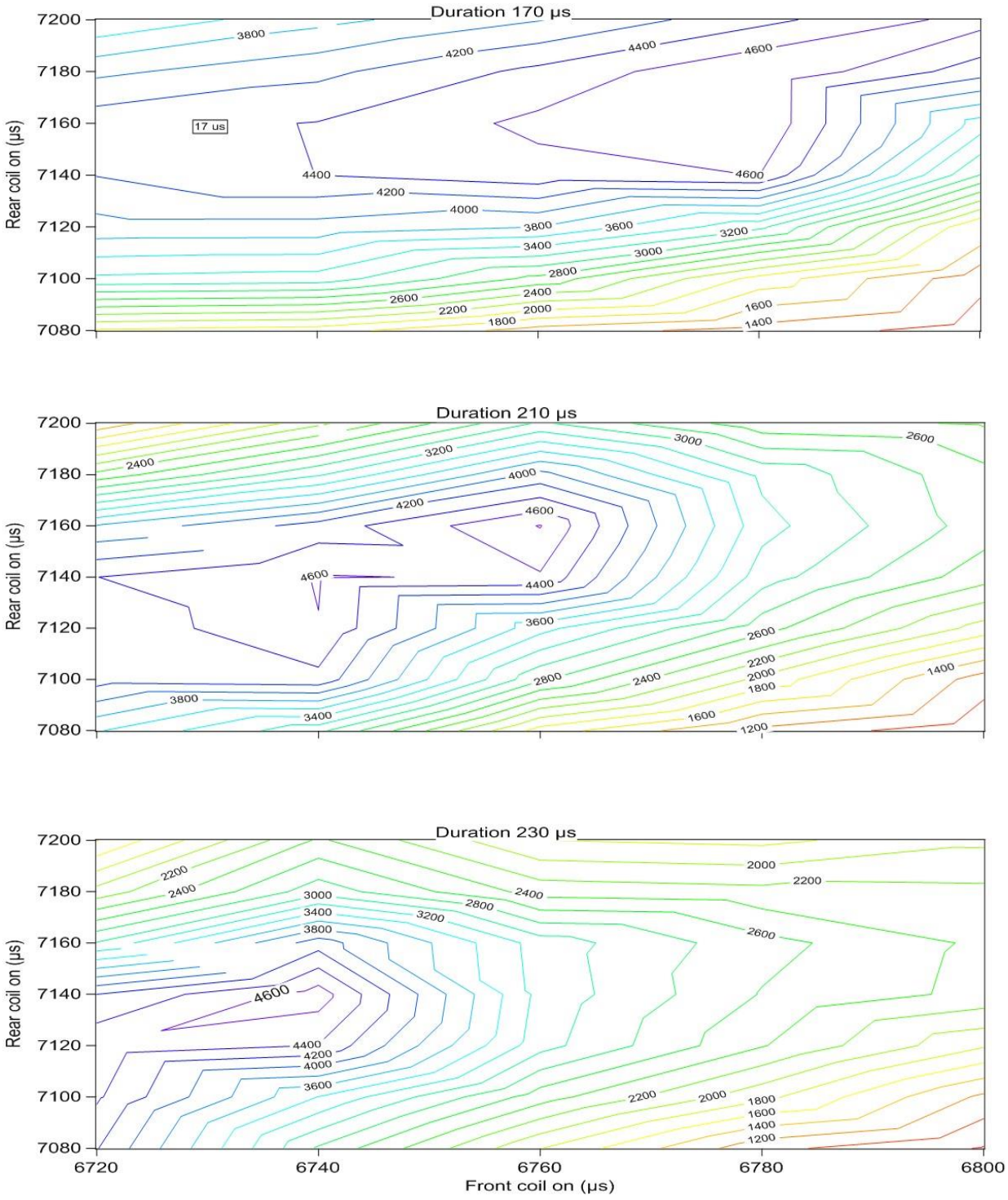

Figure A-5: Contour plot of number of trapped molecules at different front and rear coil timings. The x axis and y axis denote the switch on times for front coil and rear coil, respectively. The total number of molecules in the decelerated packet before entering the trap was 19538. The three contour plots show the number of trapped radicals at different durations of front and rear coils